

**Fixation of sulphur during framboidal pyrite development in a petroleum reservoir  
in Cretaceous volcanics in the Andes: implications for Cu metallogenesis**

**Patrick G. Collins,**

*Department of Earth Sciences, Dalhousie University, Halifax, Nova Scotia, Canada B3H 3J5*

Submitted in partial fulfillment of the requirements for the degree of Bachelor of Science  
(Honours) at Dalhousie University, April 18, 2002



**DALHOUSIE**  
*University*

Department of Earth Sciences  
Halifax, Nova Scotia  
Canada B3H 3J5  
(902) 494-2358  
FAX (902) 494-6889

**DATE:** May 10, 2002

**AUTHOR.** Patrick G. Collins

**TITLE** Fixation of sulphur during framboidal pyrite development in a  
petroleum reservoir in Cretaceous volcanics in the Andes:  
implications for metallogenesis

**DEGREE** **B.Sc. (Honours)**

**YEAR** **2002**

Permission is herewith granted to Dalhousie University to circulate and to have copied for non-commercial purposes, at its discretion, the above title upon the request of individuals or institutions.

---

**Signature of Author**

THE AUTHOR RESERVES OTHER PUBLICATION RIGHTS, AND NEITHER THE THESIS NOR EXTENSIVE EXTRACTS FROM IT MAY BE REPRINTED OR OTHERWISE REPRODUCED WITHOUT THE AUTHOR'S WRITTEN PERMISSION.

THE AUTHOR ATTESTS THAT PERMISSION HAS BEEN OBTAINED FOR THE USE OF ANY COPYRIGHTED MATERIAL APPEARING IN THIS THESIS (OTHER THAN BRIEF EXCERPTS REQUIRING ONLY PROPER ACKNOWLEDGMENT IN SCHOLARLY WRITING) AND THAT ALL SUCH USE IS CLEARLY ACKNOWLEDGED.

## *Table of Contents*

<i>Abstract</i>	<i>vii</i>
<i>Acknowledgements</i>	<i>ix</i>
<i>Chapter 1: Introduction to El Soldado and Definition of Objectives</i>	<i>1</i>
<i>1.1 General Statement</i>	<i>1</i>
<i>1.2 Background</i>	<i>1</i>
<i>1.3 Aims of this thesis: Scientific questions</i>	<i>4</i>
<i>1.4 Practical Implications</i>	<i>4</i>
<i>1.5 Manto-type Deposits of Chile</i>	<i>4</i>
<i>1.6 Association of organic matter and Cu- deposits</i>	<i>8</i>
<i>1.7 Previous work on the El Soldado manto-type copper deposit</i>	<i>9</i>
<i>1.8 Methodology</i>	<i>10</i>
<i>1.9 Thesis Organization</i>	<i>11</i>
<i>Chapter 2: Geology of the El Soldado Deposit</i>	<i>12</i>
<i>2.1 Geology, Stratigraphy, and Structure of El Soldado</i>	<i>12</i>
<i>2.1.2 Structure and other field relationships</i>	<i>15</i>
<i>2.2.1 Lower member of the Lo Prado Formation</i>	<i>18</i>
<i>2.2.2 Upper member of the Lo Prado Formation</i>	<i>18</i>
<i>2.3 Previous Economic Geology Studies.</i>	<i>23</i>
<i>2.3.1 Mineralogy of the Orebody Clusters</i>	<i>23</i>
<i>2.3.2 Paragenesis of the sulphides</i>	<i>26</i>
<i>Chapter 3: Pyrite Study: Understanding the Pyrite Characteristics of El Soldado</i>	<i>28</i>
<i>3.1.1 Introduction</i>	<i>30</i>
<i>3.1.2 Framboidal Pyrite</i>	<i>30</i>
<i>3.1.2.1 Origin of framboids</i>	<i>33</i>
<i>3.1.2.2 Inorganic Processes Related to Framboid Formation</i>	<i>33</i>
<i>3.1.2.3 Organic Processes Related to Framboid Formation</i>	<i>36</i>
<i>3.1.3 Discussion</i>	<i>37</i>
<i>3.1.4 Conclusion</i>	<i>41</i>
<i>3.2 Pyrite Geochemistry</i>	<i>42</i>
<i>3.2.1 Introduction</i>	<i>42</i>
<i>3.3 <math>\delta^{34}\text{S}</math> Isotope Geochemistry</i>	<i>44</i>
<i>3.3.1 Introduction</i>	<i>44</i>
<i>3.3.2 Geochemistry of <math>\delta^{34}\text{S}</math> Sulphur</i>	<i>45</i>

3.3.3 Sulphur Fractionation	48
3.3.4 Distribution of $\delta^{34}\text{S}$ in varying lithologies	49
3.3.5 Previous S Stable Isotope Data	51
<b>Chapter 4: Results for Petrology, Microprobe analysis, and <math>\delta^{34}\text{S}</math> Isotopic Analysis</b>	<b>53</b>
4.1 Introduction	53
4.2. Petrographic Descriptions	53
4.2.1 Ore zone	53
4.2.2 Deep Pyrite Zone	73
4.2.3 Petrographic Summary	80
4.2.3 Petrographic Summary	81
4.3 Geochemistry	82
4.3.1: Microprobe sulphide analysis	82
4.3.2: Geochemistry of $\delta^{34}\text{S}$ Isotopes	83
4.3.3: $\delta^{34}\text{S}$ Isotope Summary	90
<b>Chapter 5: Discussion: To What Degree is El Soldado Pyrite of Low – Temperature Genesis?</b>	<b>91</b>
5.1.1 Introduction: Stage I Sulphides	91
5.1.2 Stage I Petrology	91
5.1.3 Stage I Geochemistry	101
5.1.4 $\delta^{34}\text{S}$ Isotope Geochemistry	105
5.1.5 Implications for metallogenesis	107
5.1.6 Fluid Inclusions	107
5.1.7 Conclusion	108
<b>Chapter 6: Conclusions and Future Research Avenues</b>	<b>110</b>
6.1: Conclusions	110
6.2: Future Research Avenues: Useful Projects on El Soldado	111
Appendix A	113
Figure Captions for Figures A.2 to A.5	114
Appendix B	121
Appendix C	124
Sample Descriptions	125
Appendix D	128
References	138

## Table of Figures

Figure 1.1 Location Map of El Soldado	3
Figure 2.1: Map of General Orebody Clusters, El Soldado	13
Figure 2.2: General Zonation of Individual Orebody Clusters	14
Figure 2.3 Regional Geology in close proximity to El Soldado	16
Figure 2.4 Cross section through Filo and Valdivia Sur orebody clusters	17
Figure 2.5: Discriminant plots of El Soldado rocks	20
Figure 2.6: Columnar jointing and faulting in Lo Prado	21
Figure 2.7: Camp-scale structural characteristics	25
Figure 3.0a,b: Pyrite morphology and crystallography	29
Figure 3.1: SEM of framboidal pyrite	32
Figure 3.2: Possible sulphur pathway	34
Figure 3.3: Possible pathway for the formation of framboids	35
Figure 3.4: Eh-pH diagram for Fe oxides and sulphides	43
Figure 3.5: $\delta^{34}\text{S}$ values for some natural materials	47
Figure 3.6: Possible sulphur pathway	49
Figure 4.1: Bornite replacing framboids	55
Figure 4.2: Bornite replacement – remnant pyrite grains	56
Figure 4.3a: Progressive framboid replacement	58
Figure 4.3b: BSE microprobe image of framboid replacement	59
Figure 4.4: Cut slab sample of PC-02	61
Figure 4.5: Brecciated pyrite with chalcopyrite infilling	62
Figure 4.6: Cartoon of morphology of large pyrite grains	63
Figure 4.7: Cartoon of interstitial zones in massive pyrite	64
Figure 4.8a: Heterogeneity in framboidal zones	64
Figure 4.8b: Microprobe image of framboid zone composition	65
Figure 4.9: Cut slab sample of PC-04 and sample of PC-04.	69
Figure 4.10: Chalcopyrite replacing framboidal pyrite	70
Figure 4.11 a, b & c.	71
Figure 4.12: Late idioblastic pyrite cubes and pyritohedron	75
Figure 4.13: Large colloform structure in pyrite	76
Figure 4.14: Microprobe image of colloform spheroids	77
Figure 4.15: Plate-like pyrite textures	78
Figure 4.16 : Poikiloblastic pyrite aggregates	80
Figure 4.17. Valdivia Sur $\delta^{34}\text{S}$ values	87
Figure 4.18. Arauco $\delta^{34}\text{S}$ values	87
Figure 4.19 Arauco Norte $\delta^{34}\text{S}$ values	88
Figure 4.20: Morro and Catedral $\delta^{34}\text{S}$ values	89
Figure 4.21: Inclusion zoned cubic pyrite for all data	89
Figure 5.1 a, b	93
Figure 5.2a: SEI microprobe image of framboidal pyrite zone	97
Figure 5.2b: Compositional microprobe image of framboids	98
Figure 5.3 a, b	99
Figure 5.4: Compositional zoning and atoll structures in framboids	102
Figure 5.5a, b: Multiple stages of pyrite growth	104
Figure A.1	115
Figure A.2	116
Figure A.3	117
Figure A.4	118
Figure A.5	120

## **Table of Tables**

<i>Table 3.1 Weighting different framboid arguments.....</i>	<i>40</i>
<i>Table 3.2: Mean <math>\delta^{34}\text{S}</math> ‰ for some lithologies.....</i>	<i>49</i>
<i>Table 4.4: Summary of isotopic and textural data.....</i>	<i>85</i>
<i>Table B.1.....</i>	<i>122</i>
<i>Table B.2.....</i>	<i>123</i>
<i>Table D.1 Microprobe data for Pyrite analysis.....</i>	<i>135</i>
<i>Table D.2: Chalcopyrite data.....</i>	<i>138</i>
<i>Table D.3: Bornite microprobe data.....</i>	<i>140</i>
<i>Table D.4: All values with high levels of As.....</i>	<i>141</i>

## Abstract

El Soldado, Chile, is a giant strata-bound copper deposit hosted in Lower Cretaceous basalt and rhyodacite. Previous work suggested that copper was concentrated preferentially where hydrothermal copper-rich solutions replaced pre-existing, low-temperature, diagenetic pyrite, which is generally associated with bitumen (solidified petroleum). Doubt remains on whether some deep zones with massive crystalline pyrite veins, and massive chalcopyrite, bornite and chalcocite ores, could represent a net input of sulphur from hydrothermal, magmatically-derived sources. Magmatic related sulphur has a  $\delta^{34}\text{S}$  value close to zero per mil. Conversely, diagenetic, low-temperature crystallization of pyrite, especially with the aid of sulphur-reducing bacteria in a degrading petroleum reservoir, would have led to extreme fractionation of sulphur and a wide range of  $\delta^{34}\text{S}$  values, which would be locally available to form Cu sulphides during the hydrothermal phase.

There is textural evidence of pre-existing diagenetic pyrite, as well as textures indicative of new hydrothermal growth. Diagenetic pyrite is characterized by framboidal structures of ca.  $16\mu\text{m}$  diameter or smaller; colloform textures found in pyrite also suggest a low-temperature genesis. Although controversial, the general consensus is that framboids may grow with bacterial involvement. A range of stages of development of massive crystalline aggregates is observed in the samples: individual microcrysts, framboids, framboid clusters, recrystallized megacryst overgrowths, and banded concentric zones. Hydrothermal or high-temperature textures are characterized by idioblastic pyrite cubes or pyritohedra suspended in late calcite matrix. Temperatures

from fluid inclusions in calcite indicate maximum (pressure corrected) temperatures of ca. 300 °C, and minimum temperatures of over 100 °C.

$\delta^{34}\text{S}$  values from analysis in this study have a range of 24.5‰, from -7.4‰ to +17.1‰. This variation is characteristic of a compartmentalized system that has been incompletely fractionated, and is compatible with bacterial interaction. Several samples yielded  $\delta^{34}\text{S}$  values overlapping with that characteristic of magmatic sulphur, thus allowing for the possibility of some degree of input of homogenized sulphur, perhaps (but not necessarily) from a magmatic source.

Microprobe analyses indicate the presence of local concentrations of arsenic within the core of framboidal structures and also in fresh overgrowths on idiomorphic pyrite, probably inherited from the diagenetic phase.



## **Acknowledgements**

This thesis would not have been possible without the help of several people. Firstly, thanks go to my advisor, Dr. Marcos Zentilli, for providing me with an incredibly interesting project, and then helping with the science and logistics of the project. Secondly, thanks go to Ricardo Boric, for providing samples from the El Soldado mine site, and for sharing his immense knowledge of the deposit with me. Bob MacKay advised and trained me on both microprobes at Dalhousie, and I am grateful for his patience while I learned the ropes. Gordon Brown painstakingly made and the beautiful polished thin sections that I pored over for hours at a time – thanks for the hard work Gordon! Also, thanks to Joyia Chakungal for helping with editing and grammatical corrections.

Thanks to my peers at Dalhousie for advice and criticism during the evolution of the thesis, and for the company during the long days slogging away.

Of course, thanks to my parents for the patience while my other classes suffered, and for the freedom to always have transportation to school for the long evenings of work and of course for paying my way as I blundered through the years here at Dal.

## **CHAPTER 1: INTRODUCTION TO EL SOLDADO AND DEFINITION OF OBJECTIVES**

### **1.1 General Statement**

El Soldado is located in Central Chile (32°38'S; 71°04W) (Figure 1.1). It is the largest (>200 Mt @ 1.4 % Cu) of the known Cu manto-type deposits in central Chile and is strata-bound within a submarine, bimodal calc-alkaline basalt - rhyodacite unit of the Lower Cretaceous Lo Prado Formation, which also contains marine carbonaceous shale and volcanoclastic sandstones (Boric et al., 2002).

It is generally accepted that hydrothermal sulphide base metal deposits in island arcs are formed by calc-alkaline magmas that provide both metals and sulphur (Sillitoe, 1992). However, it has been proposed (Zentilli and Wilson, 1999) that some very large (manto-type) Cu deposits in the Andes may have originated by hydrothermal enrichment of copper replacing pre-existing diagenetic pyrite generated by bacterial action, or contribution, to degradation of petroleum. This thesis attempts to test the validity of this model for certain ores that contain massive pyrite veins or occur in deep zones of the El Soldado deposit in Central Chile, using textural (ore microscopy) studies and sulphur isotope analysis.

### **1.2 Background**

According to Wilson and Zentilli (1999), El Soldado would have formed in a shallow petroleum reservoir in the host Cretaceous Lo Prado volcanic sequence. Petroleum would have migrated from underlying organic rich sediments. Two stages of metallogenesis would have occurred. The first stage (herein called Stage I) is characterized by pyrite,

predominantly with a spheroidal or framboidal texture, that would have formed at temperatures below 100° C from reduction of sulphate in pore water by sulphate reducing bacteria, most likely of the genus *Desulfovibrio*, or *Desulfotomaculum* e.g. Goldhaber and Kaplan, (1974). The action of bacteria is interpreted from sulphur isotope data. The second stage, when the actual copper mineralization formed, is later, at higher temperatures and is characterized by copper sulphide minerals and hydrothermal pyrite (Stage II) (Wilson, 1998).

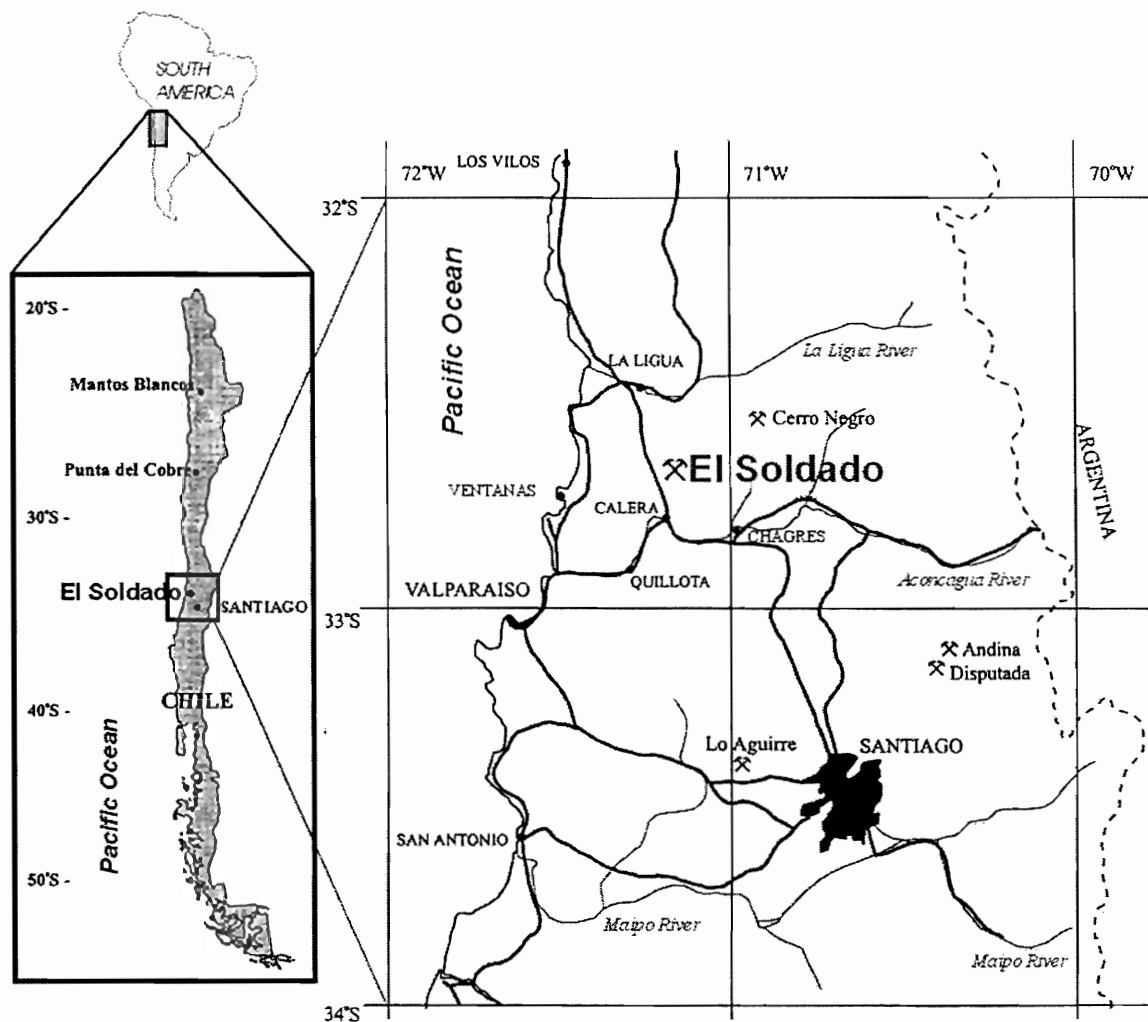


Figure 1.1 Location map of El Soldado deposit in Central Chile.

The Chagres Smelter by the Aconcagua River, and the Disputada (Los Bronces) porphyry Cu deposit and mine in the high Andes, as well as El Soldado, are owned and operated by Compañía Minera Disputada de las Condes. Also shown are manto type Cu deposits Mantos Blancos, Punta del Cobre, Cerro Negro and Lo Aguirre.

The mine operators, CMD/Exxon Minerals Chile were not convinced that all the pyrite could possibly be diagenetic and pre-existing. They believe that there was also a younger generation of high temperature phase of pyrite, in the form of massive pyrite veins.

### **1.3 Aims of this thesis: Scientific questions**

The aim of this thesis is to test whether all pyrite at the El Soldado deposit is of a low temperature, diagenetic origin, or if there is also a high temperature, hydrothermal phase of pyrite. This thesis also investigates the importance of framboidal pyrite in terms of copper metallogenesis.

### **1.4 Practical Implications**

This study has practical implications for the mine because unless more economic grade orebody clusters are discovered soon, it will close in a few years time. The low-temperature diagenetic pyrite appears to require, as prerequisite, organic matter to be present in order to form. If there is only low temperature pyrite, which is replaced to form Cu ore, then the Cu is thus restricted to where low temperature pyrite formed. If on the other hand it is proven that there is also a high temperature phase of pyrite, the Cu ore is not as restricted in where it could have formed, thus expanding the range of possible economic orebody clusters.

### **1.5 Manto-type Deposits of Chile**

According to Evans (1993), manto-type, or strata-bound deposits are “those deposits which are restricted to a fairly limited stratigraphic range within the strata of a

particular region". Wilson (1998) further emphasizes the definition of a manto-type deposit as one that is associated with a specific lithological unit and did not necessarily form syngenetically. For example, epigenetic mineral deposits, those forming after the deposition of host rocks, can be locally discordant with the strata, but at the same time still be restricted to a certain formation or member, thus still be considered stratabound. In Chile, Cu-manto deposits are second in Cu quantity only to porphyry-type deposits (Wilson, 1998). The main host for these manto-type deposits is Mesozoic volcanic-sedimentary rock. These deposits are distributed throughout the Andean orogen, hosted by volcano-sedimentary sequences of Jurassic to Eocene age (Sato, 1984).

There are differing views on the genesis of manto-type deposits, with two models or hypothesis being the most accepted. Holmgren (1987) stated that magmatic fluids are the source of the Cu, while other workers such as Sato (1984) and Sillitoe (1990) suggested that fluids liberated during crustal thinning or low-grade regional metamorphism of the volcano-sedimentary piles were the likely transporting agents of the copper

The general characteristics of Chilean manto-type deposits have been summarized by Sato (1984), Sillitoe (1990) and Wilson (1998) as follows:

1. Mantos are found in various horizons in the Jurassic to Eocene volcano-sedimentary piles of marine and continental origin.
2. Mineralization has occurred in favorable horizons, especially porous rocks such as amygdaloidal andesite, hydrothermal breccia, and volcanic breccia- sandstone containing little matrix.

3. The mineralized horizons are covered in many cases by impermeable rocks such as shale, siltstone, and compact lava flows.
4. The site of mineralization is controlled in many cases by faults and in some other cases by intrusive bodies. There is structural and/or lithological permeability that has localized mineralization, which is combined with contrasts in the redox state of the host lithologies. Deposits are typically found in reduced horizons juxtaposed with red, commonly hematized units.
5. There is no distinct wallrock alteration, but diagenetic and burial metamorphic processes have combined to extensively alter the host lithologies. This assertion has been contested by Boric (2002 in preparation) and Boric et al. (2002).
6. The ore mineralogy is S-deficient being composed of chalcopyrite, bornite, chalcocite, hematite, and/or magnetite with little pyrite. Zonation of orebodies is from central hematite through chalcocite, bornite, and chalcopyrite to distal pyrite. The mineral assemblages have the highest metal/S ratios (hypogene chalcocite, bornite, and hematite) in high- grade (>2% Cu) parts of the deposits.
7. Gangue minerals are minor except for calcite, which is relatively abundant in many deposits. Associated alteration and gangue assemblages are broadly similar to the prehnite-pumpellyite and greenschist metamorphic facies developed in the host rock sequences. Local albitic and K-feldspar alteration occurs in some high-grade Cu zones (Boric et al., 2002)

The above information suggests that the deposits are of hydrothermal origin, but that the solutions responsible lacked a contrasting chemistry or temperature as compared with

the connate fluids that would have been in regional equilibrium with the host or country volcano-sedimentary rocks (Sato, 1984). Conversely, the phase of fluid flux could have been rapid enough to have only negligible effects on host rocks. According to Sato (1984), the abundance of calcite, one of the primary gangue minerals, indicates that a temperature decrease, a key precipitation mechanism in many hydrothermal deposits, did not play an important role in El Soldado. In addition (Sato, 1984) suggested that the absence of notable wallrock alteration (but see Boric et al., 2002) suggests that a change in pH was also not a sulphide precipitation factor. The disappearance of epidote and the increase in calcite and hematite towards mineralized zones suggests that changes in pressure (especially  $P_{CO_2}$ ) and/or oxygen fugacity ( $fO_2$ ) may have taken place at the site of mineralization (Sato, 1984; Westra, 1988). Sato has also proposed that impermeable beds such as the Upper Lo Prado Formation caused mineralizing solutions migrating through faults to become dammed up, resulting the precipitation of Cu in the underlying porous beds below.



## **1.6 Association of organic matter and Cu- deposits**

The associations of organic matter and their derivatives have been recognized as factors in the formation of sedimentary and diagenetic ore deposits as well as spatially related components in higher temperature deposits Zentilli et al. (1997). North (1985) establishes that organic carbon is partitioned in the crust in several different ways, but mainly as finely disseminated particles in sediments, or as marine limestone and carbonate rich shale. Only a small proportion of this organic carbon is present as hydrocarbons such as natural gas and oil, and it is estimated that only 0.01% of this petroleum is contained in known significant reservoirs.

According to Manning and Gize (1993), organic matter commonly occurs associated with low temperature ore deposits that are hosted by (organic-rich) sedimentary rocks that are part of a maturing basin, such as the environment in which El Soldado formed. In particular, Mississippi Valley type Pb-Zn, Carlin Au, as well as several other sedimentary mineral deposit styles are known to have organic matter (e.g. bitumen) associated with metallogenesis. Organic matter has chemical attributes that make it possible to transport elements not normally soluble or otherwise compatible in aqueous fluids (e.g. Manning, 1986).

It is common for petroleum to be enriched in metals, especially vanadium, which can reach 2000 ppm in Venezuelan crude oil (Manning and Gize, 1993). Other metals (e.g. As, Ni, Au, Co) can become enriched as well, often being transported as porphyrin complexes (Manning and Gize, 1993). Also, oil can act as a good trap for metals, containing them until a potential ore fluid interacts with the petroleum and reduction of the fluid and precipitation of metal occurs.

Because of this long known spatial relationship between organic carbon and metal deposits, it is logical to expect interaction between one form or another of petroleum within an ore-forming environment. This relationship means that a model for petroleum migration and oil brines or ore fluids associated with them can be applied. This includes the sequential consideration of source, mobilization, migration, entrapment and preservation. Recent advances in the analysis of organic matter means that it is possible to combine data where relationships between bitumen and metals occurs in order to draw more probable and encompassing models (Zentilli et al., 1997).

### **1.7 Previous work on the El Soldado manto-type copper deposit**

The following section summarizes the studies undertaken on El Soldado. Table 1 summarizes past papers published on El Soldado in terms of the interpretations of genetic model, constraints the study posed, listing any problems with the model, according to Wilson (1998).

As summarized by Wilson (1998), several models have many points that make them more viable than others. These models include magmatic fluids, expelled during cooling, having high concentrations of Cu ions or Cu-complexes (Holmgren, 1987), or fluids liberated during crustal thinning and low-grade diastathermal metamorphism (e.g. metamorphism related to above average heat flow related to extensional tectonics). This diastathermal metamorphism is typical of the volcanic and volcanoclastic piles in a rifting environment (Robinson and Bevins, (1989); Sato (1984); Westra, (1988); Sillitoe, (1990)). It is proposed by other authors that a combination of magmatic hydrothermal fluids, together with metamorphic hydrothermal fluids (e.g. Fontboté, 1990) could be the

most logical source of fluids. Other authors favor an all-encompassing, regional metamorphism model due to the high level of mineralogical correlation between different deposits (Sillitoe, 1992).

## **1.8 Methodology**

This study uses two primary analytical tools to investigate the relationship between Stage I pyrite, and the proposed Stage II pyrite

Textural analysis was conducted using reflected and transmitted light microscopy, electron microprobe to further investigate small-scale textural relationships, as well as analyse minerals for chemical constituents that could provide evidence for Stage II pyrite. Photomicrographs were taken to document textural relationships.

Secondly, commercial  $\delta^{34}\text{S}$  isotope analyses were conducted in the stable isotope laboratory of Dr. Kurt Kyser, Queen's University, Kingston, Ontario on a select group of samples. These data allow the parentage of S to be determined.

Two different electron microprobes were used in this thesis, due to acquisition of a new microprobe by the Dalhousie Department of Earth Sciences part way through the study. For consistency, the new microprobe was used only for imaging in the latter portion of the study. Specifications are listed below for both the new and old probe.

The old microprobe system at Dalhousie is run by a Link eXL system paired to a JEOL 733 microprobe. Measurements were conducted using a 15kV accelerating voltage, 15nA probe current, and 1 $\mu\text{m}$  beam diameter. The counting time was 40s, at approximately 7600 total counts per second. Calibration used geological sulphide

standards (chalcopyrite and pyrite) and a ZAF matrix correction program for the reduction of raw data.

The new electron microprobe at the Earth Sciences Department is a JEOL JXA-8200 with five wavelength dispersive spectrometers (WDS) and a Noran energy dispersive spectrometer (EDS). WDS and EDS analysis can be combined. The operating resolution of the EDS is 133eV @ 5.9Kev. The WDS can analyze elements from uranium through to boron. The instrument is capable of automated unattended operation. High quality (1280x1024) backscattered and secondary electron images as well as X-Ray images can be produced by the microprobe. The operating system is Solaris (Unix).

### **1.9 Thesis Organization**

This thesis is organized into two components: The first component is a pyrite study; focusing on the textural relationship between low grade Stage I pyrite with bitumen and the proposed Stage II pyrite. The second aspect of this thesis is a S-isotope study.

## **CHAPTER 2: GEOLOGY OF THE EL SOLDADO DEPOSIT**

### **2.1 Geology, Stratigraphy, and Structure of El Soldado**

The geology of El Soldado has been well documented by several workers, Ruge (1985), Klohn et al. (1990), Zentilli et al. (1997), Wilson (1998), Wilson and Zentilli (1999), and during the course of this thesis, Boric et al. (2002). The following chapter is summarized from them.

The El Soldado deposit is located about 120 km northwest of Santiago, in the coastal range of central Chile (Wilson and Zentilli, 1999). It comprises of a number of locally discordant, but strata-bound, or manto-type, orebody clusters. The horizontal distribution of the deposit is shown in Figure 2.1, which is a plan view at a camp-scale. These orebodies are zoned from the outside inwards with pyrite in an outer halo followed by abundant chalcopyrite, and a bornite-chalcocite core with minor hematite (Figure 2.2) (e.g. Boric (2002); Wilson (1998)).

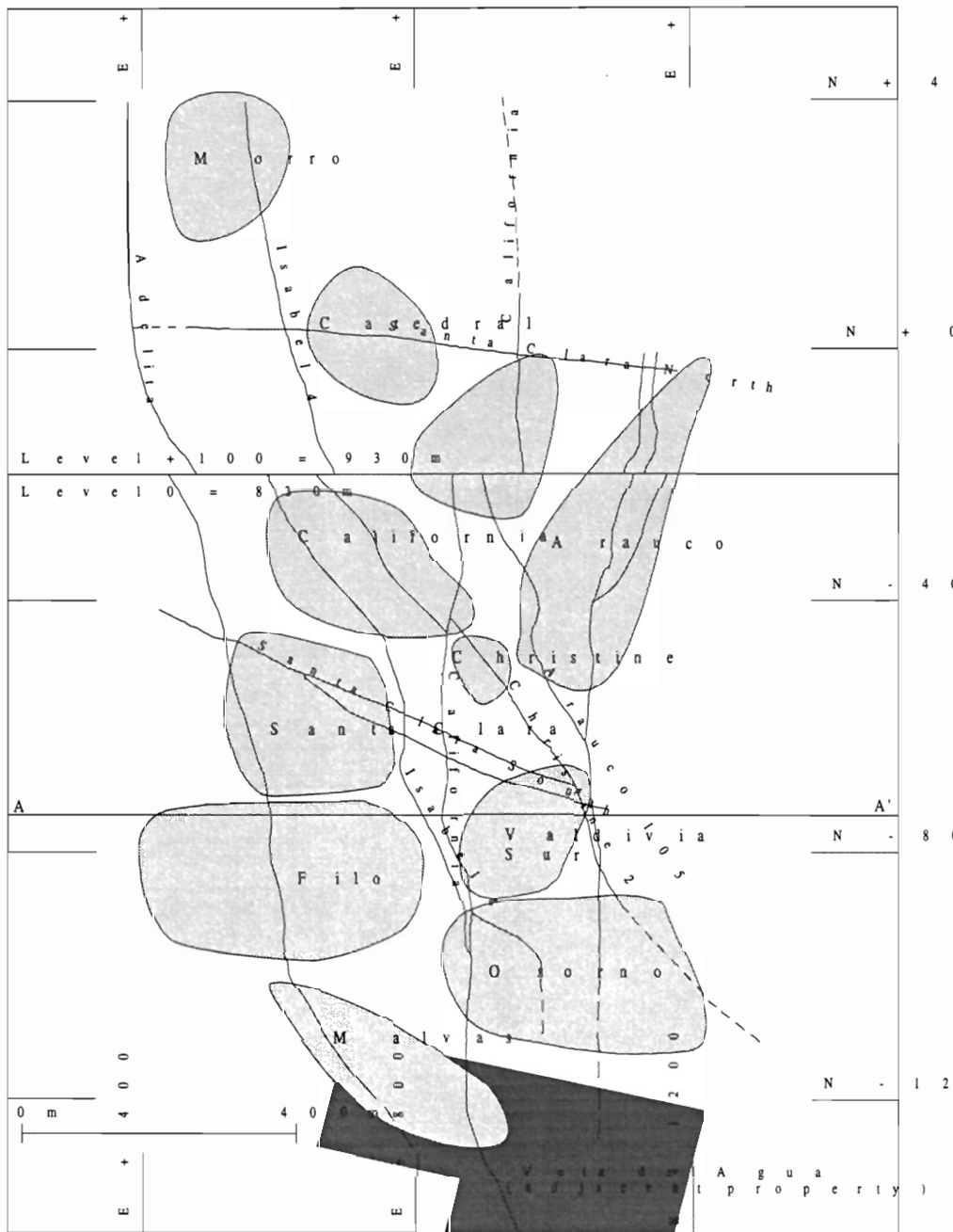


**Figure 2.1: Map of General Orebody Clusters, El Soldado**

Simplified plan section at the level  $\pm 0$  (830 m a.s.l.) and level +100 (930 m a.s.l.) of the deposit outlining the approximate locations of the major orebody clusters. Valdivia Sur is roughly at the N -800 or A – A' line. Morro is in the far north of the deposit. The major N-S and E-W fault sets are represented by the solid and dashed lines. The spatial relationships between orebody clusters are projected onto the plan surface, but vary in vertical location (Modified after R. Sillitoe, CMD Internal Report, 1993).

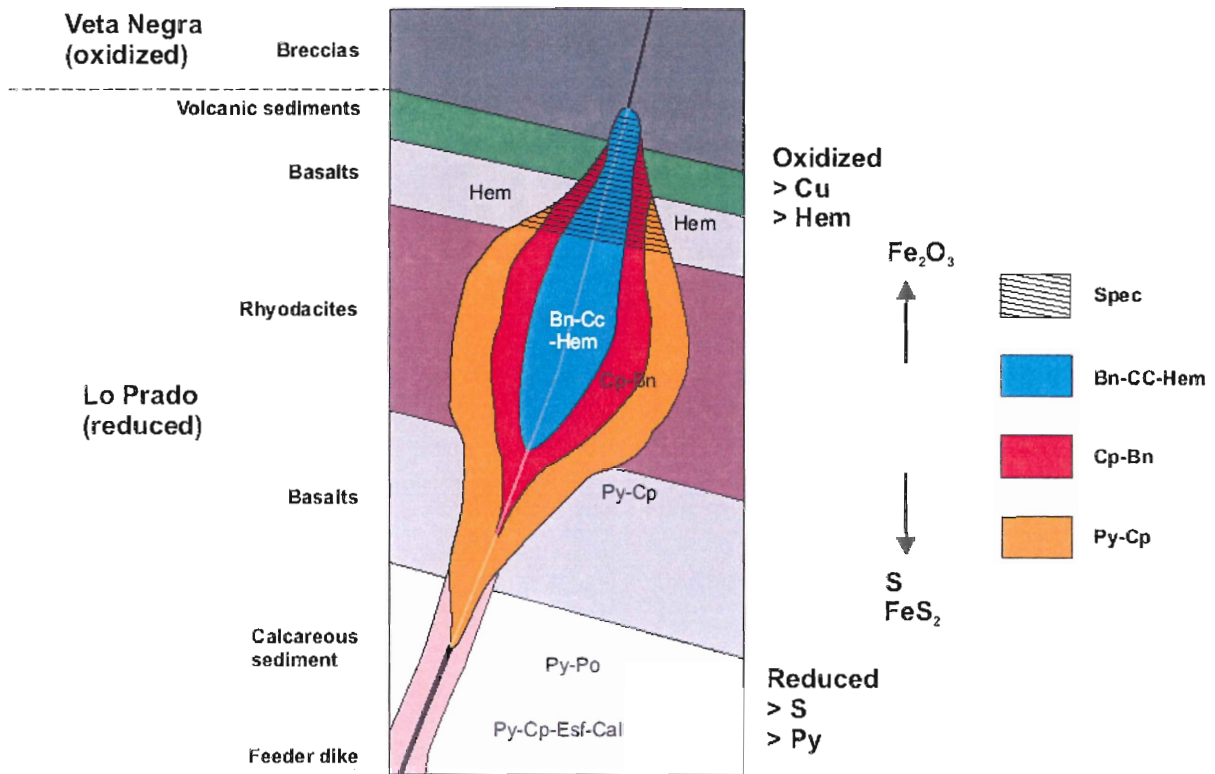


**Figure 2.2: General Zonation of Individual Orebody Clusters**

General illustration of the high degree of zonation of individual ore bodies within the orebody clusters in the deposit. The zonation from the edge to the core increases in Cu grade. The zonation of orebody clusters is discussed in detail later in this chapter. Modified from R. Sillitoe, CMD Internal Report, 1996 and Boric et al (2002).

### **2.1.2 Structure and other field relationships**

Stratigraphically the lowermost unit of the El Soldado deposit is the Upper Jurassic Horquetta Formation, which is a ca. 4 km thick succession of fossiliferous marine limestone. Conformably overlying this are sedimentary units of the Lower Lo Prado Formation. The upper member of the Berriasian- Hauterivian Lo Prado Formation conformably overlies the Lower Lo Prado Formation and is comprised of felsic and andesitic units and hosts the orebody clusters. The Lo Prado Formation is conformably overlain by a 5-7 km thick sequence of basaltic andesites and redbeds that belong to the Barremian-Albian Veta Negra Formation (Boric et al., 2002; Figure 2.3).

The entire sequence is tilted into a ca. 30° east-dipping homocline (Figure 2.4) and regionally metamorphosed to prehnite-pumpellyite, or very low-grade facies (e.g. albite, chlorite, epidote). Upper Cretaceous granitoid bodies occur approximately 13 km east and north east of El Soldado (Figure 2.3; Boric (2002)).



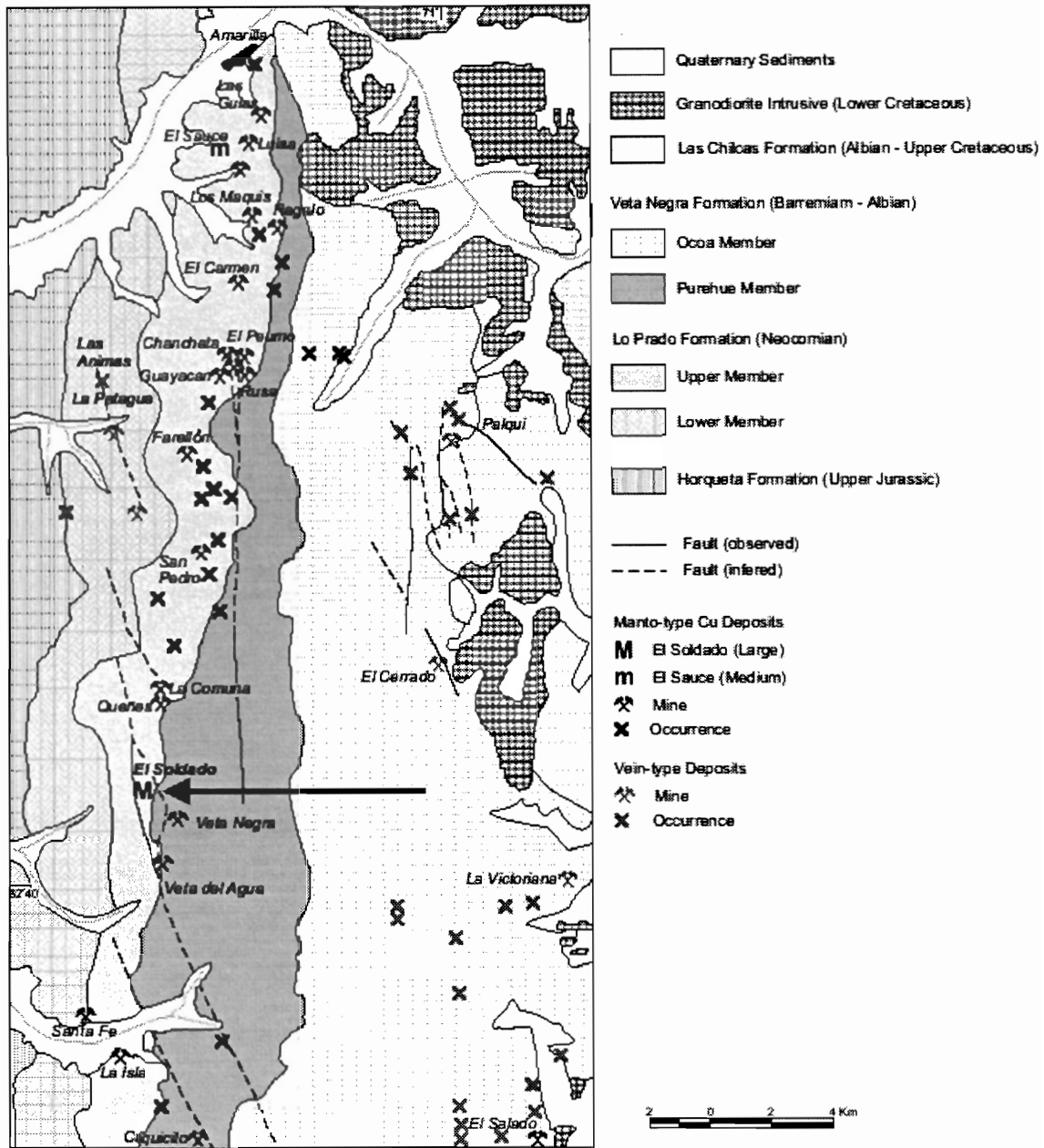


**Figure 2.3 Regional Geology in close proximity to El Soldado**

Geology of the El Soldado and surrounding region. Arrow indicates the El Soldado deposit. Note the high concentration of active mines hosted by the lower Lo Prado Formation. The faults mapped in the El Soldado deposit are concordant with the regional NNW trending strike-slip structural regime. Modified after Boric et al. (2002).

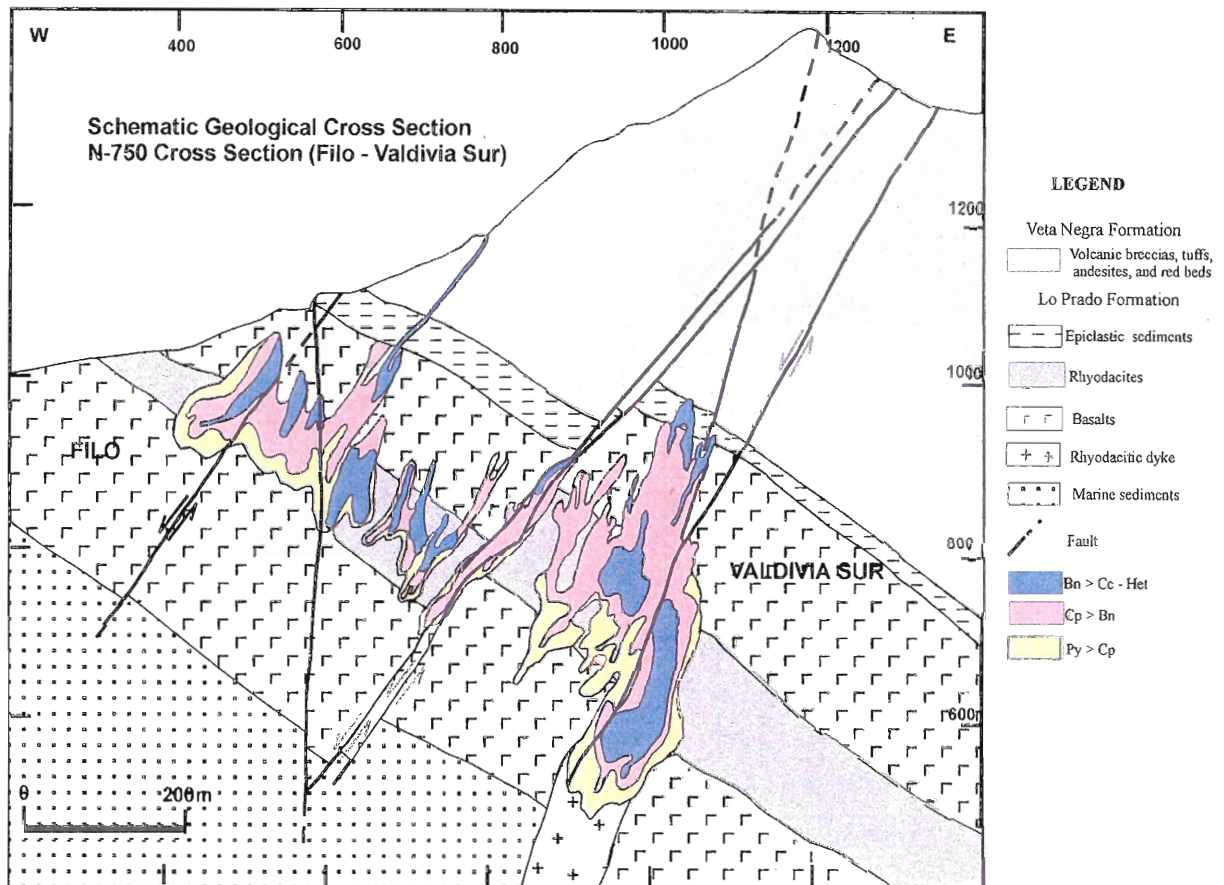


**Figure 2.4 Cross section through Filo and Valdivia Sur orebody clusters**

A cross section of the detailed zonation of sulphide phases cut through the Valdivia Sur and Filo orebody clusters. Note the generally strata-bound nature of the mineralized horizons, but local structural control. Structural control in the orebody clusters occurs mainly where structural permeability has been generated by brittle fracturing, such as in fault intersections, where subvertical (pipe-like) bodies developed. The orebody clusters are zoned horizontally and vertically, where the core has the highest grade and decreases outwards. Samples were collected from the lower zone of the Valdivia Sur, as well as in the northern part of the deposit, not shown in this cross-section. Modified after R. Boric (2002).

An understanding of the geological framework of the El Soldado deposit is important for it is the basis upon which relationships between the ore and bitumen have been made.

### **2.2.1 Lower member of the Lo Prado Formation**

The lower unit of the Lo Prado formation directly underlies the El Soldado deposit. It comprises planar-bedded sandstone, organic-rich siltstone and calcareous shale that is generally organic-rich, exhibits soft sediment deformation and contains finely disseminated sulphides and minor calcite (Wilson, 1998). Along strike, the lower member varies in thickness, but at El Soldado it is ca. 1500 m thick (Wilson, 1998).

Minor disseminated sulphides occur as pyrite, chalcopyrite, sphalerite, galena, and pyrrhotite (Wilson, 1998). The sulphides occur as disseminated grains or lenses and lie on bedding planes, a feature suggestive of a diagenetic origin (Wilson, 1998). Bitumen is found as blebs or fine veinlets within the sediments.

### **2.2.2 Upper member of the Lo Prado Formation**

The upper member of the Lo Prado Formation comprises three main rock types: a rhyolitic unit, basalts and re-worked volcanoclastic sediments.

The felsic component has historically been classified as trachytic in composition mainly indicated by their major element whole-rock chemistry and trachytic texture. Recent work by Boric (2002) indicates the felsic rocks are rhyodacites (Figure 2.5). The rhyodacites occur as flows and domes, as well as their feeder dikes (see below). Within these different forms, texture varies from massive to porphyritic, flow-banded,

spherulitic, vesiculated, autobrecciated, and brecciated (Wilson, 1998). The rhyodacites are most commonly light coloured (e.g. red, green, gray, white).

Bitumen and Cu-sulphides are restricted to fractures, some brecciated zones, and minor vesicles. Many of the fractures are primary fractures, essentially cooling joints (Figure 2.6). Secondary porosity is prevalent, and consists of fractures developed during faulting (Wilson, 1998). Bitumen occurs associated with Cu-sulphides in fractures, while in other places just sulphides occupy the fractures. Where rhyodacites have a columnar jointed form Cu-sulphides occupy the joint surfaces

Minor porosity is also present in breccias, which are present as autobreccias, clast-supported breccias, and tectonic breccias. Autobreccias have little porosity as the flow moulded around the clasts, effectively sealing any possible porosity (Wilson, 1998).

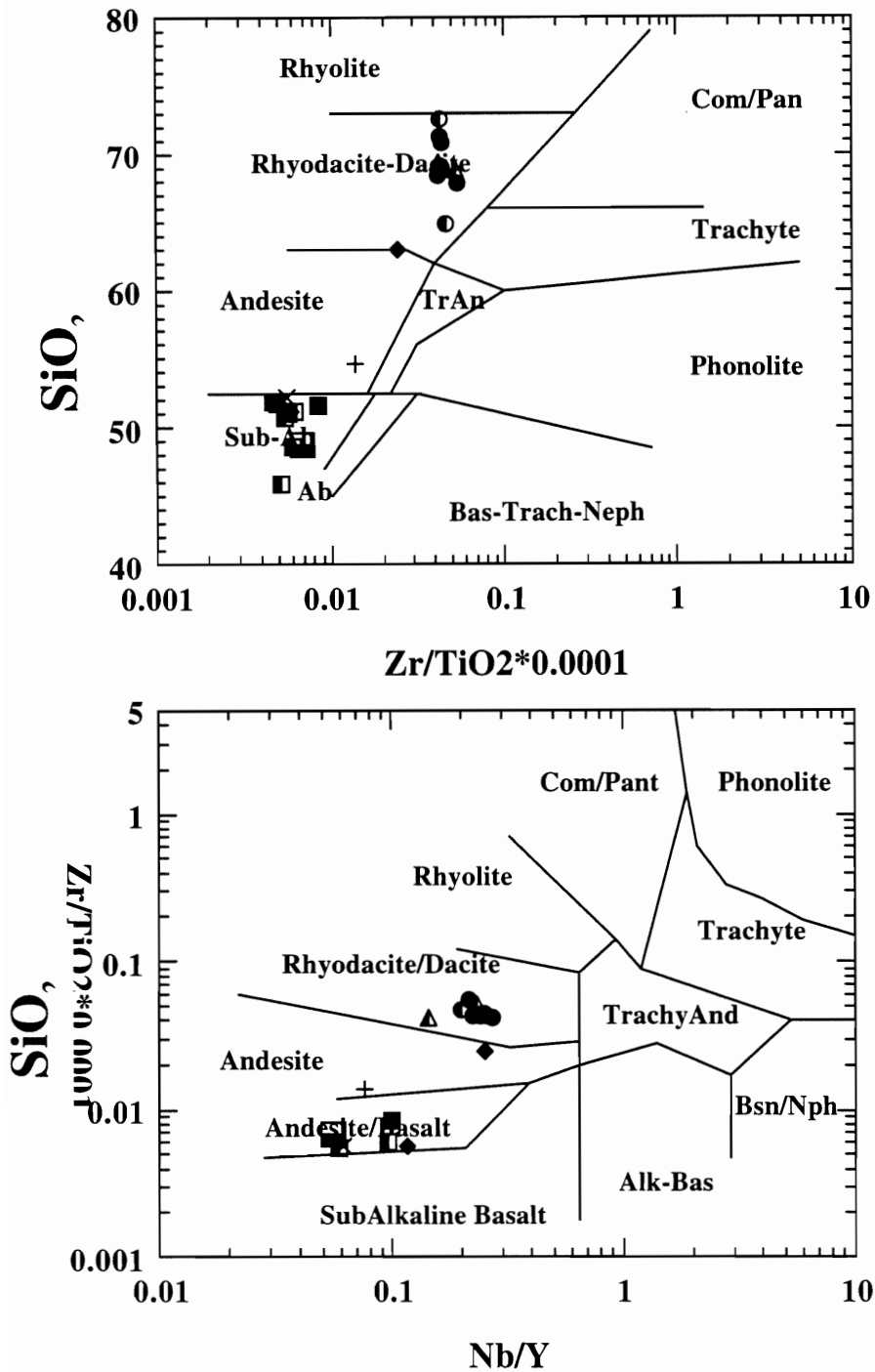


**Figure 2.5: Discriminant plots of El Soldado rocks**

Discriminant plots of El Soldado rocks (filled symbols: unaltered rocks; half filled symbols are weakly altered-pyritized rocks) indicating that the volcanic rocks in the El Soldado deposit are rhyodacites and basalts, not alkaline trachytes and andesites, as interpreted by previous workers. Some dikes are andesitic. Plots after Winchester and Floyd (1977) from Boric (2002). Circle: rhyodacite, square: basalt; triangle: rhyodacitic dike; rhomb: mafic dike; cross is a dioritic dike; "letter X": gabbro stock.



**Figure 2.6: Columnar jointing and faulting in Lo Prado**

Columnar jointing (primary porosity), a dike (1) and a fault (secondary porosity) (2) in the upper Lo Prado Formation. Photo by M.Zentilli.

Clast-supported breccias contain angular blocks of rhyodacite that have been interpreted to have accumulated at the edges of individual flows (Wilson, 1998). These breccias have excellent primary porosity, and are commonly filled by Cu-sulphides, bitumen, and gangue minerals (Wilson, 1998). Tectonic breccias are those that formed through later brittle faulting of the rhyodacite. Bitumen, sulphides, and gangue minerals occupy most available porosity.

The mafic suite of rocks at the El Soldado camp are (alkali metasomatized) basalts (Boric, 2002). Basalts have a porphyritic texture, and generally are green or black. They are composed of plagioclase, rare augite phenocrysts in a groundmass of randomly oriented plagioclase laths (mostly albitized) with interstitial K-feldspar, clinopyroxene (chloritized), and some devitrified glass (Klohn et al., 1990).

Amygdules are filled with calcite, quartz, chlorite, bitumen, and Cu-sulphides. Brecciation is inferred to be mostly tectonic, although some might be primary (Wilson, 1998). Fault-brecciated basalts are commonly mineralized in the inter-breccia space. Associated with the fault-breccias are bitumen, gangue, and sulphide minerals (Wilson, 1998).

Volcaniclastic rocks of the Lo Prado Formation are present at the boundary between the upper Lo Prado Formation and the overlying Veta Negra Formation. Porosity varies with grain size, where the smaller the grain size, the less porosity. Within a sample, grain size varied considerably within a few centimetres, with bitumen present in the coarser-grained samples (Wilson, 1998).

According to Wilson (1998), the bitumen distribution in the epiclastic rocks of the Lo Prado Formation is the same as that observed in coarse-grained sedimentary units

where petroleum has migrated along primary porosity. The low porosity of the volcanoclastic unit appears to have acted like a cap rock, effectively sealing the units and preventing further petroleum migration (Wilson, 1998).

At the northern end of the deposit, mine geologists have mapped intrusive rhyodacitic bodies (Figure 2.6, Boric, 2002). Cross-cutting relationships between feeder-dikes from the intrusives and pyrite-bitumen veins indicate that at the time of petroleum flow, the intrusions cooled to temperatures compatible with the flow of liquid petroleum (<140°C; North, 1985).

### **2.3 Previous Economic Geology Studies.**

The following account of the ore geology of the El Soldado copper deposit has been summarized from Wilson and Zentilli (1999), Klohn et al. (1990), Boric (1997), Wilson (1998).

#### **2.3.1 Mineralogy of the Orebody Clusters**

The El Soldado deposit comprises numerous isolated ore bodies with intervening barren zones that are distributed in about a dozen clusters or zones (Wilson and Zentilli, 1999). These ore zones are referred to as *orebody clusters*, because of their 3D form, which is not as one discrete orebody, but many small clusters of ore, and also to avoid confusion with the term *zone*, which is often used to describe metamorphic or mineralogical zoning. The orebody clusters are distributed in a volume of rock approximately 2 km long by 0.8 km wide and 600 m thick (Figs. 2.1, 2.4). The size of



individual ore blocks is highly variable, ranging from 100 to 450 m in length, 30 to 150 m in width, and 80 to 250 m in height (Klohn et al, 1990).

Ore mineralogy is characterized by chalcopyrite, bornite, and chalcocite. Gangue minerals are abundant, present as calcite and pyrite, hematite and minor amounts of sphalerite, galena, and arsenopyrite (Wilson and Zentilli, 1999). Individual orebodies are zoned, with a pyrite halo at the fringes of the orebodies, followed inwards by abundant chalcopyrite, and a bornite-chalcocite core with minor hematite (Figure 2.3; Wilson, 1999).

The orebody clusters are structurally controlled, preferentially developed within a NS to NNW trending regional fault system, notably where NS, EW, and NW trending faults intersect (Figure 2.7); Wilson and Zentilli, (1999). Due to the structural control on mineralization, the lateral limits of the ore bodies are characterized by abrupt lateral changes in mineralogy and Cu grade.

### Regional Structure

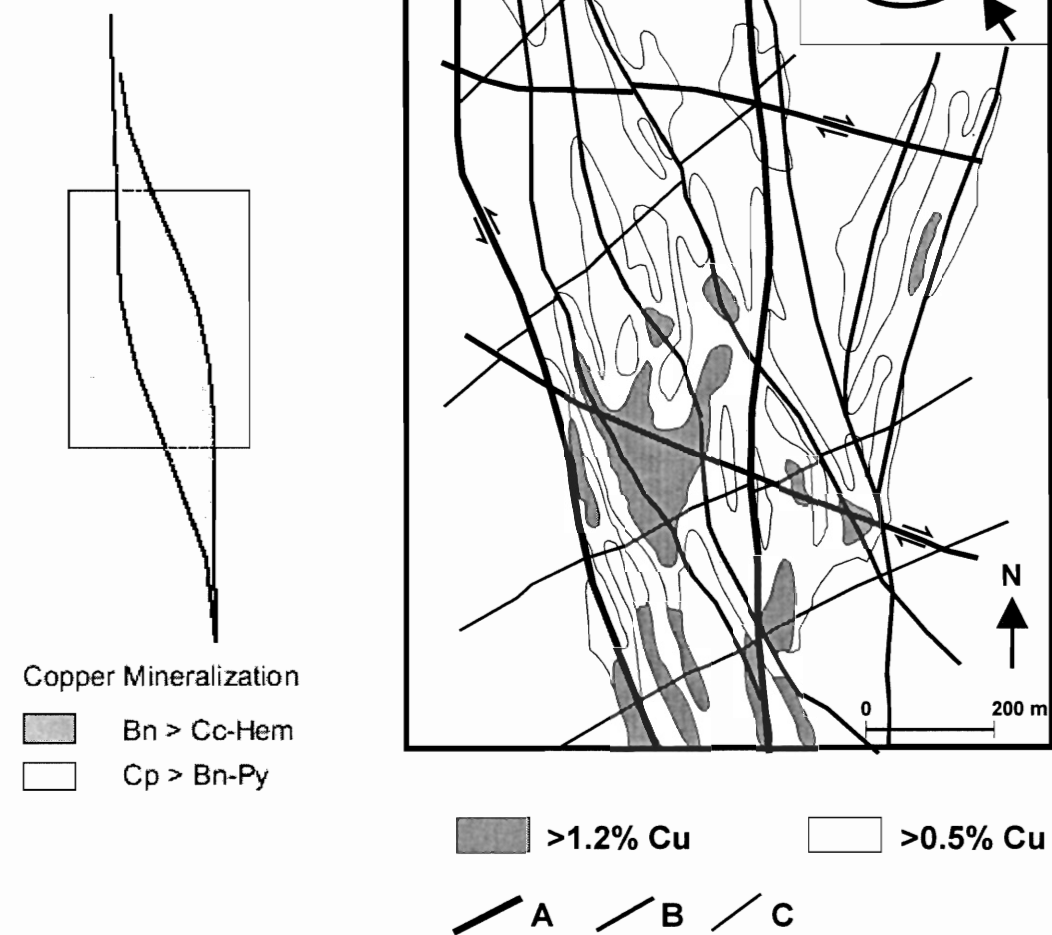


### Figure 2.7: Camp-scale structural characteristics

Illustration showing the strong structural control on the deposit zonation. Most large, high-grade orebody clusters are at the locus of major fault intersections, and have a vertical extension. The regional structure is developed in a dilational jog of a sinistral strike-slip brittle shear system. Modified from (Boric et al., 2002)

A, B & C are fault size in decreasing order.

The wall rock between ore bodies is generally barren (below 0.15 % Cu) Klohn, (1990). Away from the structurally controlled regions Boric (1997), describes the mineralization as veins. Lithological control is influenced by relatively brittle rhyodacite flows and their intrusive feeders, which have a higher degree of mineralization than basalt flows and tuffs (Ruge,1981) Dikes are generally barren Boric (1997).

District zoning is evident, whereby the southern orebody clusters have relatively more chalcocite and bornite but in the north chalcopyrite is the dominant sulphide e.g. Martin, 1981; Gonzalez and Holmgren, 1993; Boric, 1997; Boric, 2002. The zonation of sulphides according to grade appears to be related to pyrobitumen abundance. Where high amounts of pyrobitumen are present, the grade of sulphides is generally higher than in regions with relatively less pyrobitumen Wilson, (1998).

### **2.3.2 Paragenesis of the sulphides**

The El Soldado deposit was formed in two distinct stages, each under differing conditions.  $^{40}\text{Ar}/\text{Ar}^{39}$  geochronology data indicates the first stage formed approximately 130 M.y. ago. Wilson (1998), and Wilson and Zentilli (1999) postulated that a diagenetic, low temperature (<120° C) process, that was coeval with liquid petroleum migration, accumulation, and degradation constitutes *Stage I*. The second assemblage formed approximately 20 Ma later, and is known as *Stage II* henceforth.

In Stage I, during petroleum accumulation, abundant pyrite framboids were formed with probable help from sulphate-reducing bacteria. In response to increasing temperatures, framboidal pyrite developed into euhedral or massive pyrite. Accessory sulphides in Stage I include minor amounts of sphalerite, sphalerite with inclusions of

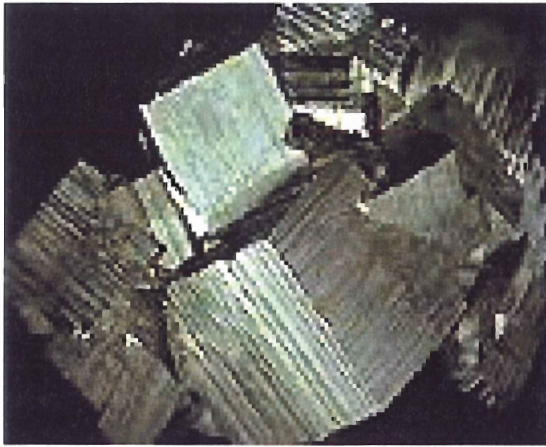
chalcopyrite Wilson, (1998), and very rare arsenopyrite Zentilli et al., (1997) that exists within the early sulphide assemblage. Also prominent in Stage I is organic matter, which occurs as bitumen or pyrobitumen, and represents thermally and biogenically altered petroleum (Boric et al., 2002)

Stage II sulphides include chalcopyrite, bornite, and chalcocite, which were deposited ca. 20 Ma after petroleum migration and accumulation. Chalcopyrite was the first Cu sulphide to replace Stage I pyrite, and was followed by bornite, chalcocite and covellite replacement. In high-grade zones, the framboidal pyrite structure is still preserved. The Stage II phase of deposition was much hotter than previous events and resulted in the thermal alteration of bitumen to pyrobitumen Wilson and Zentilli, (1999). Bitumen caused a change in fluid stability resulting in the precipitation of the Cu sulphides from solution.

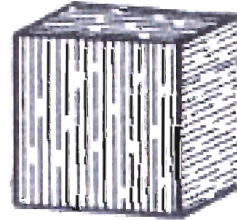
### **CHAPTER 3: PYRITE STUDY: UNDERSTANDING THE PYRITE CHARACTERISTICS OF EL SOLDADO**

This chapter includes a description and discussion on the origin of pyrite framboids in sediments and ore deposits, with an emphasis on the process of formation of framboids. The geochemistry of pyrite is presented to establish the framework for the discussion of the probable role of pyrite in the formation of the El Soldado deposit. A brief background section on the crystallography, structure and chemistry of pyrite follows so that a framework is created for this section, which deals with aspects of pyrite, and compositional variation.

Pyrite,  $\text{FeS}_2$ , is a cubic mineral with a specific gravity of 4.95 to 5.03  $\text{g cm}^{-3}$  and a hardness of 6 to 6.5. It has a brassy yellow colour in air, and is pale yellow to white in reflected light microscopy; fine-grained samples can be black. Pyrite has poor cleavage on {001}. Although cubic (Figure 3a, b (i)) pyrite also exists as octahedral (Figure 3b (ii)) and more commonly as pentagonal dodecahedron (pyritohedron) (Figure 3a, b (iii)) e.g. Deer et al., 1992; Ramdohr, 1980; Bennet et al., 1965 as Figure 3.0b illustrates. Pyrite also has a dimorph, marcasite (Figure 3.0a(ii)), which does not share the same crystal structure or lattice arrangement as pyrite, but does share the same composition,  $\text{FeS}_2$ .  $\text{FeS}_2$  formed from a colloidal gel is referred to as *melnikovite pyrite* (e.g. Deer et al., 1992; Ramdohr, 1980). Pyrite can accommodate some impurities or solid solution in its chemical structure, allowing minor incorporation of Ni, Co, Mn, Cu, As (Deer et al., 1992).



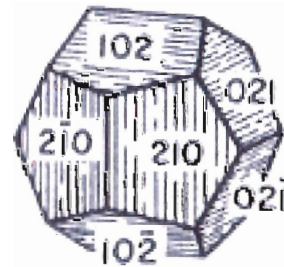
(i)



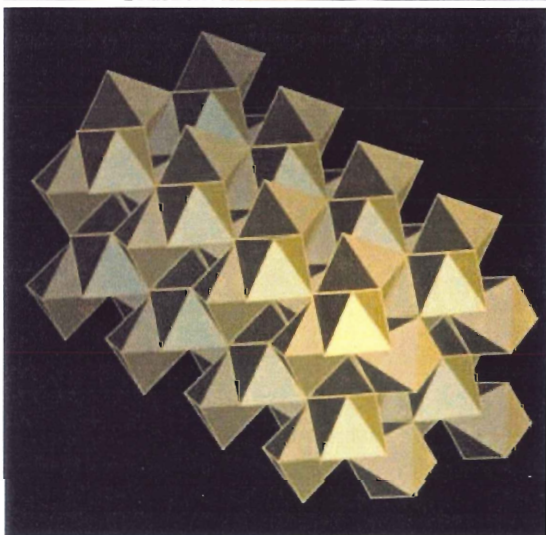
b(i)



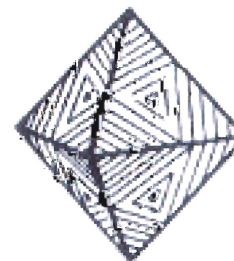
(ii)



b(ii)



(iii)



b(iii)

**Figure 3.0a,b: Pyrite morphology and crystallography**

3a (i) <http://www.theimage.com/mineral/pyrite/pyrite.html>

3a (ii) <http://mineral.galleries.com/minerals/sulfides/marcasit/marcasit.htm>

3a (iii) <http://www.chem.ox.ac.uk/mom/pyrite/pyrite.html>

### **3.1.1 Introduction**

In the El Soldado Cu deposit, pyrite is omnipresent throughout the orebodies. It occurs in several different forms, including massive pyrite aggregates, as well as in a framboidal form. The distribution of pyrite in El Soldado falls into two main categories. As noted before, the orebodies have a concentric zonal pattern, in which highest-grade copper sulphide minerals such as chalcocite and bornite are located in the core of the orebody. Moving outwards to the periphery of the orebodies, the grade and Cu/Fe ratio decreases. At the edge of the orebodies pyrite occurs as a halo surrounding the copper sulphides. This pyrite is framboidal or massive in texture. The other pattern of orebody zonation is a vertical zonation whereby the tops of the orebodies exhibit the highest Cu/Fe sulphides, and with increasing depth the ore decreases in grade and Cu/Fe. At the base of the orebodies, massive pyrite veins, or roots are present.

### **3.1.2 Framboidal Pyrite**

Framboidal pyrite has been identified in ore districts of many different styles for over a century (Otswald and England, 1979) and was first described by Rust (1935). Despite many field and experimental studies, the formation mechanism of framboids remains in question. To date, convincing data has not been presented to fully explain the formation processes.

Framboids are spherical aggregates of individual microcrysts that have the appearance of raspberries (framboise = French word for raspberry). They are predominantly composed of pyrite, and rarely as magnetite (Figure 3.1) (Rickard, 1970; Sawlowicz, 1992; Wilkin and Barnes, 1997a). Framboids have been observed forming in

modern anoxic environments such as salt marshes, and argillaceous marine and lacustrine sediments. Framboidal pyrite may be found forming in the water columns of modern anoxic basins, e.g. the Black Sea (Berner, 1970). Pyrite with a framboidal morphology has been preserved in sediments of shale, carbonate, and coal from as old as the Proterozoic (Wilkin and Barnes (1997a); Rickard (1970)). Clearly, if framboids have been forming for this long, and modern framboids and ancient ones have essentially the same characteristics, the process of formation must be a stable and consistent one, and there is the possibility of more than one mode of formation.



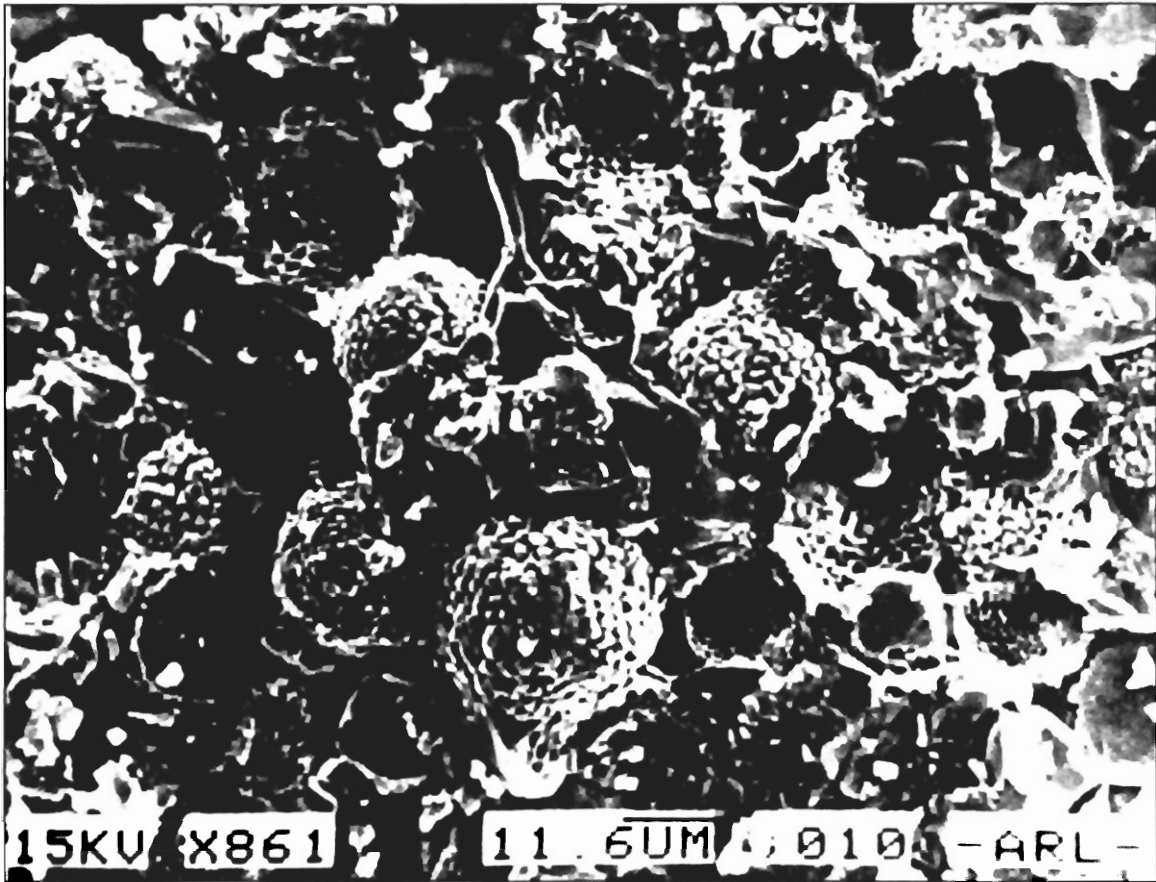


**Figure 3.1: SEM of framboidal pyrite**

This image is a scanning electron microscope image (SEM) of framboidal pyrite. Note their spheroidal nature, and size. Individual microcrystals, which form the framboids, can be clearly observed in this image (From Wilson, 1998).

### **3.1.2.1 Origin of framboids**

Two main hypotheses are most accepted for the formation of framboidal pyrite. One idea is that inorganic processes form framboids and no organic matter is required for any part of their formation. The second hypothesis states that organic processes, such as the involvement of certain bacteria, as well as organic components are necessary to form framboids. Many workers have now come to believe that a combination of organic and inorganic processes works in unison to form framboids. Following is a brief summary of both hypotheses.

### **3.1.2.2 Inorganic Processes Related to Framboid Formation**

Formation of framboids by inorganic means has been studied in detail by Berner (1969b, 1970), Wilkin and Barnes (1996), Rickard (1969, 1975), and others. In laboratory experiments, workers have been able to synthesize pyrite under conditions expected for typical marine sediments undergoing early to late diagenesis, that is pH (6-8) (refer to Figure 3.2), and temperature ( $>25^{\circ}\text{C}$ ,  $<70^{\circ}\text{C}$ ; e.g. Wilkin and Barnes, 1996). Also formed synthetically in laboratory experiments, below  $100^{\circ}\text{C}$  are (1) amorphous iron sulphide ( $\text{FeS}_{0.9}$ ) (2), mackinawite ( $\text{FeS}_{0.9}$ ) (3) cubic iron sulphide ( $\text{FeS}$ ) (4) hexagonal pyrrhotite ( $\text{FeS}_{1.1}$ ) (5) greigite ( $\text{Fe}_3\text{S}_4$ ) (6) smythite ( $\text{Fe}_3\text{S}_4$ ), and finally (7) marcasite, or orthorhombic  $\text{FeS}_2$ . The source of sulfur and iron in these experiments was controlled such that the path of the ions in question could be traced. Upon completion of the experiments, some of which lasted several months, microscopic analysis of the minerals was conducted using

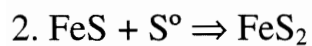
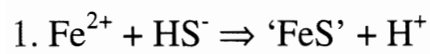
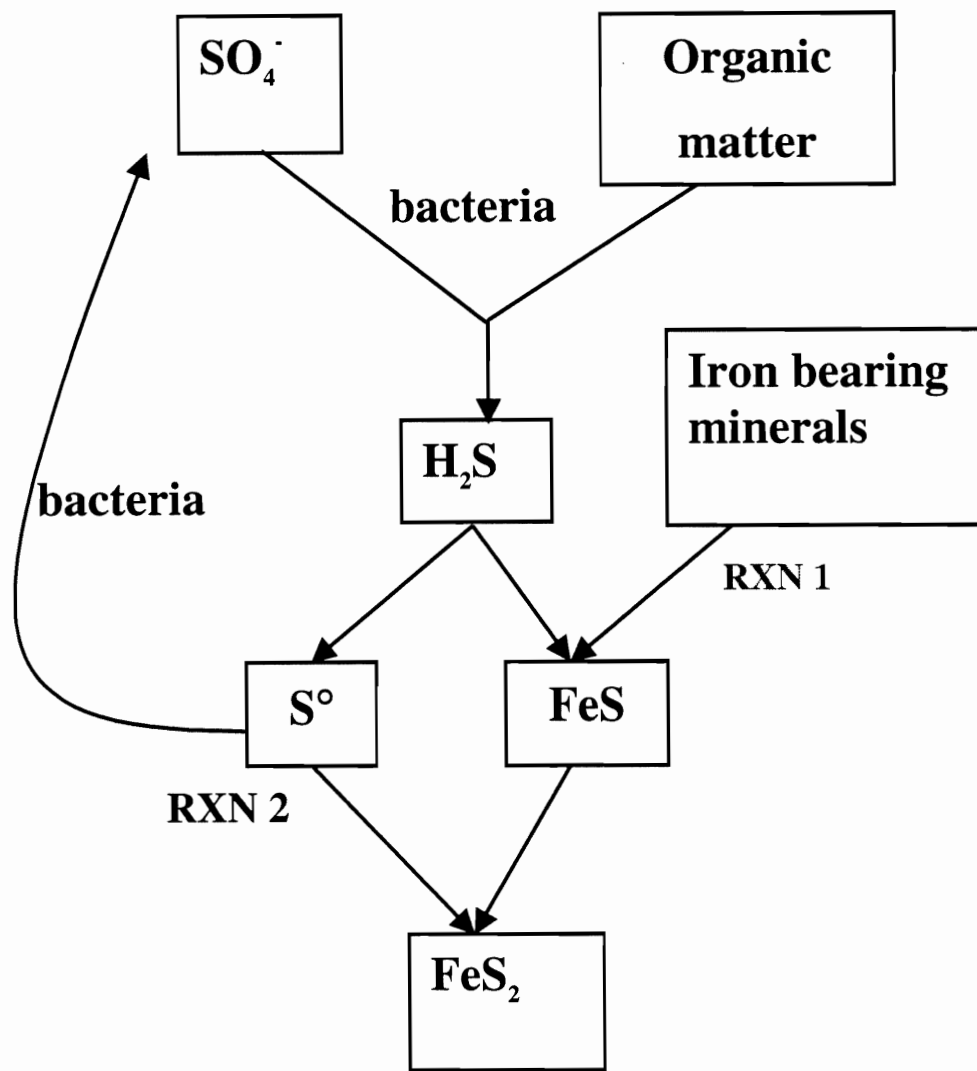


**Figure 3.2: Possible sulphur pathway**

Possible multistage path followed by iron and sulphur follows as they are converted to pyrite. An explanation of the pathway is given in the text. Modified from Berner (1985).

reflected light microscopy and X-ray diffraction. In some cases,  $\delta^{34}\text{S}$  analysis before and after experiments was conducted to trace the path of S. There is a general consensus among the inorganic experiments as to the path that results in the formation of pyrite framboids. It should be noted that this path might be applied in a modified form to many proposed organic modes of formation. The path includes four consecutive processes: (1) nucleation and growth of initial iron monosulphide microcrystals; (2) reaction of the microcrystals to greigite ( $\text{Fe}_3\text{S}_4$ ) or mackinawite ( $\text{Fe}_9\text{S}_8$ ); (3) aggregation of uniformly sized greigite microcrystals, i.e. framboid growth; and (4) replacement of greigite framboids by pyrite (Figure 3.3) (Wilkin and Barnes, 1996).

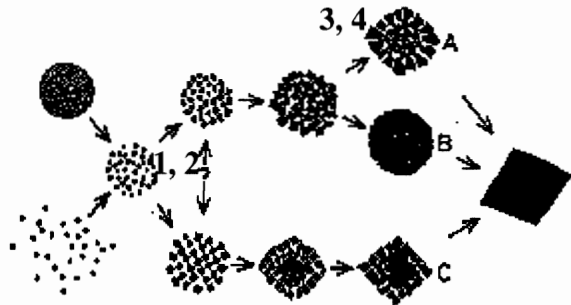


**Figure 3.3: Possible pathway for the formation of framboids**

The physical pathway for the formation of framboids. The diagram has been modified to illustrate the general stages for chemical conversions that ultimately result in framboidal pyrite, or annealed cubic pyrite. Chemical analysis can be performed to reveal chemical zonation of recrystallized framboids

Microscopic analyses of synthesized pyrite grains revealed they occurred only as aggregates of crystals embedded on the surface of orthorhombic sulfur grains (Berner (1970). Since the work of Berner (1970), however, others have produced pyrite without sulfur cores (Wilkin and Barnes, 1997a). At very high magnification, microspheres of pyrite with an average grain size of  $\sim 1\mu\text{m}$  in diameter are observed. The texture of the

aggregates reveals that they were comprised of even smaller crystals. Berner (1970) recognized this texture as similar to framboidal textures that form in natural sediments.

### **3.1.2.3 Organic Processes Related to Framboid Formation**

Scientists have debated the involvement of an organic component in the formation of framboids. Workers such as Schneiderhöhn (1923), Rust (1935), Ramdohr (1960), Rickard (1970), and Sawlowicz (1992) have argued that processes requiring the contribution of organic matter, or a biological agent, are needed to form framboids. The following is a brief summary of the concepts and ideas advanced by them.

In the pioneering days of framboid formation research, workers such as Rust (1935) and Ramdohr (1960) believed that framboids represented fossilized bacteria, or cells, that were subsequently pseudomorphed by pyrite, or other sulfides. With major advances in microbiology, however, there remains no discovery of an organism that filled the role, and no intermediate stages of replacement have been observed (Wilson, 1998). Experiments by Kashefi et al. (2001), using hyperthermophilic and mesophilic dissimilatory Fe (III) Bacteria and *Archaea* were able to precipitate Au(0) under certain conditions. Although these experiments used gold as a reactant, the experiments have advanced the theory that special bacteria could potentially play a role in framboid formation.

Many workers have proposed bacteria as an intermediate stage in the formation of framboids (Rickard, 1970; Berner, 1970; Wilkin and Barnes, 1997a). In modern sediments, Berner (1970) and others have noted that as organic matter accumulates at the sediment-water interface, bacteria subsequently metabolize it (Figure 3.2). This results in

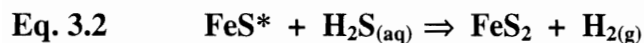
the removal of oxygen from the water, and formation of  $H_2S$ , a waste product of the bacteria, and an essential component in the formation of precursor iron monosulphides, which are eventually replaced by pyrite. An alternate means by which organic matter may facilitate framboid formation does not require bacterial involvement, but relies instead on organic globules. Rickard (1970) proposed that the spheroidicity of framboids does not arise by a physical property of the Fe-S-water system, but rather by pseudomorphing iron monosulfides of a preexisting spheroidal shaped object, or void (e.g. gas vacuole - inorganic). Rickard noted that in many modern types of sediment, there exist immiscible organic globules that are most stable in a spheroidal configuration, which represents the lowest surface free energy. If there are sufficient components e.g. Fe and S, then the formation of iron monosulphides can occur at the expense of the organic globule, essentially replacing it and taking its spheroidal form. Rickard and others have proposed this explanation because in many cases an organic film, or particles of organic material are observed enclosed within the framboids.

### **3.1.3 Discussion**

The processes that lead to the formation of framboids are not well constrained or understood, thus controversial, and often conflicting. Framboids occur in many different rock types, yet retain a morphology that appears to be independent of host rock. Also, because of the similarity between modern and ancient framboids, the process appears to have developed long ago, remaining largely unchanged since the Proterozoic.

There are several problems with both the organic hypothesis, and inorganic hypothesis. Neither is able to explain, or prove conclusively what processes actually form

framboids. Many explanations are feasible, but there is simply not enough evidence to provide a high level of confidence. Many of the inorganic models work at a basic level – in an experiment using inorganically derived constituents, but in nature these constituents are most easily supplied by organic means, making a composite model seem most logical. For example, in the experiments of Berner (1970), and other similar experiments, such as Wilkin and Barnes (1996), there was fixed control on the iron and sulphur species involved in the formation of precursor iron monosulphides. However, not all these species are commonly nearby in natural environments, making the experiments unrealistic. In fact, Berner (1983), states that although inorganic sulphur was used in his experiments, a viable and common source of sulphur in nature is generally from bacterial processes. Pyrite forms from the reaction of H<sub>2</sub>S derived via the bacterial reduction of seawater sulphate in anoxic sediments, with detrital iron minerals Berner (1983). Bacterial sulphate reduction is accomplished by the oxidation of organic matter via reaction 3.1. Equation 3.2 is the second stage in pyrite formation, and generally uses H<sub>2</sub>S from Eq. 3.1.



\*FeS represents precursor iron monosulphides such as greigite and mackinawite

A general problem with the formation of framboids inorganically is that the sulphur source used in the experiments is often not readily available in natural systems: nature is rarely as consistent as experiments.

There are also many problems with the theories presented in support of purely organic processes. One of the main problems is the occurrence of framboids in systems where the introduction of organic material is virtually impossible, such as magmatic deposits, or hydrothermal systems, which can exceed temperatures of 300°C. Sunagawa et al. (1971) synthesized framboidal pyrite at high temperatures (~300° C) that was virtually indistinguishable from sedimentary framboids formed at considerably lower temperatures. The lack of organic material in general is a strong limiting factor in this theory, because not all occurrences of framboids have organic matter associated with them, yet regardless of host lithology, the framboids are consistent.

In order to sum up the wide range of theories related to the genesis of framboids, and more specifically pyrite framboids, which are an essential component in the formation of the El Soldado deposit, Table 3.1 lists organic and inorganic means of formation and lists pros and cons for each theory. The pyrite in the El Soldado deposit, both massive and framboidal, has clear textural indications that it was replaced by copper sulphides in Stage II of mineralization (see Chapter 4 for textural descriptions of samples).



**Table 3.1 Weighting different framboid arguments**

Inorganic Processes		Organic Processes	
Pros	Cons	Pros	Cons
<ul style="list-style-type: none"> <li>• synthesis of framboids consistent with natural morphology- shows it is possible</li> <li>• chemical/physical properties used to explain spheroidicity</li> <li>• experiments partially define mechanisms &amp; constraints of pyrite formation (T and pH)</li> </ul>	<ul style="list-style-type: none"> <li>• experimental constraints often not viable in natural systems e.g. FeS gels or colloids as precursor to FeS<sub>2</sub></li> </ul>	<ul style="list-style-type: none"> <li>• explains organic films in some framboids</li> <li>• explains high frequency of occurrence in petroleum deposits/reservoirs</li> <li>• readily available S via Eq 3.1</li> <li>• explains wide <math>\delta^{34}\text{S}</math> ranges, which are not always consistent with inorganic constraints</li> </ul>	<ul style="list-style-type: none"> <li>• doesn't explain magmatic or hydrothermal framboids</li> <li>• often no organic film</li> <li>• doesn't completely explain spheroidicity</li> </ul>

### 3.1.4 Conclusion

The formation of framboids, either organic or inorganic, are not well defined to make any indisputable statements regarding the processes responsible for their formation. To refine the model of formation, several aspects must be considered. First, one must distinguish between chemical and physical processes that result in the nucleation and crystallization of precursor iron monosulphides and ultimately pyrite microcrysts, as well as the spatial organization of microcrysts into framboidal aggregates. In addition, the source of chemical components such as Fe and S, organic or inorganic, as defined by a particular model must be accounted for (Wilson, 1998). Using observations from the specific location of framboid occurrence to constrain the mode of local formation may be a viable short-term solution for explaining framboid formation.

It is the opinion of the author that the most viable explanation for framboid formation may be a composite model. The physical (i.e. inorganic) processes that combine to form framboids appear to be fixed in nature, such that the lowest possible energy configuration is preferred. The most viable source of chemical constituents (i.e. S) is from bacterial action, which is also nature's lowest energy source, requiring much less energy than inorganic means (Nielson, 1979). Bacterial processes are restricted to low temperatures, and so are most deposits the framboids are found in (e.g. El Soldado, Chile; White Pine, Michigan; Kupferscheifer, Europe).

## **3.2 Pyrite Geochemistry**

### **3.2.1 Introduction**

This section covers the geochemical aspects of El Soldado. Many of the observations at El Soldado can be constrained using geochemical diagrams, allowing further explanation of mechanisms in operation to be defined, and the overall paragenesis to be explained. This includes phase diagrams of Fe and Cu sulphides, stability diagrams and several reactions that help define replacement reactions.

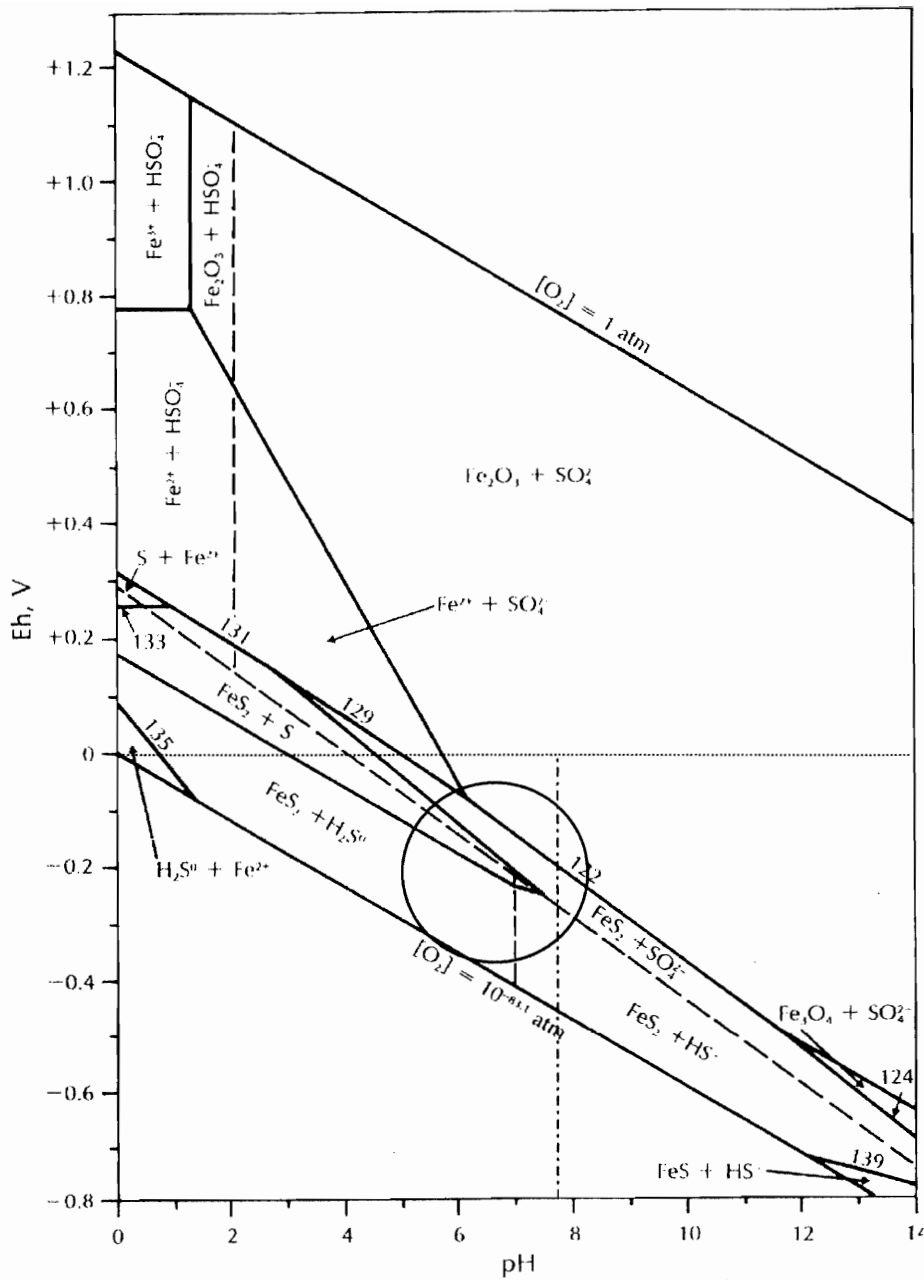


**Figure 3.4: Eh-pH diagram for Fe oxides and sulphides**

A composite Eh-pH diagram for Fe oxides and sulphides in the presence of water at 25 °C containing  $\Sigma S = 10\text{Fe-}1 \text{ mol/L}$ . Dashed lines indicate the conditions under which the different S species become dominant. Numbers adjacent to some lines are correlated to equations not presented in this chapter. Below horizontal dotted line represents stability of bitumen, and to the right of the dash-dot line is the stability field of calcite. Based on field relationships the implied environmental conditions at El Soldado are roughly inside the circle in the centre of the diagram. Faure (1991); Modified after Garrels and Christ, 1965).

Figure 3.4 is important because it helps set limits on the chemical environment in which the Stage I assemblage formed. Bitumen stability is plotted at Eh below 0 Volts; the presence of bitumen in most orebody clusters a negative Eh environment, or a reducing environment, which is consistent with chemical requirements for the formation of framboidal pyrite via reducing bacteria. Calcite precipitated after solidification of petroleum, in shrinkage cracks and veinlets, at temperatures above 100 °C (Boric et al., 2002), hence calcite was not a stable phase when pyrite was growing (low pH due to H<sub>2</sub>S) inside or around liquid petroleum.

### **3.3 $\delta^{34}\text{S}$ Isotope Geochemistry**

#### **3.3.1 Introduction**

Four stable isotopes, with the following relative abundances, characterize sulphur (Nielsen, 1979):

$$^{32}\text{S} \approx 95\%$$

$$^{33}\text{S} \approx 0.77\%$$

$$^{34}\text{S} \approx 4.2\%$$

$$^{35}\text{S} \approx 0.01\%$$

Using the differences in relative proportion as well as the specific atomic mass of sulphur, samples can be analysed and some judgment made as to the processes that combined to give the specific isotopic ratio. This study used the most common ratio (R =

$^{34}\text{S}/^{32}\text{S}$ ) used for studying terrestrial rocks, which utilizes the two most abundant stable isotopes of sulphur (Nielson, 1979).

The notation used most frequently in reporting sulphur isotope data is  $\delta$  - notation:

$$\delta^{34}\text{S} (\text{‰}) = \frac{(\text{R}_{\text{sample}} - \text{R}_{\text{standard}})}{\text{R}_{\text{standard}}} \times 1000$$

**Eq. 3.3**

### 3.3.2 Geochemistry of $\delta^{34}\text{S}$ Sulphur

In nature the concentration of  $\delta^{34}\text{S}$  ranges from  $\sim -65\text{‰}$  to  $\sim +95\text{‰}$ , where most samples fall in the  $\pm 40\text{‰}$  range. According to Nielson (1979), sulphur has the most efficient isotopic fractionation process in nature, due in part, to the wide range of redox states that sulphur can exist in. Sulphur occurs as  $\text{S}^{2-}$ ,  $\text{S}^0$ ,  $\text{S}^{4+}$ ,  $\text{S}^{6+}$ , as well as the following metastable complexes  $\text{S}_2^{2-}$ ,  $\text{S}_3^{2-}$ ,  $\text{S}_4^{2-}$ ,  $\text{S}_5^{2-}$ ,  $\text{S}_6^{2-}$ , and  $\text{S}_2\text{O}_3^-$ , which result from mild oxidation conditions. The most stable form is  $\text{S}_2^{2-}$  (also known as  $\text{S}^{1-}$ ), and bonds with  $\text{Fe}^{2+}$  to form pyrite, which is the most abundant sulphide mineral in sedimentary rocks (Nielson, 1979).

The energy required to reduce sulphate ( $\text{SO}_4^-$ ) by inorganic means requires relatively high activation energy. In natural systems the temperature required ( $\sim 200^\circ\text{C}$ ) to reduce sulphate confines it to deep crustal reactions. However, by enzymatic complexing of the sulphate ion, the threshold is lowered to the degree that reduction is possible by living cells thus providing a low energy entrance of sulphur into the sulphur cycle (Nielson, 1979).

Figure 3.5 shows the  $\delta^{34}\text{S}$  of geologically significant materials.

According to Nielson (1979), when the temperature, solubility and energy requirements are attained, sulphur in the form of sulphate or sulphide, can accumulate in environments with considerably lower background concentrations of sulphur. These concentrations, as a whole can withstand the geological processes that threaten sulphur stability for geologic time, preserving their natural or original sulphur attributes i.e. isotopic signature of formation.

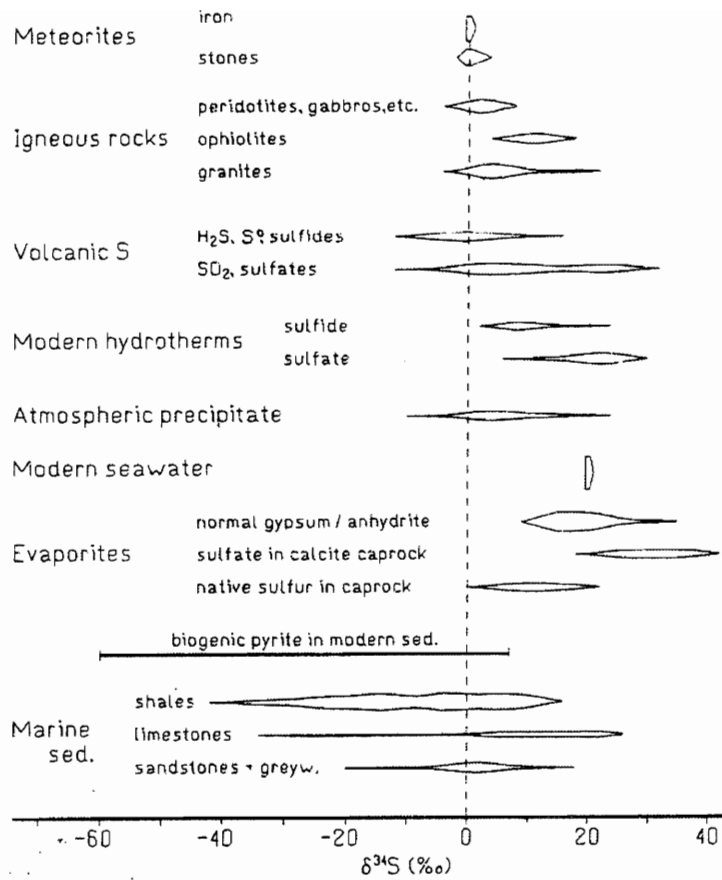


**Figure 3.5:  $\delta^{34}\text{S}$  values for some natural materials**

Distribution patterns of  $\delta^{34}\text{S}$  of some natural material, including most basic lithologies. Modified from Nielson (1979).



### 3.3.3 Sulphur Fractionation

Sulphur isotopes can be fractionated by kinetic fractionation and equilibrium fractionation. Generally, sulphur fractionation studies deal with  $\delta^{32}\text{S}$  and  $\delta^{34}\text{S}$ , the two most abundant sulphur isotopes. Systems that exhibit isotope exchange in equilibrium fractionation are:

1. Sulphide and sulphate in magmatic environments and in hydrothermal fluids at temperatures above 250°C
2.  $\text{H}_2\text{S}$  and  $\text{SO}_2$  in volcanic vents
3. Dissolved sulphide and precipitating sulphide minerals in hydrothermal fluids

Kinetic fractionation, on the other hand, occurs where a unidirectional reaction directly affects a sulphur bond. As a general rule, this process is accelerated with the lighter  $\delta^{32}\text{S}$  isotope. According to Nielson (1979), the most interesting mechanism of this sort is fractionation via bacterial sulphate reduction, which occurs in two distinct ways. The first, *assimilatory* sulphate reduction, is used in biosynthesis, which is when S is used for synthesis of specific organic molecules, such as proteins. This process is limited by the rate at which sulphate complex can be used. The energy level of the sulphate complex and S ion is roughly equal thus little fractionation occurs (<5‰) (Nielson, 1979).

The second form of bacterial sulphate reduction is *dissimilatory* or respiratory. This process is carried out by anaerobic bacteria, which rely on  $\text{SO}_4^-$  as a source of oxygen for metabolism (Nielson, 1979). The reaction whereby oxygen is derived from sulphate is:

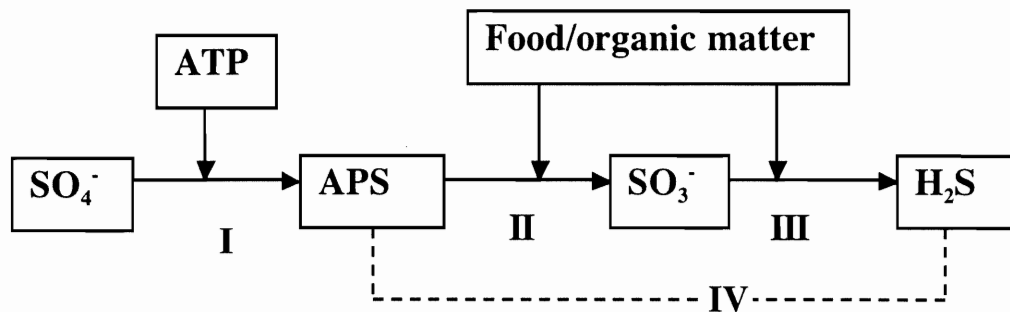


**Figure 3.6: Possible sulphur pathway**

Pathway of S from sulphate, being used by dissimilatory bacteria in metabolism (ATP, APS), through to H<sub>2</sub>S, which is then reduced to pyrite. Modified from Nielson, (1979). ATP = adenosine triphosphate; APS = adenosine-5'-phosphosulphate; Step I is the rate controlling reaction when sulphate or food is in small; Step II, the breaking of the S-O bond is the normal rate controlling step because it is the most energy intensive step, thus the slowest.

### 3.3.4 Distribution of $\delta^{34}\text{S}$ in varying lithologies

As a result of the different sulphur fractionation processes, different lithologies have different isotopic ratios. Through analysis of different lithologies a comparison can be made (Table 3.2).

**Table 3.2: Mean  $\delta^{34}\text{S}$  ‰ for some lithologies**

Material	Mean $\delta^{34}\text{S}$ ‰	Comments
Iron meteorites	~0‰	Only reliable in uncontaminated samples
Mafic igneous* (e.g. mantle provenance)	+1.0‰	Can be contaminated by sediments consumed during emplacement
Felsic igneous*	+2.0‰	Can be contaminated by sediments consumed during emplacement
Modern ocean water (sulphate)	+20‰	
For sediments refer to Fig.3.6		

\*wide ranges can be expected when magma intrudes sediment

In sedimentary rocks there are many processes that can facilitate the fractionation of  $\delta^{34}\text{S}$ . The two most effective or widespread processes include the precipitation of gypsum (anhydrite) from evaporating seawater, and bacterial reduction of pore water sulphate under “closed system” conditions. At deep levels below the sediment interface, the latter is most effective, with minor contributions from bacterial reduction at or just below the water-sediment interface, in transition between shallow and deep (>6cm below sediment-water interface) zones (Nielson, 1979). The end product of sulfate reduction is  $\text{H}_2\text{S}$ , which is poisonous to the bacteria creating it if permitted to accumulate within the system (Figure 3.6). A balance between accumulation and dissipation, therefore, is essential and may be reached when  $\text{H}_2\text{S}$  combines with active iron, derived from detrital minerals to form pyrite (Figure 3.2 and 3.6).

Nielson (1979) notes that when considering an absolute method to discriminate between  $\delta^{34}\text{S}$  of different provenance e.g. hydrothermal or sedimentary, it is not accurate to use divergence from 0‰, as many factors can influence the isotopic signature of sulphur. For example a magma that intrudes black shale will inherit the sedimentary  $\delta^{34}\text{S}$  signature, thereby skewing the igneous signature. Sediments that undergo several phases of fluid circulation may fractionate particular  $\delta^{34}\text{S}$  isotopes preferentially, also resulting in a skewed signature. Thus large spreads in  $\delta^{34}\text{S}$  may not be accurate, and an alternate means must be used to determine the ultimate source of  $\delta^{34}\text{S}$ . A more reliable method is to compare grains within one sample, and if there

exists a strong difference in  $\delta^{34}\text{S}$  between individual grains, then there is a strong likelihood of biogenic fractionation. Local differences in  $\delta^{34}\text{S}$  represent disequilibrium and are unstable, and have a greater tendency to homogenize i.e. recrystallize or be replaced (Nielson, 1979); thus later higher temperature events can wipe out the  $\delta^{34}\text{S}$  signature. In addition, if pyrite is broken down ( $\text{FeS}_2 \rightarrow \text{Fe} + \text{S}^0$ ), the local isotopic ratio may change upon S being reincorporated into a stable phase (Nielson, 1979). However, at El Soldado evidence for pyrite breakdown via the above reaction is absent. Rather, Cu sulphides have replaced pyrite by the addition of Cu (Eqs. 3.4, 3.5 & 3.6).



Pyrite + copper  $\rightarrow$  chalcopyrite



Pyrite + copper  $\rightarrow$  bornite +  $\text{Fe}^{2+}$



Iron + oxygen  $\rightarrow$  hematite

When Fe is removed, S and its isotopic signature are still preserved. In this study it was not possible to analyse individual grains, only whole samples were analysed thus  $\delta^{34}\text{S}$  values represent the mean for the sample, and must be interpreted with this in mind.

### 3.3.5 Previous S Stable Isotope Data

Previous S isotope data for chalcopyrite and bornite were presented by Klohn et al. (1990) where a mean  $\delta^{34}\text{S}$  value close to 0 ‰ was interpreted to indicate a magmatic source. These authors interpreted the observed range in  $\delta^{34}\text{S}$  values as due to variations in temperature and  $f_{\text{O}_2}$ . Framboidal pyrite with  $\delta^{34}\text{S}$  values of 7.3 ‰ and 28 ‰ were interpreted to have formed early by biogenic reduction of seawater S (Klohn et al., 1990). Wilson (1998) observed  $\delta^{34}\text{S}$  from -13 ‰ to +29 ‰, attributing the divergence from 0 ‰ to bacterial fractionation. These authors, however, failed to see any relation between the diagenetic pyrite and the Cu mineralization.

## **CHAPTER 4: RESULTS FOR PETROLOGY, MICROPROBE ANALYSIS, AND $\delta^{34}\text{S}$**

### **ISOTOPIC ANALYSIS**

#### **4.1 Introduction**

This chapter has two main components, a petrographic results section, followed by geochemical results. As previously mentioned, samples have been collected from two distinct regions within the deposit. Samples come from either an ore zone, having a range of sulphides, or from deep pyrite zones, which are pyrite dominated. For convenience, this section contains only descriptions of a few representative samples from the two sample areas. All other sample descriptions are located in Appendix A.

The second component, dealing with the geochemical analysis, presents data derived from the microprobe and sulphur isotope analysis. Following each section, a brief summary deals with all samples.

#### **4.2. Petrographic Descriptions**

##### **4.2.1 Ore zone**

The samples that were used in this study primarily come from the Valdivia Sur ore block (Fig 2.4), which is situated in the deeper zone of the El Soldado deposit. The samples that are most representative of this zone are PC-01, and PC-02A, and PC-04. Each sample is dominated by one either of the three sulphide phases (pyrite, chalcopyrite or bornite)

##### **Sample PC-01**

This sample has been included as a detailed description because it has the highest occurrence of bornite thus a good description of bornite is possible.

### **Hand sample:**

This sample is from a bornite-pyrite vein within the Valdivia Sur orebody. Grey, mildly brecciated, altered calc-alkaline basalts host the 2 cm wide vein, which is cut by late calcite veinlets. Mineralogically, the vein comprises 65% bornite, 20-25% pyrite and 5-10% chalcopyrite.

### **Petrographic Description**

Bornite is the most abundant sulphide in this sample, and occurs predominantly as massive, featureless zones. In some zones, where framboidal pyrite is present, bornite is present, pseudomorphing the framboidal structures. Varying degrees of preservation of framboidal structures persist throughout the sample (Figure 4.1). Internal framboid textures are rarely, if ever preserved during bornite replacement. In this sample, considering only the sulphide phases, bornite represents a sort of “matrix”, and the other sulphide phases are suspended in it. Pyrite is present as large (2-5mm) highly fractured grains that are replaced by chalcopyrite and bornite. As a result of partial replacement, pyrite is observed as small, rounded discrete grains within bornite (Figure 4.2).

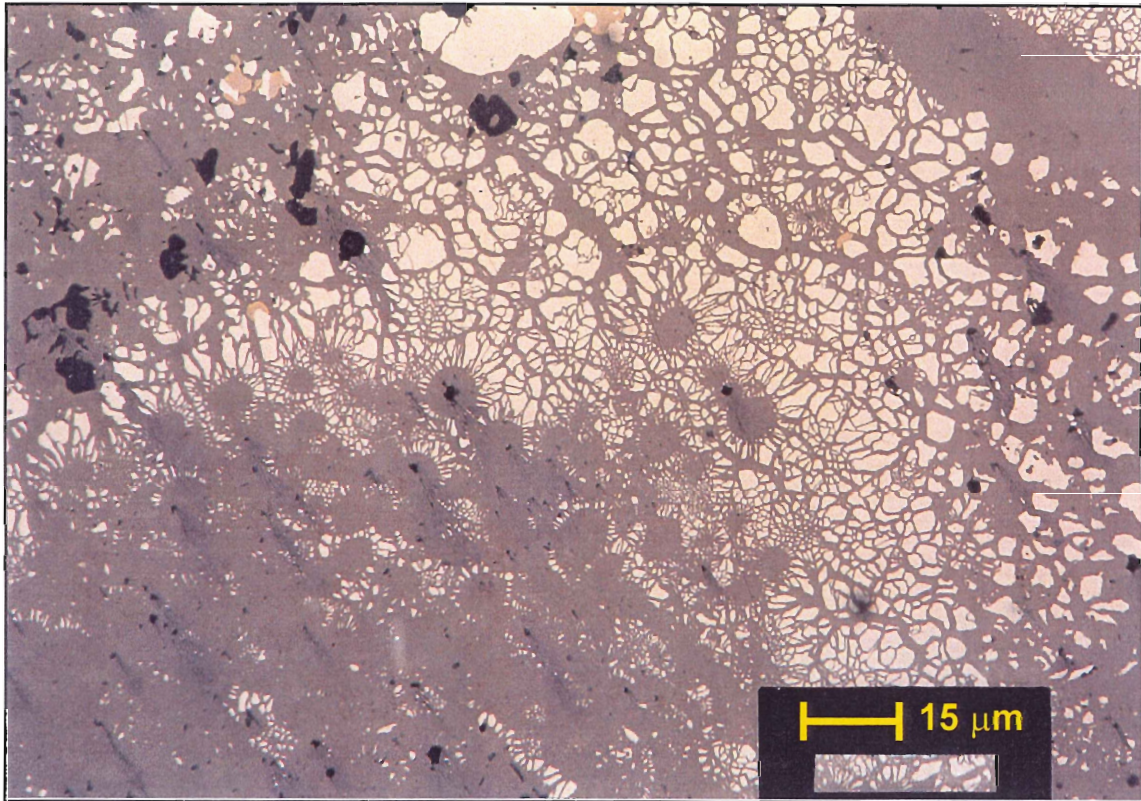


**Figure 4.1: Bornite replacing framboids**

Bornite (pink) replacing framboidal pyrite (white) in PC-01. The replacement front has moved approximately from the bottom left corner to the centre, where more stable, recrystallized non-framboidal pyrite remains less replaced, creating atoll structures as a result. Black streaks are a polishing affect, and black spots are gangue.



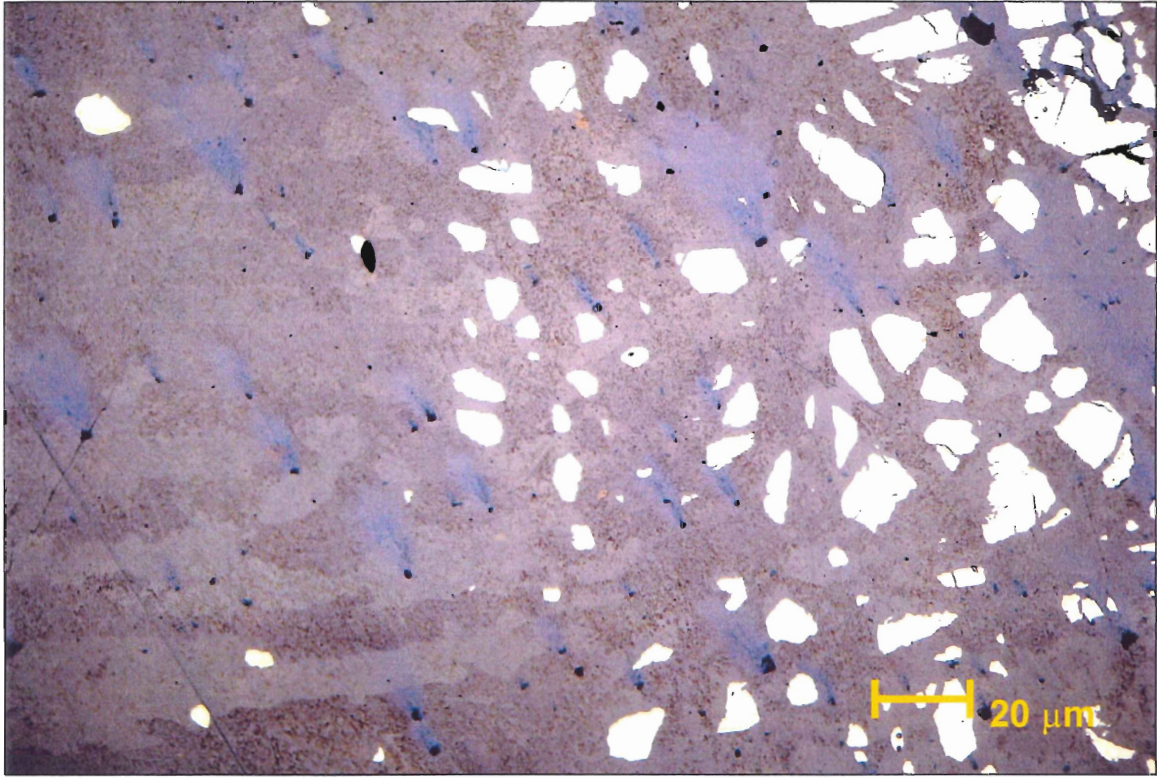


**Figure 4.2: Bornite replacement – remnant pyrite grains**

Micrograph of sample PC-01, taken in reflected light. Pyrite grains are suspended in a matrix of bornite. Pyrite grains are on the verge of being replaced by bornite. This image shows partially oxidized bornite. Note that this alteration has enhanced chemical variation, highlighting a compositionally different lower left corner. This texture is remarkably similar to microprobe chemical composition images of pyrite. Perhaps some degree of chemical variation from pyrite has been preserved, despite replacement. This is discussed in Chapter 5.

Note that black “comet-like” zones are formed during polishing, and tarnish. Composition of black material is unknown (may be quartz).

Replacement of pyrite by chalcopyrite and bornite appears to be controlled by pyrite cleavage, as many of the replacement veinlets are in a regular, approximately orthogonal pattern. Pyrite framboids of similar size and spatial distribution are observed at the periphery of large pyrite grains near the edge of the vein (Figure 4.3 a and b).

Chalcopyrite occurs primarily as veinlets replacing pyrite grains. At the intersection of two chalcopyrite veinlets there are large concentrations chalcopyrite. Locally accumulations of intersection chalcopyrite propagate outwards into adjacent pyrite grains. In some instances, bornite replaces chalcopyrite in the same manner that chalcopyrite replaces pyrite – as small veins penetrating into chalcopyrite. Based on the cross-cutting relationships that are pervasive throughout the slide the paragenetic sequence of sulphide development is interpreted to have begun with pyrite growth, followed by its replacement by chalcopyrite and subsequently by bornite.

### **Sample PC-02A**

This sample is from a massive pyrite-chalcopyrite vein in the Valdivia Sur orebody, situated in the northern part of the deposit. The sample is hosted by slightly altered and mildly brecciated grey basalt of the Lo Prado Formation. PC-02A is rich in pyrite relative to other sulphides, and contains a high frequency of framboids.

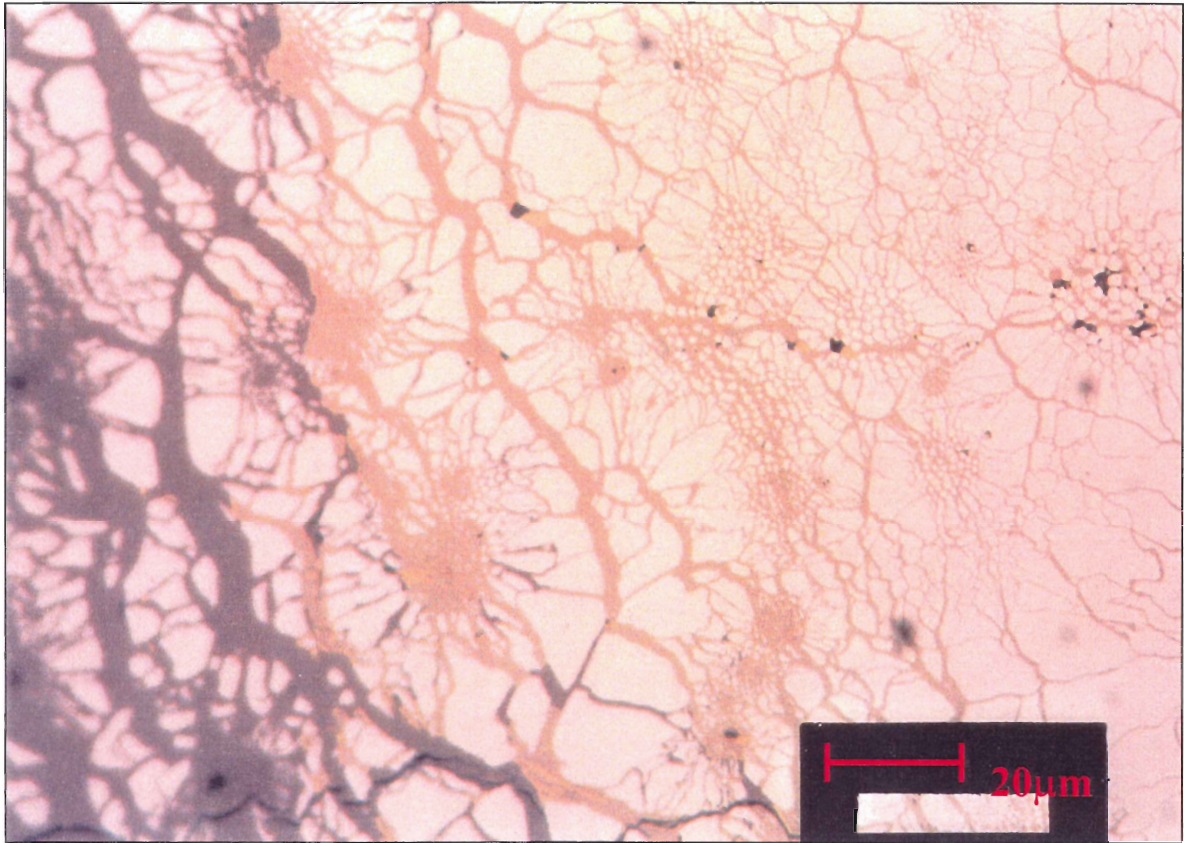


**Figure 4.3a: Progressive framboid replacement**

Reflected light micrograph of PC-01 illustrating replacement of pyrite framboids from left to right by chalcopyrite first (golden yellow), revealing details of interstitial framboid structure. Bornite (pink), replacing chalcopyrite.

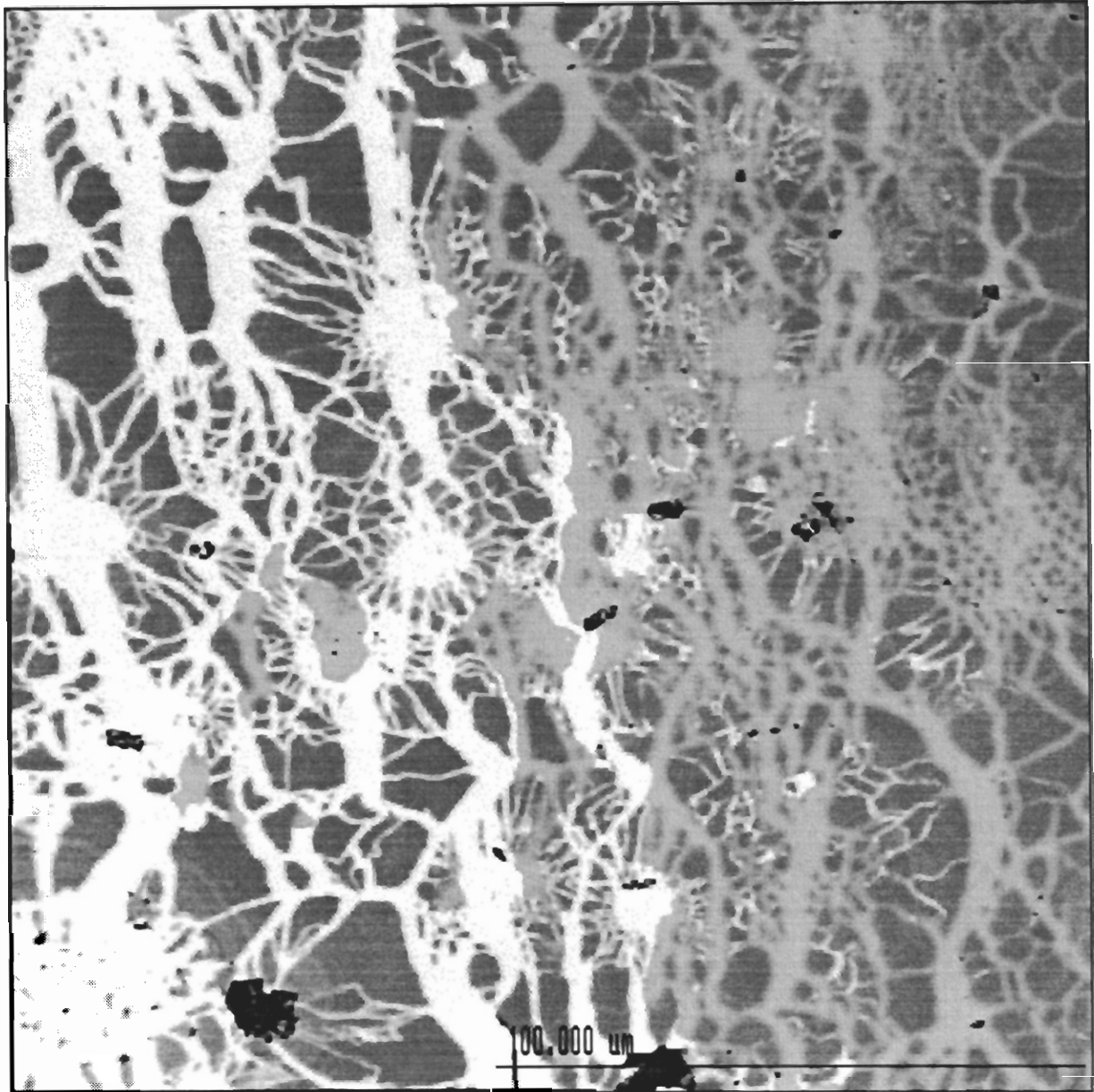


**Figure 4.3b: BSE microprobe image of framboid replacement**

Electron microprobe image of replacement in PC-01. Bornite is white, chalcopyrite is light grey, and pyrite is dark grey. Individual framboid microcrysts are visible at the right, but replacement by bornite has partially destroyed framboid morphology (left side). The partial replacement is called atoll structures (e.g. Ramdohr, 1980).

**Hand sample:**

PC-02A is a massive, 12-15 cm diameter pyrite-chalcopyrite vein (Figure 4.4). It is cut by late calcite veinlets in a web pattern. Pyrite and chalcopyrite occur as small (1-2mm) agglomerated spheroids, suspended in either late calcite, or within the wallrock. The wallrock of the sample is altered or cut by late calcite veins that appear to be tension/extension related. Mineralogically, the sulphides in the vein comprises 97 % pyrite, 1-2 % chalcopyrite and <1 % bornite.

**Petrographic Description**

Pyrite occurs in several distinct morphologies; two forms appear to be spatially controlled. Pyrite occurs most frequently as ca. 100-500 $\mu$ m sub-angular grains that are homogeneous, with cross-cutting, or replacement by veins of chalcopyrite. The coarse grains are found predominantly in the center of the vein. Pyrite also occurs as euhedral cubes or pyritohedra (<2 $\mu$ m - 10 $\mu$ m, average 4 $\mu$ m) suspended mainly in late calcite. The sub-angular pyrite is commonly associated with highly brecciated zones, which appear to result from forceful injection of chalcopyrite veins (Figure 4.5). There is increasing textural heterogeneity within the grains towards the edge of the vein (Figure 4.6).

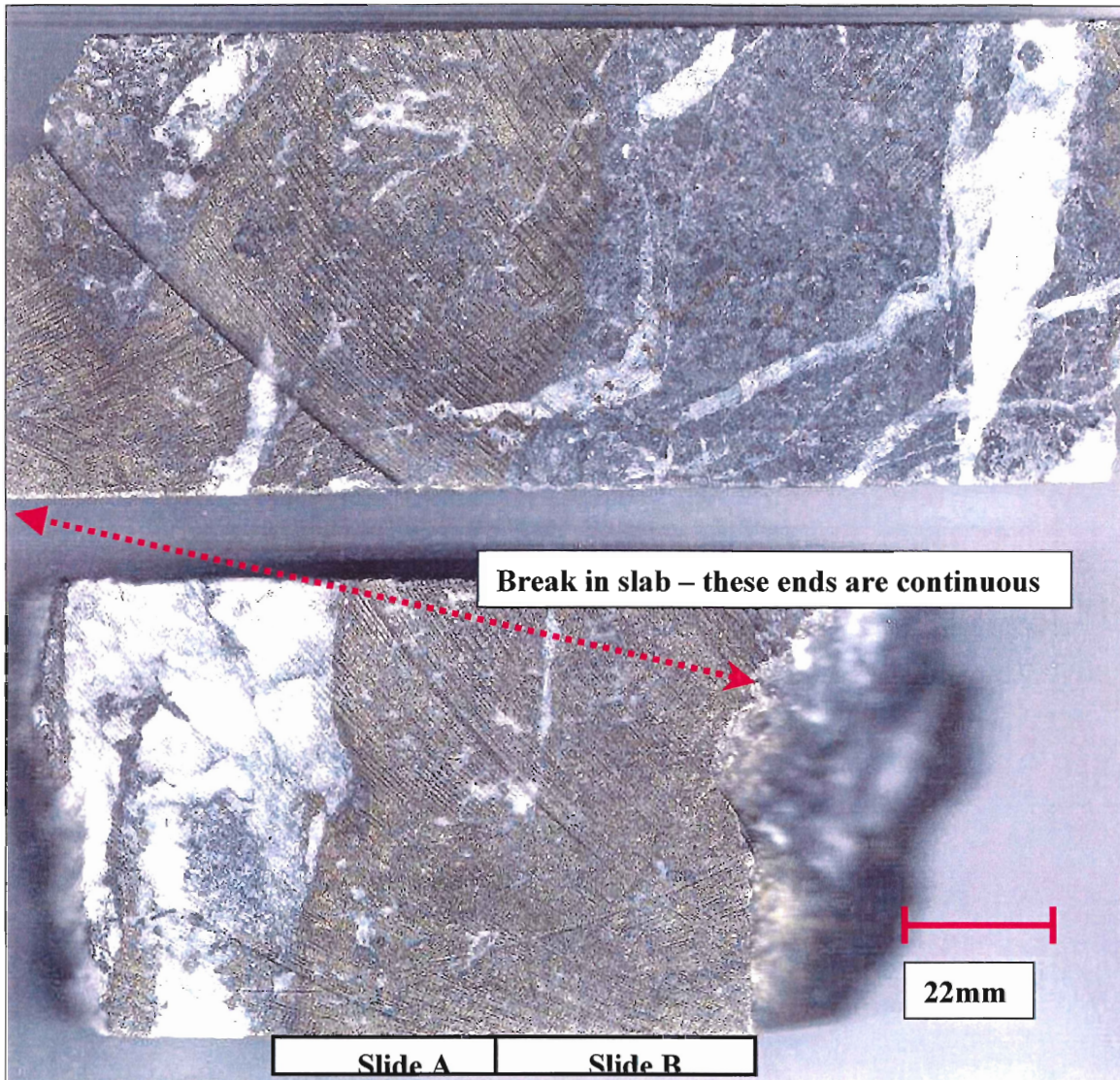


**Figure 4.4: Cut slab sample of PC-02**

Slab of rock that PC-02 A & B were cut from. Late calcite appears to be related to extension, which is consistent with tectonic models of the district. Note that A and B were cut perpendicular to the face up surface. Abundant spheroidal structures are visible at a hand sample scale.

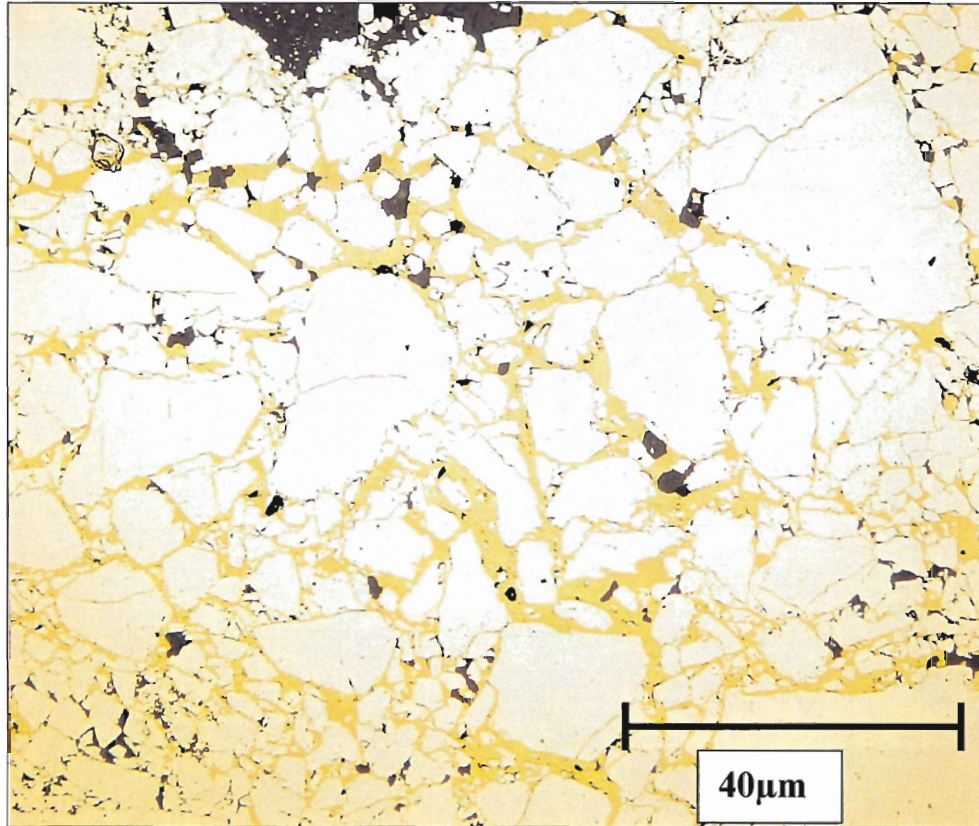


**Figure 4.5: Brecciated pyrite with chalcopyrite infilling**

Reflected light micrograph of PC-02A illustrating the forceful injection of chalcopyrite into pyrite, creating angular fragments of pyrite. Calcite in the vicinity of this image hosts cubic pyrite, which appears to be late relative to Cu mineralization.

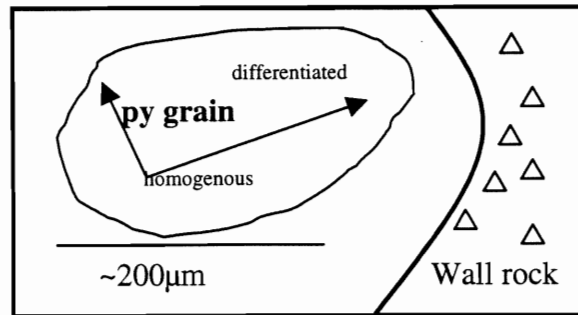


**Figure 4.6: Cartoon of morphology of large pyrite grains**

Textural differentiation in large pyrite (py) veins varies according to proximity to edge of grain

The texture of pyrite in this sample is pyrite framboids. Framboids are present the edge of large pyrite grains, where the grains are in contact with late calcite. The highest abundance of framboids is on grains in close proximity to the wallrock. Pyrite becomes more homogenous towards the core of the large grains (Figure 4.8). Framboids are most abundant in this sample thus a detailed description is pertinent.

Framboids in PC-02A occur in several morphologies. Often a rim of calcite surrounds the framboids when they are at the edge of a pyrite grain. From the center of a massive pyrite grain to the edge there is an increasing resolution of the form of framboids (Figure 4.8). Presence of framboids within the massive pyrite grains can be inferred from textures whereby small concave “inclusions” appear to represent the junction between an aggregate of framboids (Figure 4.7).



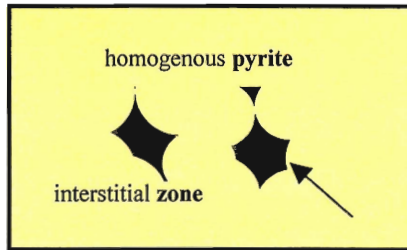


**Figure 4.7: Cartoon of interstitial zones in massive pyrite**

Inferred framboids within homogenous pyrite. Scale of interstitial zone ranges as in Figure 4.8a

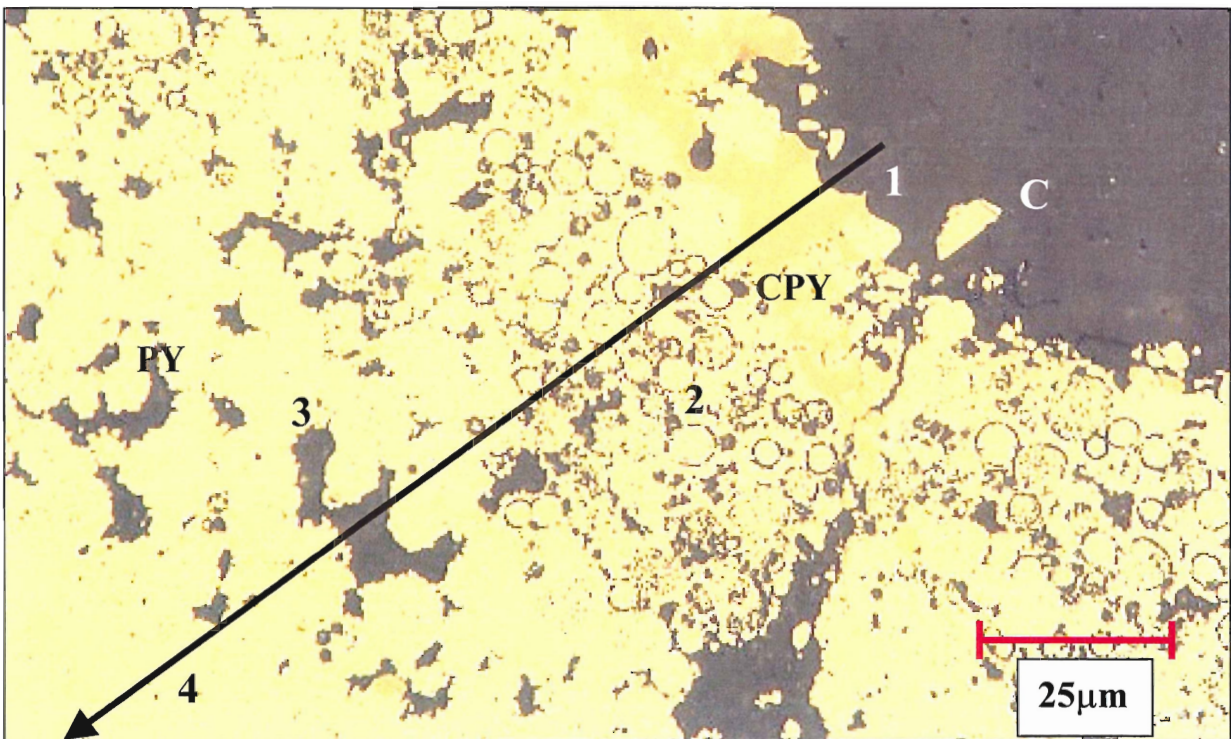


**Figure 4.8a: Heterogeneity in framboidal zones**

Reflected light micrograph of framboidal pyrite at the edge of PC-02A. The right side of the image is the edge of the vein (see Figure 4.4). Point 1 is late calcite (C) replacing the framboids, revealing subtle textural variations. CPY is chalcopyrite. Point 2 is a zone of discrete framboids that are revealed through calcite replacement. Point 3 is a zone of framboids that have not been as completely replaced by calcite, due to their further distance from the calcite penetration into the pyrite (PY). Point 4 is more massive or recrystallized pyrite where framboidal textures are not visible without microprobe imaging (Figure 4.8 b).

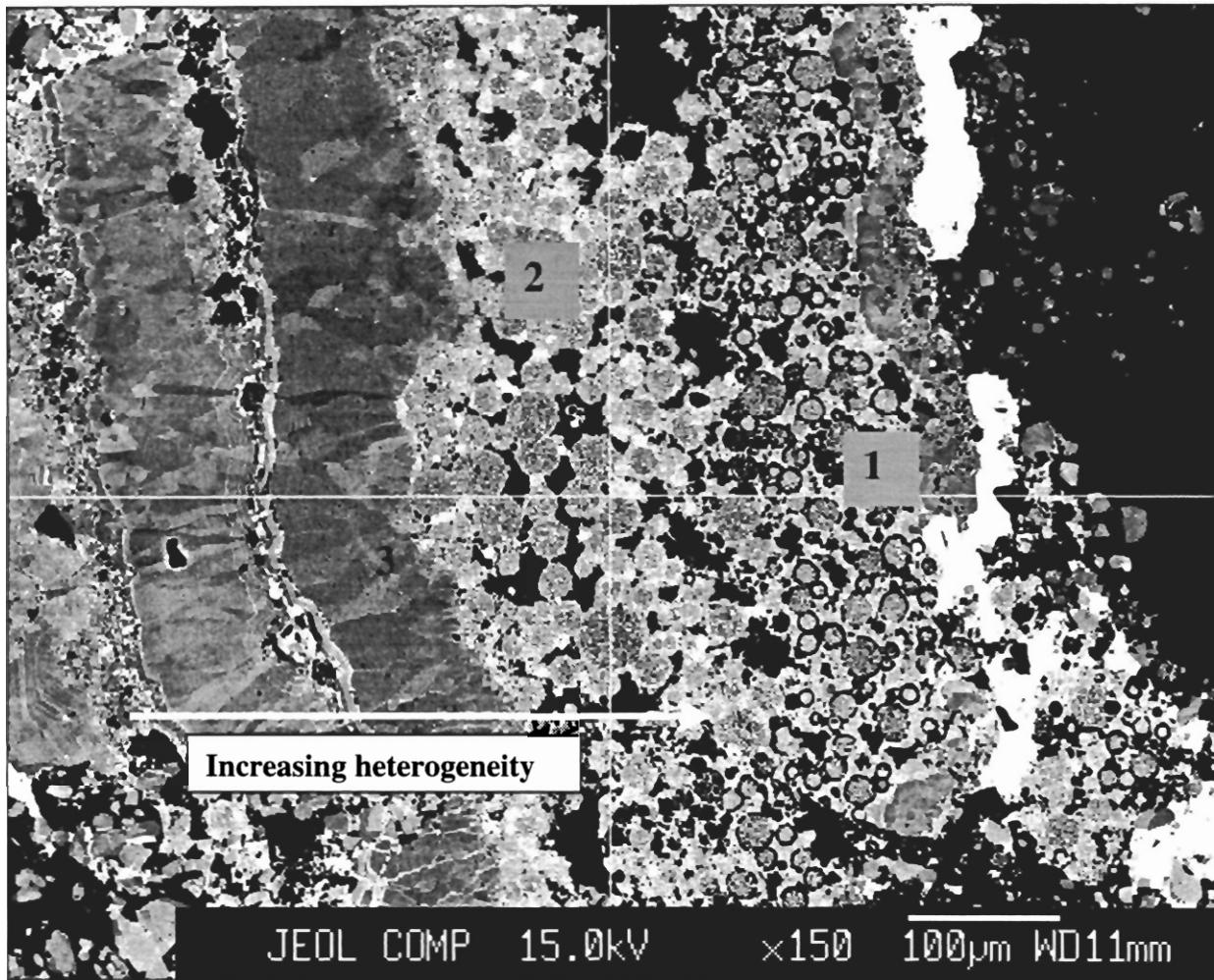


**Figure 4.8b: Microprobe image of framboid zone composition**

Composition-variation electron micrograph of PC-02A. Black is calcite. From right to left from the peripheral calcite, discrete framboids are present (1). Zone 2 shows the same spheroids as in Zone 3 in 4.7 a, but now reveals discrete internal microstructures characteristic of framboids. Point 3 identifies a texturally distinct zone compared to the framboids. The anisotropic nature is only visible as chemical variation, and is not optically detectable.

The microcrysts, or individual framboid components that comprise framboids occur in three forms: spheroidal, euhedral and annealed or recrystallized, where distinct form of microcrysts are not discernable. Microcrysts range in diameter from 0.25 $\mu\text{m}$  to 0.1 $\mu\text{m}$ . The framboids' packing arrangement varies from tightly to loosely packed microcrysts. Calcite or chalcopyrite occupies interstitial space between microcrysts. The tightest packed framboids permit no replacement and are essentially annealed or recrystallized, with a homogenous core. More loosely packed spheroids permit replacement by calcite or chalcopyrite. Microprobe compositional analysis has permitted the detection of framboidal pyrite in optically homogenous pyrite (Figure 4.8b, 5.2a and 5.2b).

Chalcopyrite is the second most frequently occurring sulphide in PC-02A. Chalcopyrite occurs predominantly as small (5 $\mu\text{m}$  to <1 $\mu\text{m}$ ) veinlets that cross-cut pyrite mainly in a cleavage controlled pattern (orthogonal vein sets), and also as forceful injections that resulted in pyrite breccia. The occurrence of chalcopyrite is locally more abundant near pyrite framboids. Framboids are often partially pseudomorphed by chalcopyrite; thus where framboids are concentrated there is a higher modal occurrence of chalcopyrite.

## **Sample PC-04**

This sample has been included as a detailed description because it has the highest percentage of chalcopyrite thus a description of textures that it exhibits is possible.

### **Hand sample**

This sample, from Valdivia Sur, is a vein of massive chalcopyrite hosted by altered grey basalt of the Lo Prado formation (Figure 4.9). Late calcite veinlets cross-cut the massive chalcopyrite vein. Framboids are visible without magnification in the hand sample. Mineralogically, the vein comprises 85% chalcopyrite, ca. 14% pyrite and ca. 1% bornite.

### **Petrographic Description:**

Chalcopyrite is the dominant sulphide in this sample, and exhibits primarily a massive and homogenous texture. Textural heterogeneity occurs mainly proximal to pyrite grains, where pyrite framboids are replaced. Chalcopyrite replaces pyrite grains mainly as veinlets that cut and penetrate pyrite. This gives chalcopyrite a finger-like texture at grain the periphery. Pyrite is also absorbed in a homogenous manner, leaving smooth edges on pyrite grains. The most distinct replacement texture chalcopyrite exhibits is where it is replacing pyrite framboids. Chalcopyrite appears to have preference to the interstitial zones of the framboid relative to the more homogenous rims that most framboids have (Figure 4.10). This preferential replacement is extensive throughout framboidal zones, both in this sample and others. This type of replacement texture,

known as atoll replacement is common in this sample, and is present in other samples where there is a high proportion of copper sulphides (Figure 4.11a, b, c).

Pyrite occurs much as in PC-01, as large coarse sub-rounded to elliptical grains that are being replaced by chalcopyrite. The grains are zoned according to the degree of replacement from edge to core. At the rim of most pyrite grains, penetration of chalcopyrite into the grain results in many small (<20 $\mu$ m), discrete pyrite grains within chalcopyrite. From the edge moving into the grain itself, chalcopyrite replacement lessens, becoming only thin veinlets, and finally homogenous pyrite. These veinlets typically form in sub-circular patterns. It is possible to discern between framboidal and massive pyrite at the edge of a grain based on the relative heterogeneity – framboids create increased heterogeneity.

Bornite occurs infrequently as small irregularly shaped blebs with sub-angular edges and is only found in contact with chalcopyrite; distribution of bornite appears to be random.

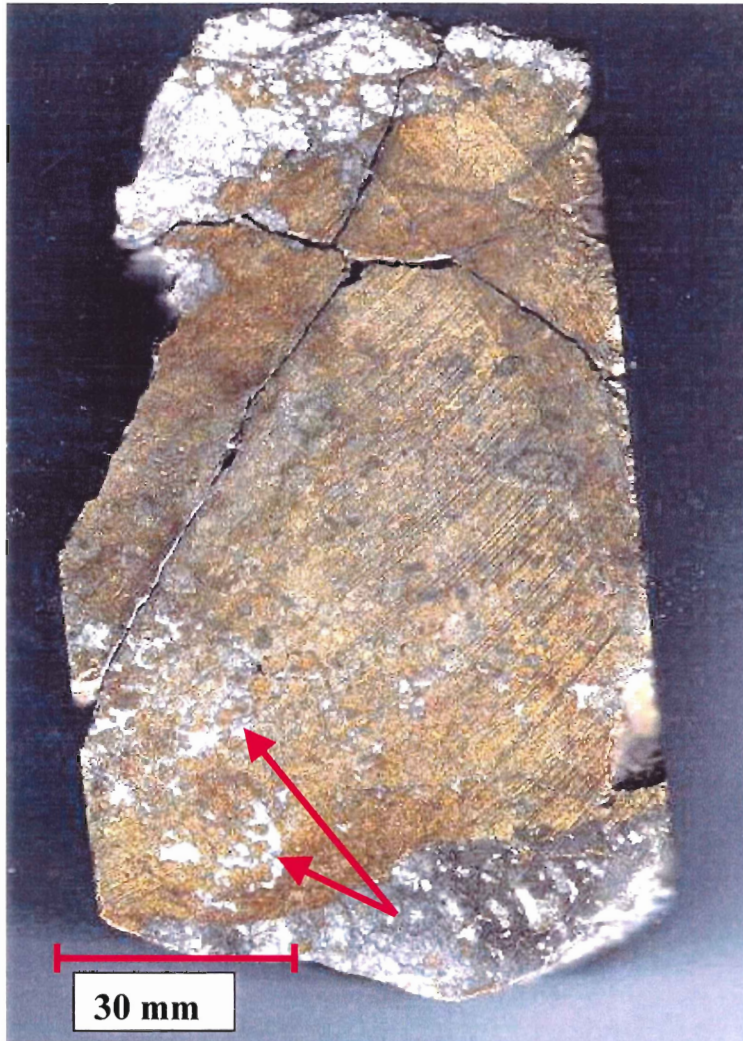


**Figure 4.9: Cut slab sample of PC-04**

The sample is primarily chalcopyrite and pyrite is difficult to discern in this photograph. Red arrows point to zones where spherical structures are visible. These are pyrite grains suspended in calcite and chalcopyrite. The periphery of these grains is where framboids are most visible under magnification.

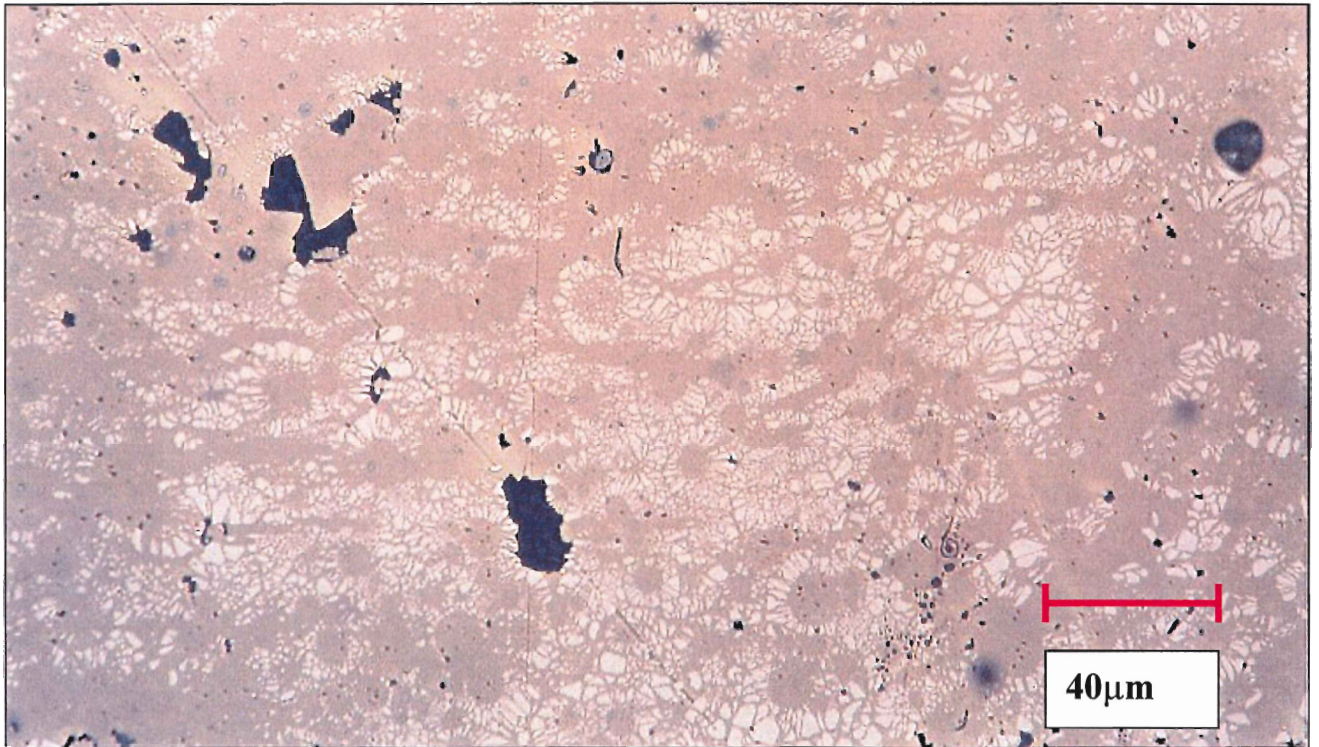


**Figure 4.10: Chalcopyrite replacing framboidal pyrite**

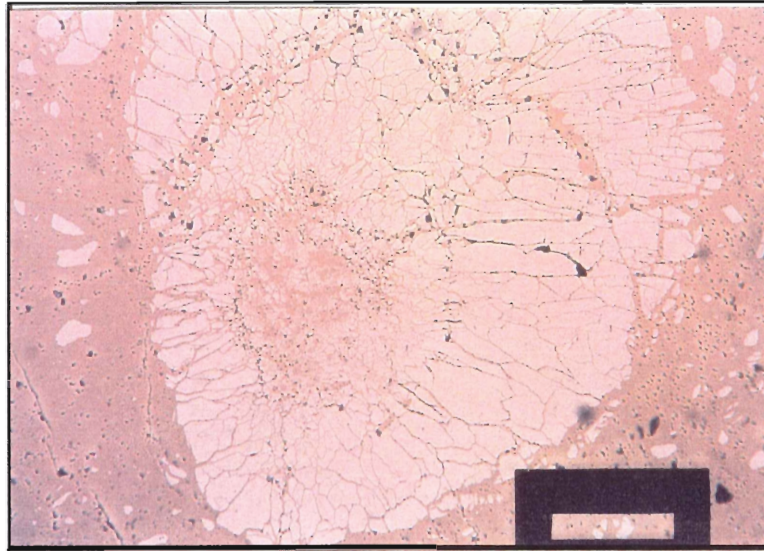
Reflected light image of PC-04. This image illustrates the typical form of chalcopyrite replacement after pyrite framboids. The yellow/gold is chalcopyrite, and white is pyrite. Black spots are holes related to polishing, and not a function of the sample. Framboids are replaced preferential to more texturally uniform pyrite shells surrounding the framboids, creating small atoll structures of chalcopyrite.

**Figure 4.11 a, b & c.**

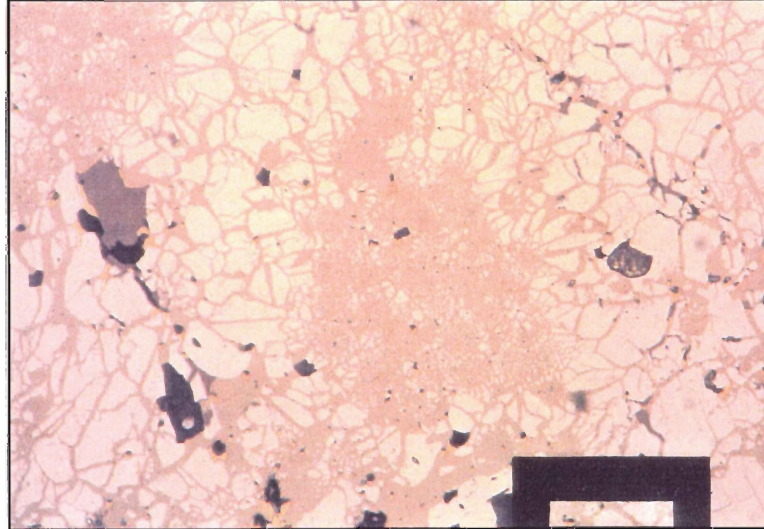
Reflected light micrograph illustrating large atoll structures in PC-04. In all cases golden yellow phase is chalcopyrite, and the white mineral is pyrite. It is postulated that the shells of pyrite that remain are chemically more stable than framboidal pyrite, and resists replacement longer.



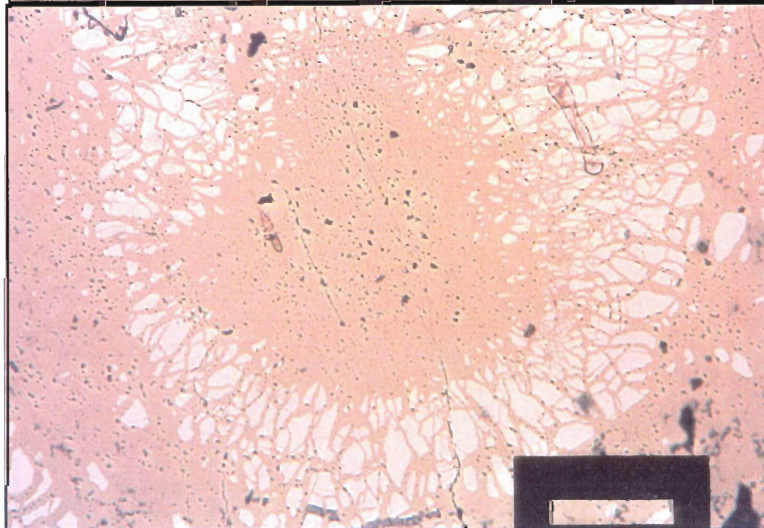
**A.** scale bar  
is 50 $\mu$ m long



**B.** scale bar  
is 35 $\mu$ m



**C.** scale bar  
is 80 $\mu$ m long



#### **4.2.2 Deep Pyrite Zone**

Two samples from the deep pyrite zone were studied to determine the degree of hydrothermal or high temperature pyrite contribution. Due to the lack of Cu sulphides in these samples, which does not exceed 5%, there will be no description of them.

Pyrite samples can be divided in to two broad categories based on texture: those exhibiting colloidal to inclusion rich textures and those with primarily cubic or aggregated cubic pyrite textures.

#### **Sample MP2001-50**

This sample is from the root of the Valdivia Sur orebody cluster, in the southern section of the deposit (Fig 2.1, 2.4). The sulphides in this sample are a 5 to 10mm wide anastomosing vein of pyrite. The vein is located in close proximity to a rhyodacite dike, and there is late calcite interspersed throughout the vein.

Mineralogically, the vein comprises ca. 98% pyrite, <1 %chalcopyrite and <1 % specular hematite.

Pyrite occurs in several different textures throughout the sample. The least commonly occurring mode is euhedral pyrite, which is present primarily at the periphery of the vein, in contact with surrounding calcite (Figure 4.12). The cubes range in size from <1 $\mu$ m to 15 $\mu$ m. The cubes are subidioblastic, rarely having perfectly sharp edges, or corners. Inclusions in this pyrite are rare compared to other samples. In many places the cubes have aggregated into polycubic masses. Where this occurs, the edges of the cubes are sometimes still distinct within the aggregate. It is possible to observe traces of where

cubes have grown together, because the aggregations usually preserve inclusions where the cubes did not fill in e.g. Fig. 4.8.

The second major texture of pyrite in this sample is a colloform texture.

Colloform textures are present throughout the sample as large (up to  $300\mu\text{m} \times 75\mu\text{m}$ ) structures (Figure 4.13, 4.14). Colloform structures are observed as concentric bands of pyrite growing outwards from a central zone. These bands alternate with calcite, which appears to have partially replaced, less stable growth rings, or been present during growth. There is no preferred orientation of the structures within the sample, but as discrete structures they are asymmetric, appearing open at one end and closed at another (Figure 4.13 & 4.14). The number of concentric bands visible is dependent on the degree of calcite replacement. Often in the cores of the colloform structures there are spherical zones, which sometimes appear to be a locus for outward growth (Figure 4.13, 4.14). Using electron microprobe compositional imaging it is possible to observe minute ( $<1\mu\text{m}$ ) spheroids or cubes clustered together and composing the spherical structures (Figure 4.14). Each growth band has a characteristic pattern as it grows. The inner edge is marked by a sharp distinct boundary, often abutting calcite. As it progresses outward it becomes less defined, ending as plate or needle-like laths (Figure 4.15).

Where colloform textures are not directly observable in more massive pyrite zones, there are often distinct patterns of small inclusions that mimic the observable colloform structures, implying that they are simply less replaced by calcite, thus less detectable.

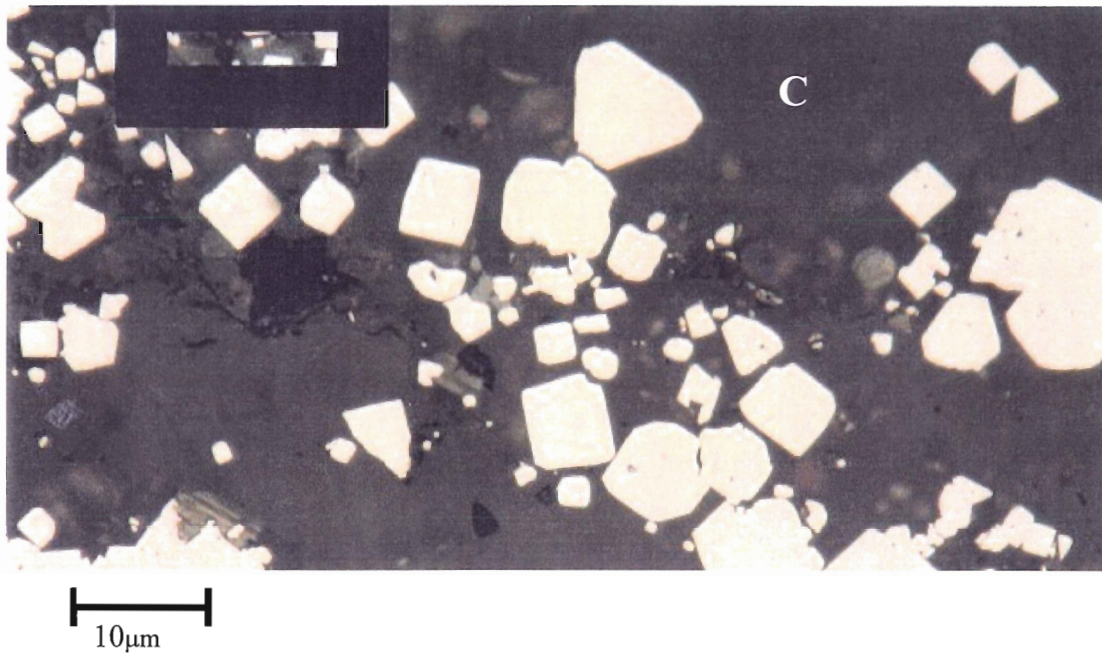


**Figure 4.12: Late idioblastic pyrite cubes and pyritohedron**

Reflected light micrograph from the periphery of MP2001-50. Cubic pyrite is dominant at the edge of the sample, but is not as prevalent in the centre of the vein. Note the idioblastic texture, and lack of inclusions, which makes this form of pyrite distinct from other cubic pyrite in different samples. The matrix in this sample is calcite (C).

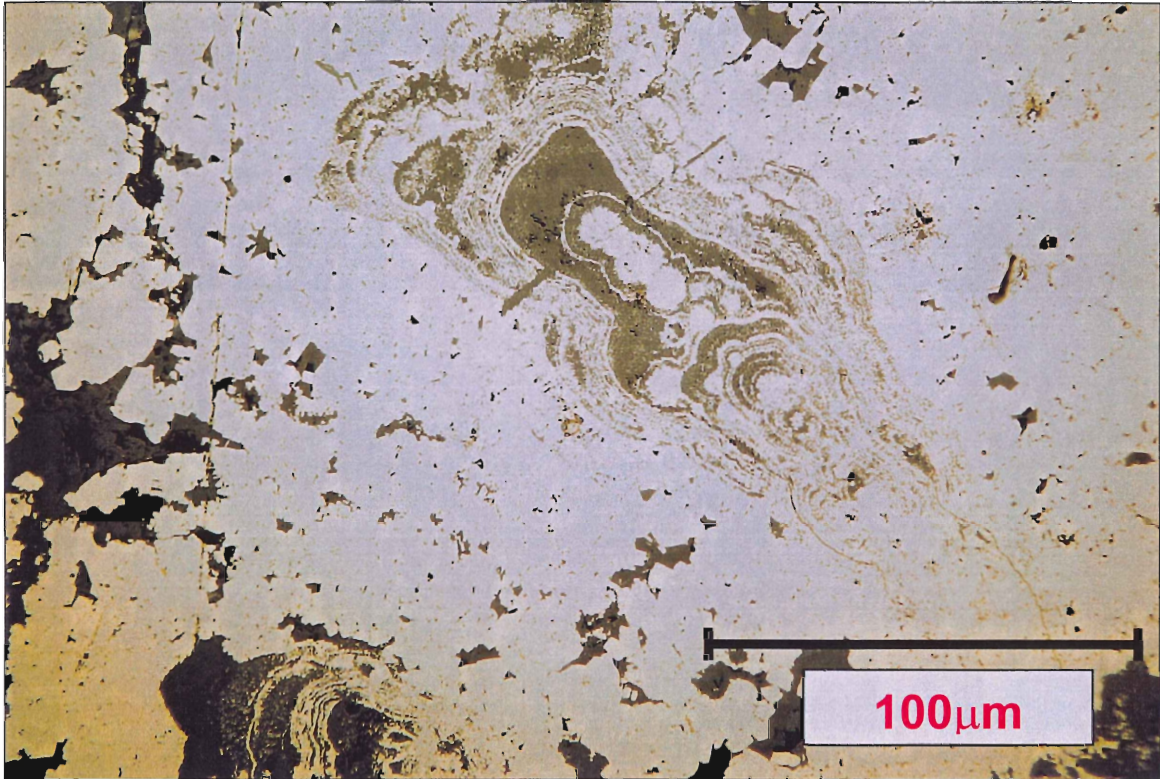


**Figure 4.13: Large colloform structure in pyrite**

Reflected light micrograph of MP2001-50 showing a well-preserved colloform structure. The structure shows multiple growth rings, indicating stable conditions for a long time span. The beginning of each new ring or band is characterized by a needle or plate-like morphology, indicating free space to grow into. This may also be a function of preferential replacement of an acicular or "micro-lath" texture. Pyrite does not have a needle or plate-like crystal form, so it could represent a pyrite precursor (marcasite?) that has later been pseudomorphed by pyrite.

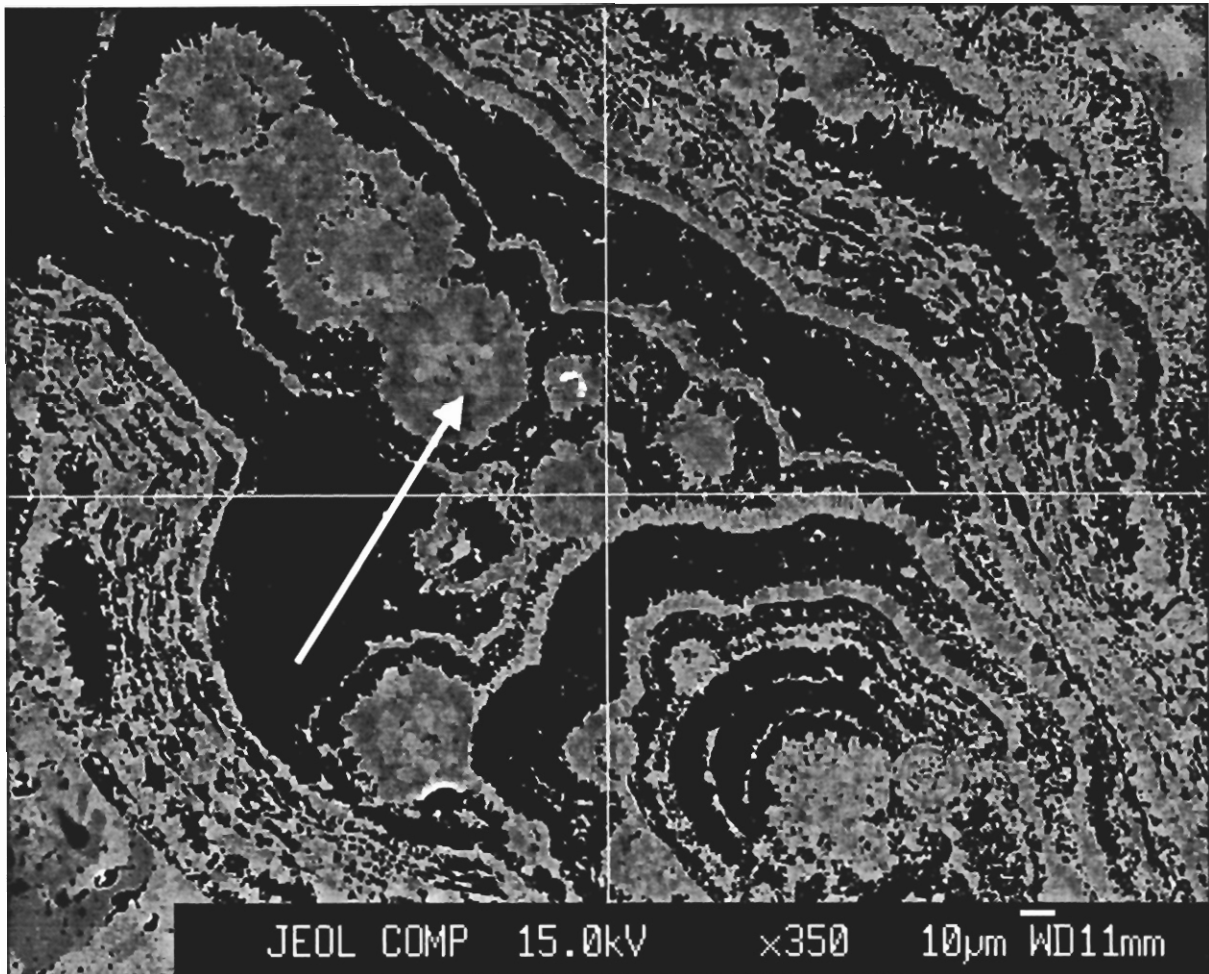


**Figure 4.14: Microprobe image of colloform spheroids**

This figure is a composition-variation microprobe micrograph. The area imaged is the same as in Fig. 5.3a (though a different scale). The important features of this image are the spheroidal clusters in the centre of the image. In the reflected light and in backscatter electron imaging, the discrete zonation in the spheroids is not evident. This compositional variation image shows micron scale cubes and spheres (red arrows). This pattern strongly resembles that of framboidal pyrite in this study as well as that of similar images done by others (see references within Chapter 3 on framboids)

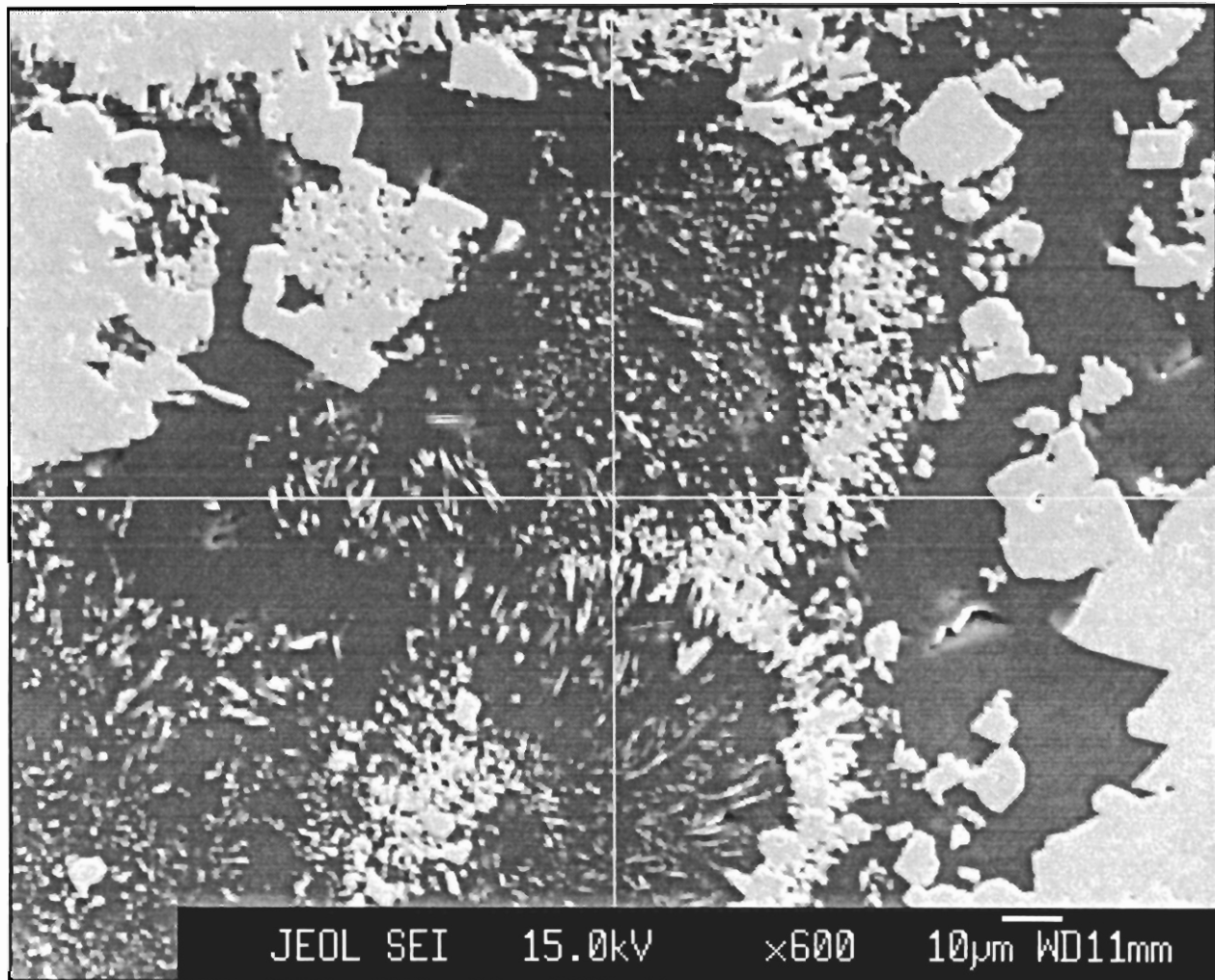


**Figure 4.15: Plate-like pyrite textures**

Secondary electron image (SEI) is from sample MP2001-50, in the Valdivia Sur ore zone. The image shows oriented plates or laths of pyrite. Pyrite does not form this morphology, so this texture must represent pseudomorphing of a previous mineral such as marcasite, a low T polymorph of pyrite. The needles are oriented presumably because of growth patterns, which have now been replaced by calcite (dark grey matrix mineral).

### **Sample MP2001- 74**

This sample is included because it has the most distinct pattern of inclusions, which are observed in many of the other pyrite samples.

This sample comprises 99% pyrite and <1 % specular hematite and chalcopyrite. Pyrite occurs in two different morphologies, both cubic pyrite (Figure 4.16), and as pyrite aggregates, which are more common.

Cubic pyrite ranges in size from <2 $\mu$ m to 30 $\mu$ m and is poikiloblastic, containing inclusions of calcite, other non-sulphides and rare hematite. Inclusion distribution appears to be random throughout the slide. The inclusions have two distinct sizes: large (ca. 8-4 $\mu$ m), and small (<1 $\mu$ m). The different sizes of inclusions also show no zonation: large and small inclusions generally co-exist together. The majority of poikiloblastic pyrite cubes have a fresh, inclusion-free rim of varying thickness. This rim is sharply defined, and appears to be related to a second phase of pyrite growth.

The second morphology of pyrite present in this sample is aggregates of cubic pyrite. The aggregates are also full of inclusions, again of calcite, and rarely as Fe-oxides.



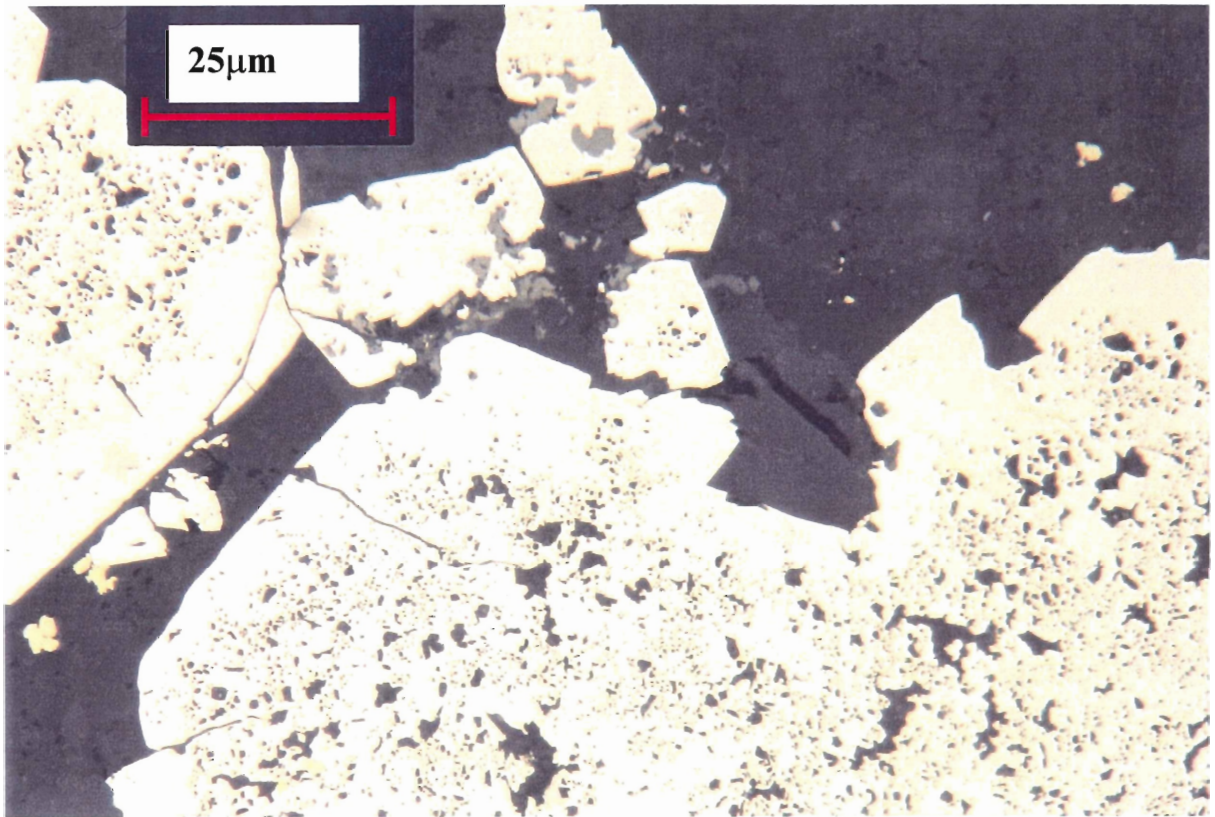


**Figure 4.16 : Poikiloblastic pyrite aggregates**

Reflected light image of MP2001-74 illustrating the poikiloblastic or sieve-like texture of pyrite in. Note the fresh, inclusion-free overgrowth on the rim of the aggregates. This implies multiple phases of growth in this sample. Visible at the top centre of the image is several partially replaced cubes of pyrite. Generally, cubes are more idiomorphic than this in this sample. The shape and size of inclusions similarities between barren and mineralized inclusions indicates that most inclusions now filled with calcite were once filled with hematite, the grey inclusion mineral in center top of image.

### 4.2.3 Petrographic Summary

Samples from the El Soldado deposit have varying morphologies and assemblages. Variation in texture and sulphide assemblage is somewhat spatially controlled. Ore-zone samples e.g. Valdivia Sur, display massive, and often framboidal, pyrite textures. Most of this pyrite has undergone some degree of replacement by Cu sulphides. Framboidal pyrite appears to be replaced preferentially by Cu sulphides relative to more massive or recrystallized pyrite.

Pyrite samples from the deep root zone are texturally and mineralogically distinct from the ore zones. Different processes appear to have formed the majority of these samples relative to the ore zones. Zoning in some samples and not in others indicates multiple phases of growth were not spatially widespread or consistent. Cubic pyrite is often suspended in a calcite matrix, indicating a relative timing – cubic pyrite has formed later than non-cubic pyrite because the calcite from cross-cutting relationships is itself later than much of the mineralization.

It is the opinion of the author that all of the pyrite in the ore zones is low temperature, diagenetic pyrite, having little influence from the high temperature phase of metallogenesis, other than replacement by Cu-rich fluids. Pyrite from the deep pyrite zone has been formed through several different processes, and it is difficult to determine satisfactorily what degree of influence the low temperature diagenetic phase has had on these samples. There appears to have been several phases of growth, indicated by the many growth bands in colloform pyrite, which appears to have grown early, and also by the fresh overgrowth rims on some poikiloblastic pyrite.

## 4.3 Geochemistry

### 4.3.1: Microprobe sulphide analysis

This section provides a summary of geochemistry of the samples, as derived from microprobe analysis. Microprobe analysis was conducted on all 17 samples used in this study. All data, both raw and refined and categorized are located in Appendix II in weight percent. There are few strong chemical trends in the samples. The most notable trend is the presence of relatively high levels of arsenic in some samples, especially those of the Valdivia Sur orebody cluster. All data in section 4.3 are reported in wt. percent.

Bornite does not exhibit significant deviations from normal bornite stoichiometry. There was very little incorporation of other elements into bornite, with the exception of Pb, which ranges from undetected to 1.43%. However, it is possible that Pb values are related to polishing, which used a lead lap and diamond paste (G. Brown, pers. comm.)

Chalcopyrite exhibits considerable variation in Cu:Fe:S proportions, although the significance of this variation is unknown. This phase, when from Valdivia Sur samples, is enriched in As, up to 0.64%, as well as Co, up to 0.25%.

Pyrite exhibits some degree of stoichiometric variability. However, the microprobe used for analysis had a high degree of drift from the standard during analysis, due generally to old age (R. MacKay, pers. comm.). This drift, even when corrections from calibration standards were taken into account, is still abnormally high, resulting in less reliability of accuracy in data. Pyrite exhibits some degree of incorporation of Cu (up to 8.17%), Arsenic (up to 2.78%), nickel, manganese, cobalt, lead, and molybdenum. Again, Pb is possibly due to polishing affects.

Arsenic, when assessed in relation to texture of the host phase, displays some trends (Appendix D, Table D.4). In particular, As is enriched in framboidal pyrite, and in pyrite within zones surrounding framboids. As is enriched in fresh, inclusion-free rims around poikiloblastic pyrite cubes and aggregates of poikiloblastic pyrite grains. In chalcopyrite As is enriched, in particular, adjacent to framboidal zones.

When considering only samples with As enrichment, that is, traces above 0.1% As, a pattern of As distribution is present. 50 % of the points with enrichment are in the direct vicinity of a framboidal zone, 28 % are related to overgrowths on poikiloblastic pyrite cubes or aggregates. The remaining 22% have a more random distribution

#### **4.3.2: Geochemistry of $\delta^{34}\text{S}$ Isotopes**

Thirteen samples were processed and sent to the Stable Isotope Laboratory of Queen's University for  $\delta^{34}\text{S}$  analysis. These samples all have corresponding polished sections, thus a comparison between textures of the ore and the range of  $\delta^{34}\text{S}$  ‰ has been made.

$\delta^{34}\text{S}$  values range from  $-6.6\text{‰}$  to  $+17.1\text{‰}$ , and all samples except 70B, which is chalcopyrite, are pyrite. The mean value of  $\delta^{34}\text{S}$  for pyrite is  $5.8\text{‰}$ . These samples were specifically chosen because they are dominated by pyrite, and it is hoped that they will provide information on the paragenesis of much of the deep pyrite, which many workers e.g. Holmgren (1987) in the past have claimed as hydrothermal.

As stated above, the usefulness or validity of  $\delta^{34}\text{S}$  data is greatest when the values are correlated within a specific zone of individual grains in a sample. In this study, it was not possible because samples were picked for polished section analysis as a priority, and

the remaining portion of the sample was crushed and sulphides concentrated for  $\delta^{34}\text{S}$  analysis. It is possible to compare the overall texture of the samples to the isotopic values to determine if the  $\delta^{34}\text{S}$  is accurate in terms of equilibrium (i.e. if the phases are in equilibrium), and textural homogeneity. Data have been summarized in Figure 4.17 to 4.21, in which data have been correlated according to which orebody cluster samples are from. It is not realistic to assume that in a deposit of such a large scale the chemical environment in which sulphides were deposited in was uniform over time or space. Thus grouping by location and sulphide phase, in combination with Table 4.4, can provide insight into the processes that have created the orebody clusters of the deposit.

Figure 4.17 is a chart with all pyrite samples from the Valdivia Sur orebody cluster.  $\delta^{34}\text{S}$  values range from +6.3‰ to 17.1‰, the highest value recorded from this data set. The average  $\delta^{34}\text{S}$  is 11.6‰. This orebody cluster is in the southern region of the deposit, where most pyrite is framboidal, and where bitumen is more pervasive (although none was noted in this analysis). The textures for these samples are summarized in Table 4.4, and indicate a strong presence of colloform pyrite, which according to Ramdohr (1980), is a product of low temperature genesis.

Figure 4.18 presents data from the Arauco orebody cluster.  $\delta^{34}\text{S}$  values range from 10.5‰ to 16.7‰, and have the highest average value (13.7‰) from the data set. This orebody is in the north-central zone of the deposit, where bitumen is less prevalent. The textures associated with this orebody cluster according to Table 4.4 are predominantly zoned, or multiphase cubic pyrite with some colloform pyrite also present.

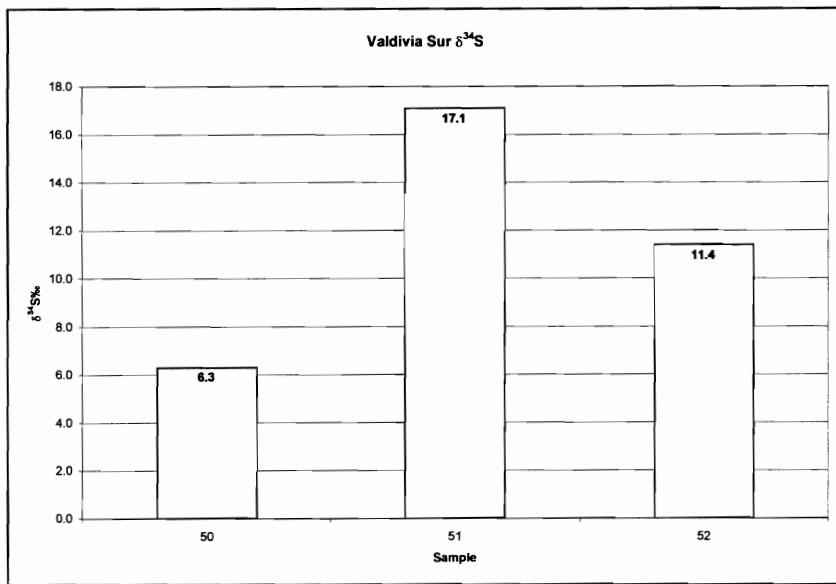
**Table 4.4: Summary of isotopic and textural data**

Sample	$\delta^{34}\text{S}$ ‰	Ore-body	Sulphide	General Texture
50	6.3	Valdivia Sur	pyrite	Colloform pyrite dominant, cubic pyrite (inclusion-free) common at periphery of host vein
51	17.1	Valdivia Sur	pyrite	Massive, brecciated vein of pyrite; cpy and hem (<2%); cubic pyrite uncommon
52	11.4	Valdivia Sur	pyrite	Colloform pyrite; massive pyrite; cubic pyrite at periphery of vein – two apparent generations based on inclusion or inclusion-free
60	16.7	Arauco	pyrite	Subhedral pyrite cubes with few inclusions; colloform structures (rare, but evidence suggests more present but not revealed by replacement); pyrite has embayed texture at edges of agglomerates
61	13.8	Arauco	pyrite	Cubic pyrite (in <50 $\mu\text{m}$ vein); rare colloform structures; skeletal pyrite at periphery of vein; py possible pseudomorphing hematite/marcasite(?)
62	10.5	Arauco	pyrite	95% euhedral pyrite, but with inclusion rich cores in larger cubes
67	-0.2	Arauco Norte	pyrite	Sub-rounded pyrite; cubic py uncommon; brecciated vein; few inclusions, where present not zoned; hematite present
68	7.4	Arauco Norte	pyrite	Cubic pyrite and amorphous pyrite with zonation of inclusions. Fresh overgrowth at rim is inclusion-free
69	-3.3	Arauco Norte	pyrite	Discrete concentrations/blebs of pyrite; very homogenous; inclusions rare, when present smooth/amoeboid shaped – as if fluid was present
70A	-2.9	Arauco Norte	pyrite	Discrete blebs of pyrite – amorphous, homogenous; inclusions are rare, when present are amoeboid shaped, as if fluid/gas once present; pyrite
70B	-6.6	Catedral	CPY	High-grade chalcopyrite vein; very homogenous/massive – no evidence for framboids; inclusions commonly filled with specularite; no pyrite
74	-0.4	Catedral	pyrite	Xenoblastic poikiloblastic pyrite, usually agglomerated into clumps; inclusions are zoned into two distinct size groups; fresh inclusion free overgrowth at rim
76	-7.4	Morro	pyrite	Cubic pyrite and agglomerated cubes. Both have fresh, inclusion-free overgrowth/rim. Multiple growth phases.

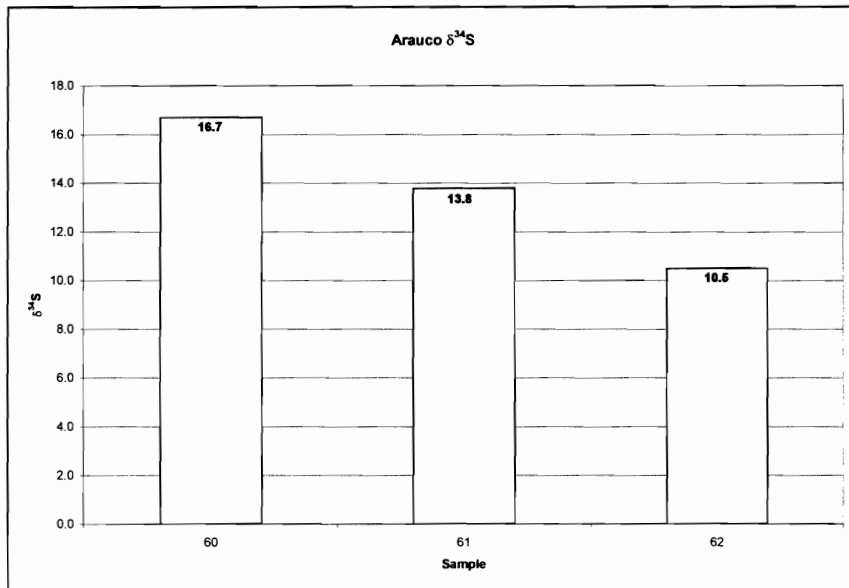
Figure 4.19 presents data from Arauco Norte, the northern zone of Arauco orebody clusters.  $\delta^{34}\text{S}$  values in this data set range from 7.4‰ to -0.2‰, and have an average value of 2.5‰, implying some degree of magmatic  $\delta^{34}\text{S}$  contribution. This part of the deposit lacks bituminous material, and is associated with a higher level of albitic alteration. Texturally, samples from this zone are quite heterogeneous, ranging from clearly hydrothermal (69) to multiphase cubes of pyrite. The sample furthest from 0‰ is associated with zoned (therefore multiphase) pyrite.

Figure 4.20 presents data from the Catedral and Morro orebody clusters, which are both in the northern part of the deposit.  $\delta^{34}\text{S}$  values range from -0.4‰ to -7.4‰, averaging -4.8‰, the lowest average. Textures in this set of samples are variable, and vary from poikiloblastic pyrite, which corresponds to 74, and has the closest value to 0‰ in this set to homogenous chalcopyrite.

Zoned cubic pyrite, with inclusion-free overgrowths, is indicative of multiple stages of growth. There appears to be a  $\delta^{34}\text{S}$  concentration pattern in this morphology (Figure 4.21). Several of the samples have elevated or fractionated  $\delta^{34}\text{S}$  values, and they are not from the same orebody clusters. This implies that a similar process occurred over a large area.



**Figure 4.17. Valdivia Sur  $\delta^{34}\text{S}$  values**



**Figure 4.18. Arauco  $\delta^{34}\text{S}$  values**



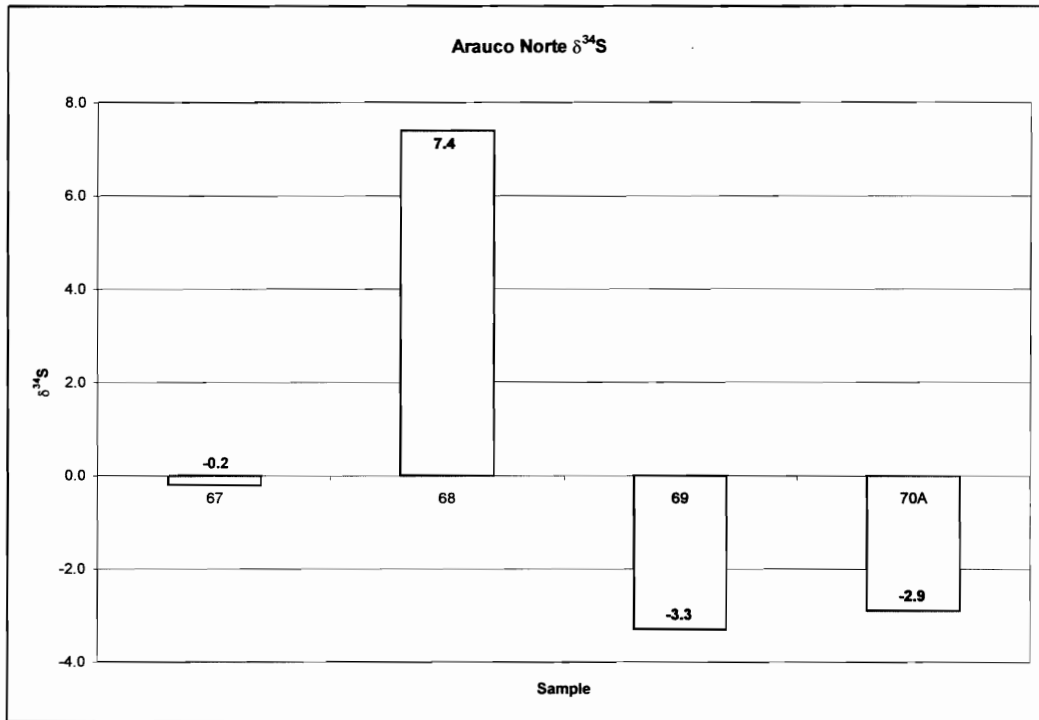


Figure 4.19 Arauco Norte  $\delta^{34}\text{S}$  values

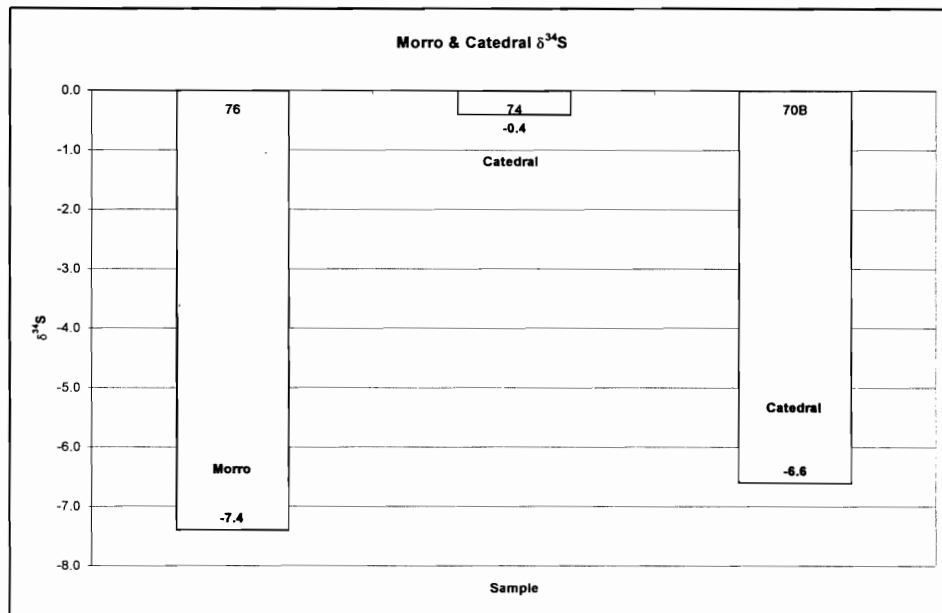
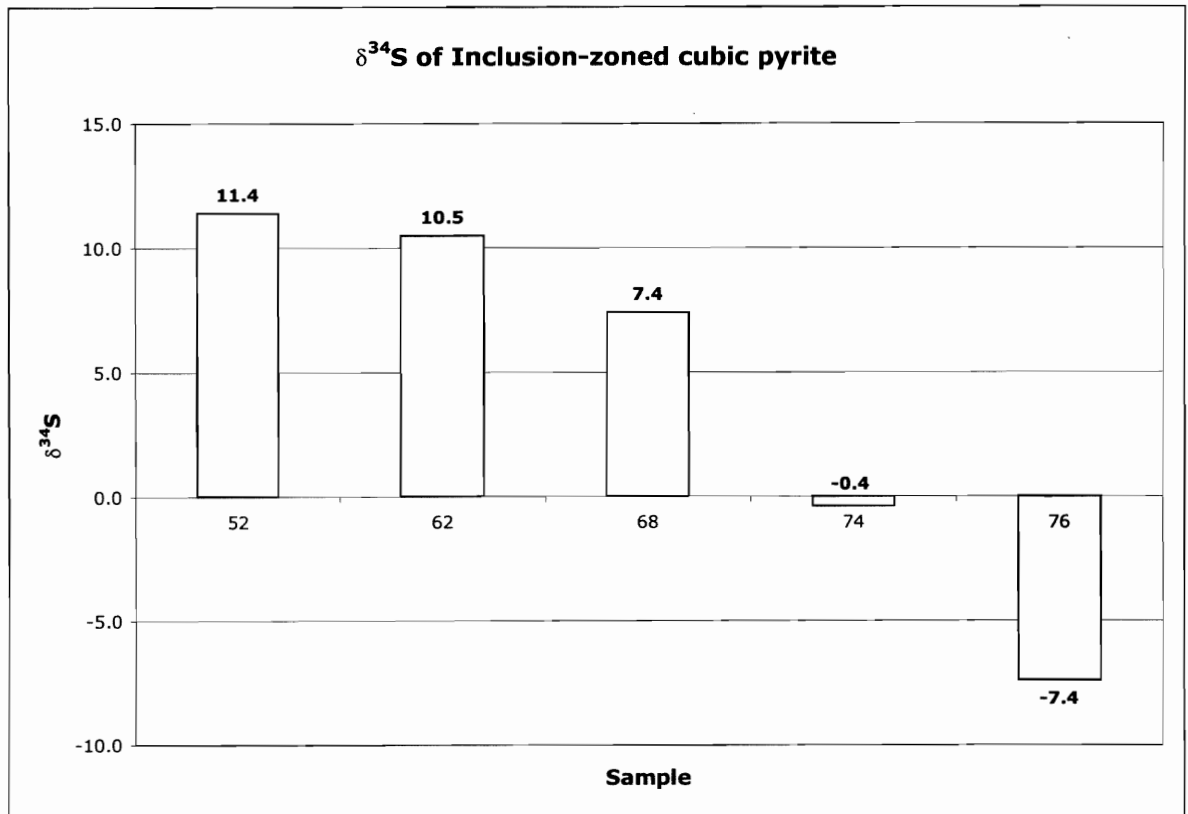


Figure 4.20: Morro and Catedral  $\delta^{34}\text{S}$  values



**Figure 4.21: Inclusion zoned cubic pyrite for all data**

Chart showing the  $\delta^{34}\text{S}$  range for all samples where pyrite, cubic and agglomerated, shows a zoned distribution of inclusions. An inclusion rich core and an inclusion-free rim characterize this morphology.

### 4.3.3: $\delta^{34}\text{S}$ Isotope Summary

The wide range of  $\delta^{34}\text{S}$  values is indicative of some degree of fractionation having occurred or that more than one source of sulphur is present. The range is not so large as to imply that it has been the predominant factor – 15% of the samples fall within the  $\delta^{34}\text{S}$  ‰ range accepted as characteristic of magmatic influence. High positive and negative  $\delta^{34}\text{S}$  values do not have a textural pattern consistent with fractionation e.g. framboidal pyrite, although many of the samples with high values do exhibit textures characteristic of low temperature environments such as colloform pyrite. Valdivia Sur and Arauco exhibit generally consistent values, while Morro and Catedral have varying values, indicating that in Valdivia Sur and Arauco similar processes persisted over orebody-sized scales. Inconsistent values from Arauco Norte and Catedral indicate that processes in these orebody clusters were not consistent over large areas, and more localized or discrete processes dominated. Furthermore the latter two sets of values also have  $\delta^{34}\text{S}$  closer to 0‰, indicating an influence by magmatic regimes or a greater degree of S homogenization with a great variety of values reservoir, which can also lead to near 0‰. This could occur through mixing of  $\delta^{34}\text{S}$  at a high temperature (> 200°C)

## ***CHAPTER 5: DISCUSSION: TO WHAT DEGREE IS EL SOLDADO PYRITE OF LOW – TEMPERATURE GENESIS?***

### **5.1.1 Introduction: Stage I Sulphides**

Previous chapters have introduced the area of study and developed the idea of a multi-stage process in the formation of the El Soldado manto-type copper deposit. The field relationships, geochemistry of Fe-sulphides, and petrographic analysis all play important roles in this formation. Part I of the discussion deals with the important role of Stage I in the formation of Cu ore, specifically with petrology, geochemistry, and S-isotopes. Recall from Chapter 1, that the primary aim of this thesis is to test the whether pyrite in this deposit is of low temperature origin, or of hydrothermal origin. As well, the control that framboids exert on the deposit is discussed.

### **5.1.2 Stage I Petrology**

Texturally there are several indications for a low T origin of Stage I. The textures indicative of low-T formation are framboidal pyrite, and colloform pyrite.

Framboidal pyrite was observed in high-grade orebody clusters e.g. Valdivia Sur, and traces of them were observed in several of the samples from the deep Valdivia Sur, those thought to be of hydrothermal origin. According to Wilson (1998), Stage I pyrite is preserved mainly in the peripheral parts of the orebody clusters. Many workers (e.g. Berner, 1970; Wilkin and Barnes, 1995; Rickard, 1970) provide supporting evidence for framboidal pyrite formation at low temperatures characteristic of diagenetic conditions.

This conclusion is supported through field and petrographic observations in El Soldado. Wilson (1998) observed a large proportion of framboidal pyrite suspended in bitumen, or thermally degraded petroleum (Figure 5.1). This relationship is important in constraining the temperature range of framboid formation, because of the three dimensional shape of framboids. In other studies (e.g. Wilson, 1998; Wilson and Zentilli, 1999; Boric, 2002) framboids have been observed in solid, thermally altered petroleum (bitumen). In order to form, framboids, which are spherical, must have grown while petroleum was liquid, in open space; confined spaces in a solid would result in irregular, or flat surfaces. This relationship constrains framboid genesis to temperatures in the “liquid oil window”. Depth of burial, duration of heating, and source or type of original organic matter influence the temperature at which liquid oil is formed (North, 1985). A general value, called the level of organic metamorphism, LOM, is applied for the needs of this study. According to LOM parameters, the liquid oil window begins at about 60 °C, and closes at approximately 140 °C (North, 1980).

Framboids can be formed through processes involving dissimilatory bacterial sulphate reduction (e.g. Goldberg, 1974; Nielson, 1979). Bacteria are restricted to temperatures where life can survive, normally considered to below 90 °C for sulphate reducing bacteria, except for the deep oceans, where bacteria survive near hydrothermal vents at temperatures above 100°C.

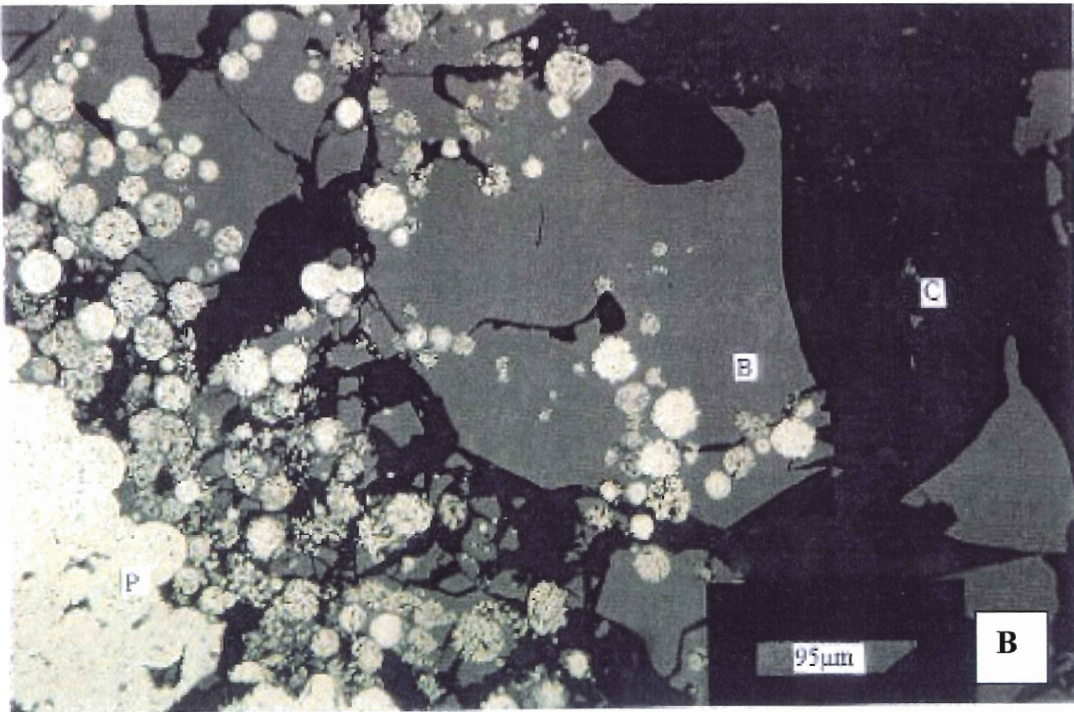
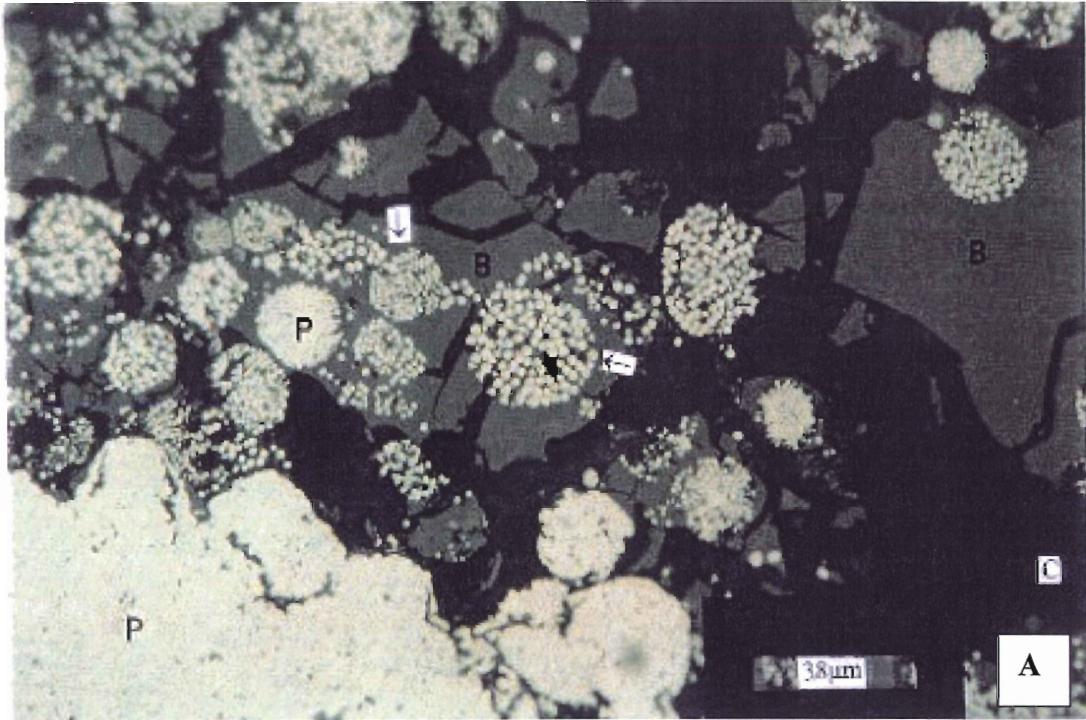
**Figure 5.1 a, b**

Reflected light micrographs showing the intimate relationship between bitumen (B) and framboidal pyrite. Bitumen must have been liquid petroleum at the time of framboid formation in order to form the spheroidal shape. Bitumen is not present in samples from the north, in deep Morro, or in the Valdivia Sur orebody clusters in samples studied in this thesis. Images are used, with permission, from Wilson (1998).

B = bitumen

P = pyrite

C = calcite



Cubic pyrite in some samples appeared to be both Stage I and Stage II, based on crosscutting relationships. Many cubes were more corroded or xenomorphic, with partial replacement by Cu sulphides, while a second generation, primarily suspended in late calcite were more euhedral (e.g. Figure 4.12). This indicates multiple stages of pyrite formation in most samples.

Colloform pyrite, observed in Valdivia Sur, is also named “melnikovite-pyrite”. Melnikovite pyrite forms from an  $\text{FeS}_2$  gel, at low temperature as a fine-grained precipitate (Ramdohr, 1980). Melnikovite pyrite is susceptible to replacement due to its inherent instability. This form of pyrite is characterized by a brownish colour in reflected light. Melnikovite pyrite was not observed in El Soldado. Pyrite and melnikovite pyrite are both  $\text{FeS}_2$  and microprobe or x-ray diffraction analysis cannot distinguish between them. According to Ramdohr (1980) colloform pyrite is very common in low temperature deposits. Replacement by or conversion to true pyrite could be the reason for its absence.

Marcasite, a dimorph of pyrite also forms at low temperatures, becoming unstable at elevated temperatures (Ramdohr, 1980). Plate-like structures, which are typical of marcasite, were observed in the bands between growth rings of the colloform structures (Figure 4.15). Pyrite does not form in this habit, thus replacement of a previous mineral structure must be employed to explain the observed morphologies. Ramdohr indicates that pseudomorphing, or conversion to ordinary pyrite, of marcasite and colloform or melnikovite pyrite is common due to the instability of the latter two phases. Microprobe imaging of several zones of colloform structures, as well as some non-colloform structures indicate chemical zoning, revealing shapes characteristic of melnikovite or marcasite morphology (Fig 4.8B, 4.2, 5.2b).



Zonation in colloform textures, as alternating bands of calcite and pyrite, could be explained through the preferential replacement of a less stable low-T phase, such as melnikovite or marcasite reflecting the absence of these two FeS<sub>2</sub> phases. Colloform textures displayed distinctive chemical variation in the spherical core, as microcryst aggregates (Figure 4.14). Microcrysts are characteristic of framboids, implying colloform textures formed after framboids. Growth rims in colloforms indicate a prolonged period of formation under favourable and consistent temperature and chemical conditions, and not rapid growth, as the late Stage II phase was. Later thermal metamorphism resulted in the annealing or recrystallization of framboids to massive pyrite. According to geochronological studies by Boric (2002) and Zentilli & Wilson (1999), Stage I genesis occurred over a prolonged period, while Stage II was relatively brief. Based on this, the above textures were created during Stage I at low temperatures. Zonation of texture and chemical composition in samples from Arauco Norte, and deep Valdivia Sur show evidence for multiple stages of pyrite growth. These samples, (Figure 4.16 & 5.3), suspected to have formed late and at high temperature have a distinctive core-mantle relationship. Texturally this demonstrates at least two distinct phases of pyrite growth.

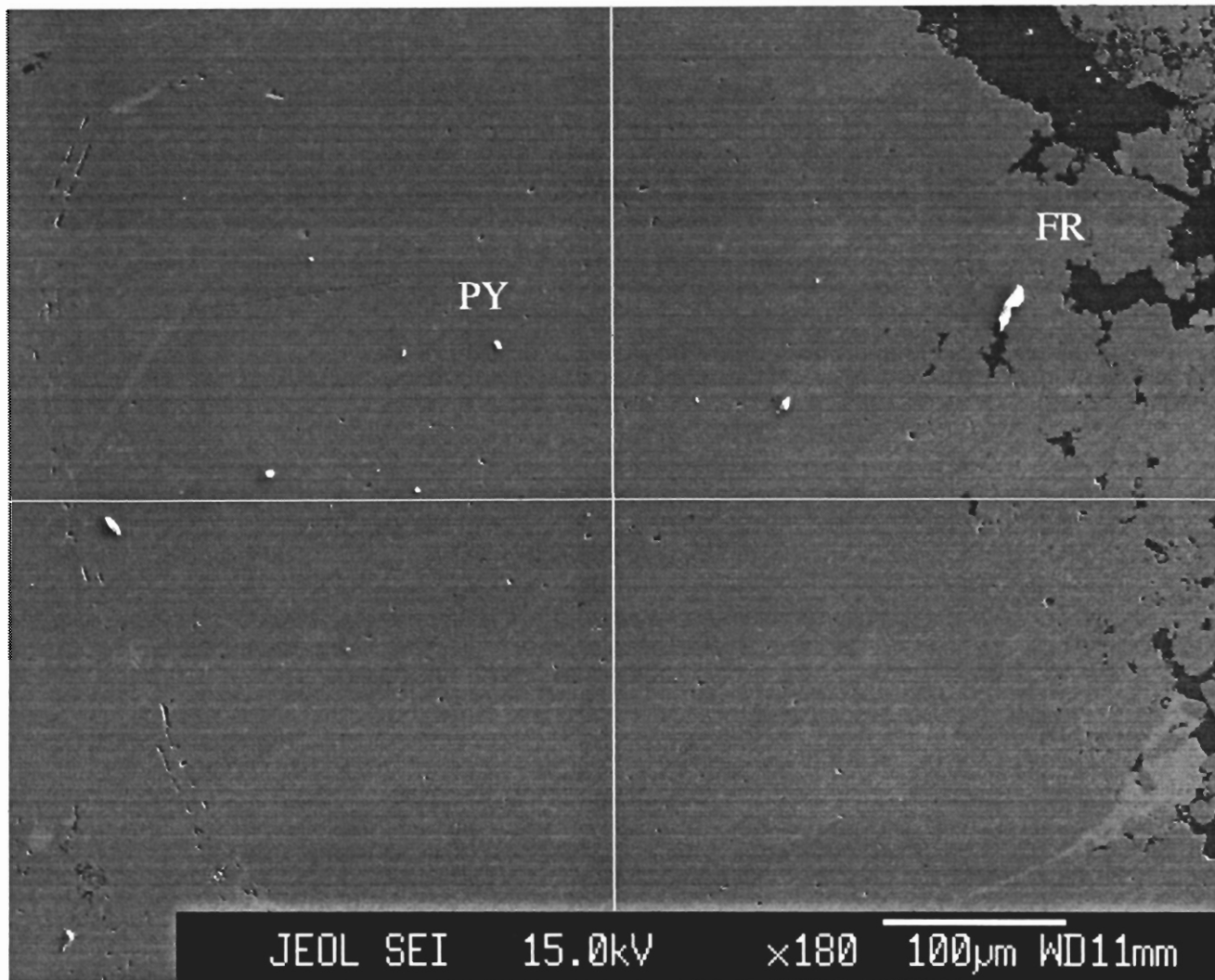


**Figure 5.2a: SEI microprobe image of framboidal pyrite zone**

Electron micrograph (SEI) of PC-02A. This sample is from the Valdivia Sur orebody cluster. This image shows, a pyrite zone (PY), which resembles framboidal pyrite; spherical shapes on the right hand side and top right corner resemble clusters of poorly defined framboids (FR). This image is similar to what would be observed in reflected light, illustrating the homogeneity of some zones of pyrite suspected to be Stage I. Note that parallel lines running from the top right to bottom left corners are artifacts from imaging, and do not represent any physical quality of the sample (pers. comm., Bob MacKay).

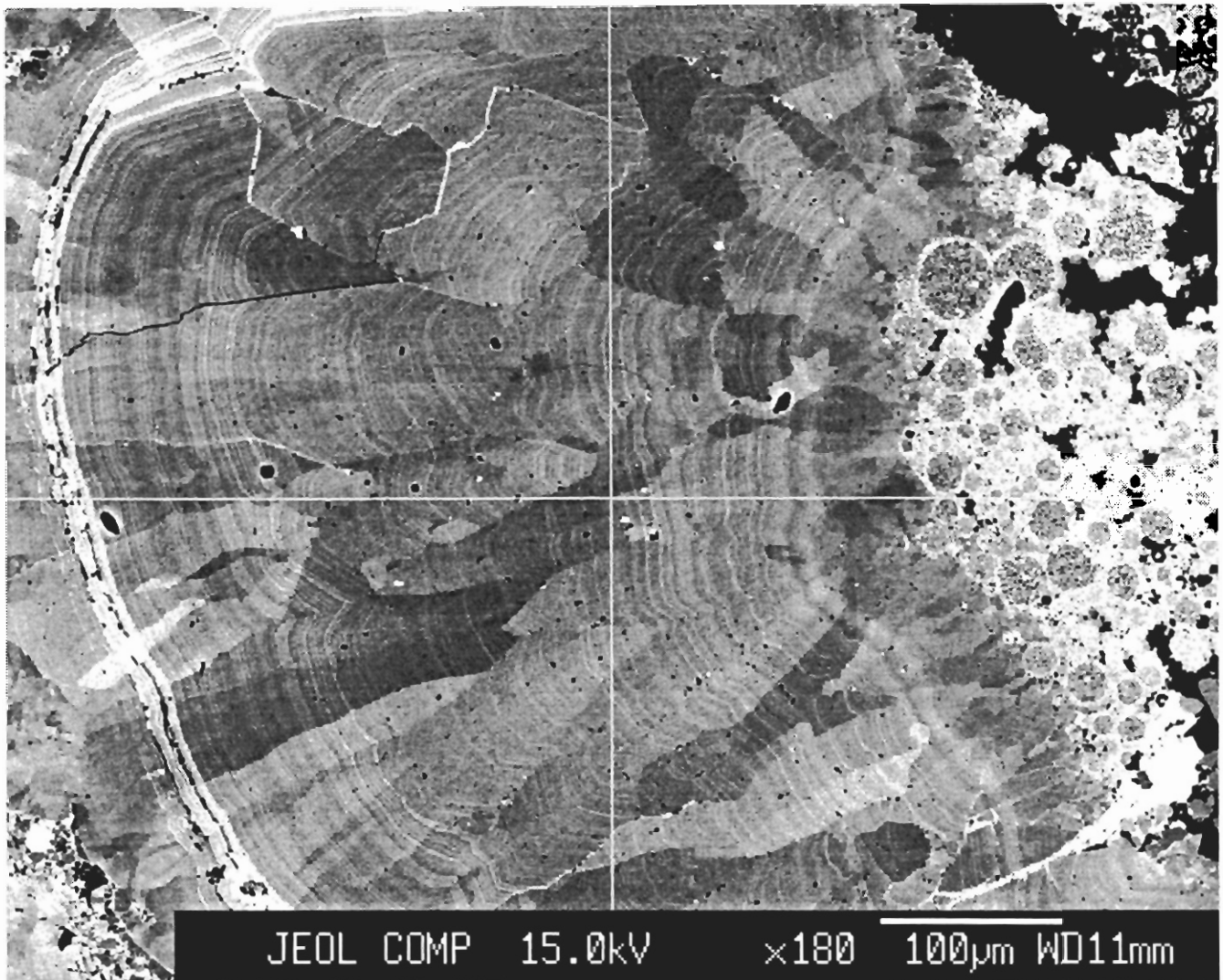


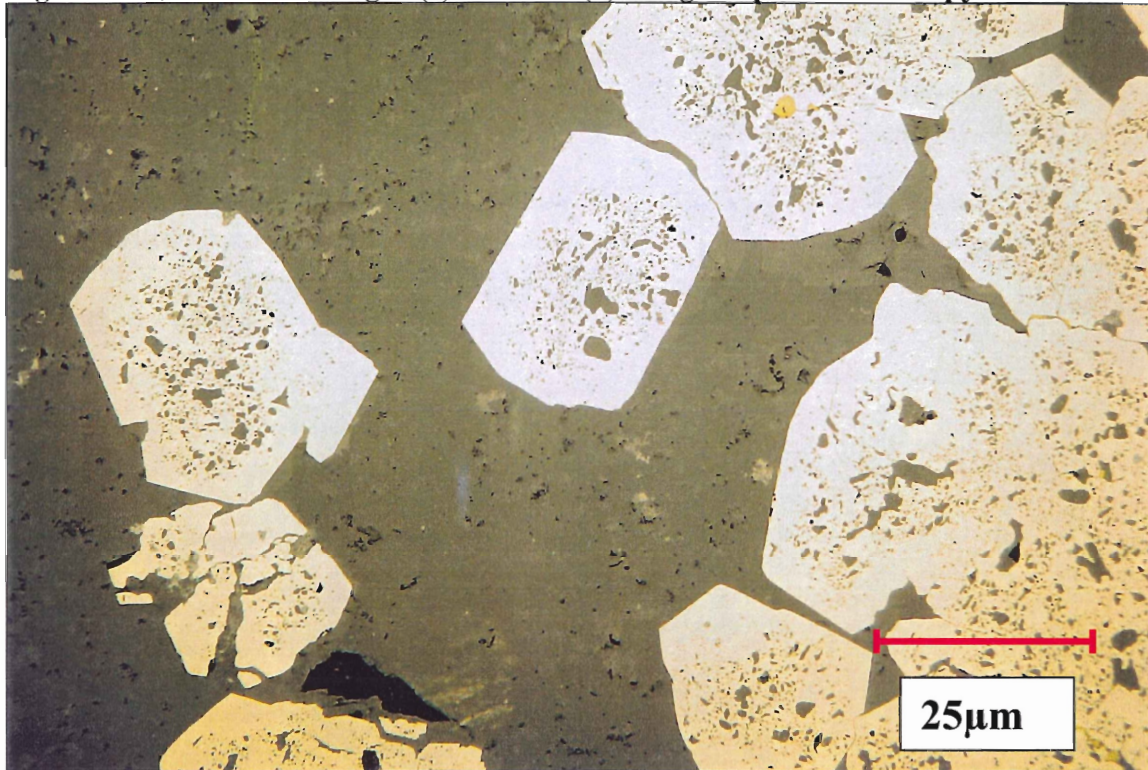
**Figure 5.2b: Compositional microprobe image of framboids**

Electron micrograph of the exact same spot as Fig. 5.1a. BSE image showing the compositional variation, by elemental variability. This type of image does not quantify or identify the nature of compositional variation. Of importance in this spectacular image is the high degree of heterogeneity in composition. Framboidal pyrite is revealed only through chemical variability, indicating recrystallization or some other form of annealing. The alternating bands in the center to the left of the image are growth bands formed by the slow growth of layers of pyrite from circulating fluids of varying composition. The variation in composition, especially in the center portion of the image could indicate that a different phase of pyrite, such as marcasite, existed in early growth phases but was later converted to pyrite proper. Note that this texture is remarkably similar to that of Figure 4.2, which is of bornite that has replaced pyrite, but is not in the vicinity of framboidal pyrite, indicating that whatever has caused this variation is persistent.

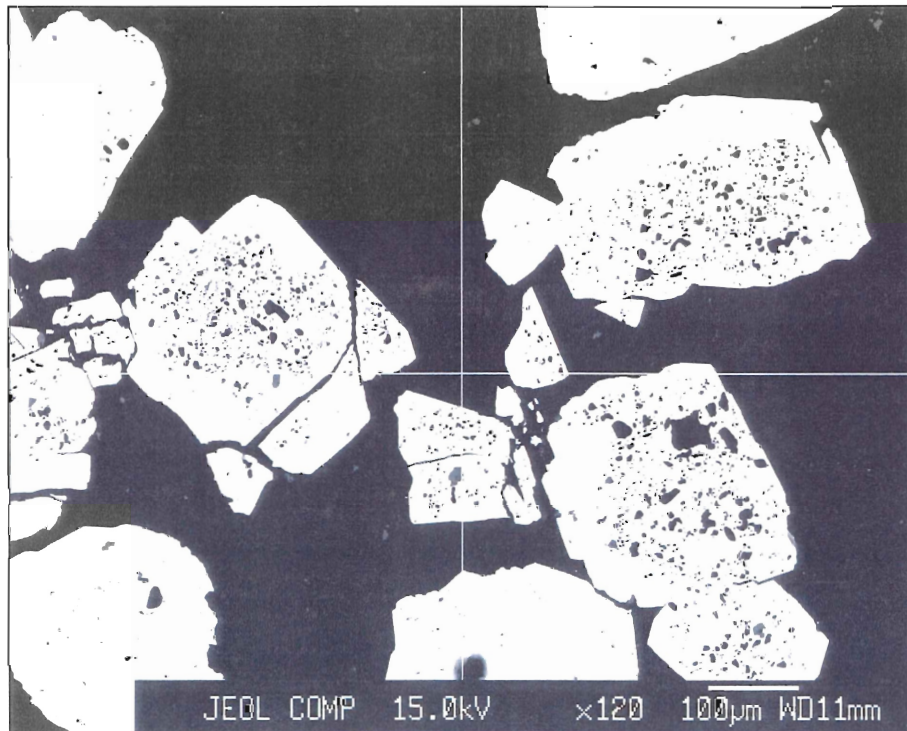
**Figure 5.3 a, b**

Figure 5.3a is a reflected light image, and 5.3b is a composition microprobe image. These two figures show the distinctive zonation in some cubic pyrite cubes from MP2001-74, from the Cathedral samples and other ore bodies, which share this texture. The cores are characterized by a high frequency of inclusions. The rim is characterized by overgrowths that are almost completely free of inclusions. Rims have a higher level of As than cores. This pattern of overgrowths was observed in several samples. This pattern is not found just in cubes, but in large aggregates of cubes (e.g. Fig 4.16) and more massive zones as well, giving a relative indication of a second phase of fluid circulation.

Figure 5.3a, b: Reflected light (a) and SEI (b) image of poikiloblastic pyrite cubes



b.



### 5.1.3 Stage I Geochemistry

Arsenic is concentrated preferentially in certain morphologies. Framboids, the immediate zone around framboids, and fresh overgrowths on some poikiloblastic and euhedral pyrite cubes and agglomerates are all slightly enriched in As. Figure 5.4 illustrates chemical zoning in the region surrounding a pyrite framboid being replaced by chalcopyrite.

Manning and Gize (1993) show that As can be enriched in oil field brines and petroleum. The presence of bitumen in the proximity to some framboidal zones, and the noted relationship between framboids and this thermally degraded petroleum imply that some As could have been incorporated during formation.

Otswald & England (1977) indicate that microprobe analysis of euhedral pyrite can detect zoning of As in the core of the cubes. They state that framboids can have high levels of As, and during recrystallization into cubes, As enrichment is preserved. The known progression from framboids to massive homogenous pyrite at El Soldado implies some massive pyrite also should be enriched, similar to that noted by Otswald and England (1977).

In summary, two points indicate a low temperature origin, based on the geochemical trends and texture of pyrite. The first point is the relationship between bitumen and framboids, as is well documented by Wilson (1998). Framboids formed within petroleum when it was liquid, which constrains the temperature to below ~140 °C (North, 1985).

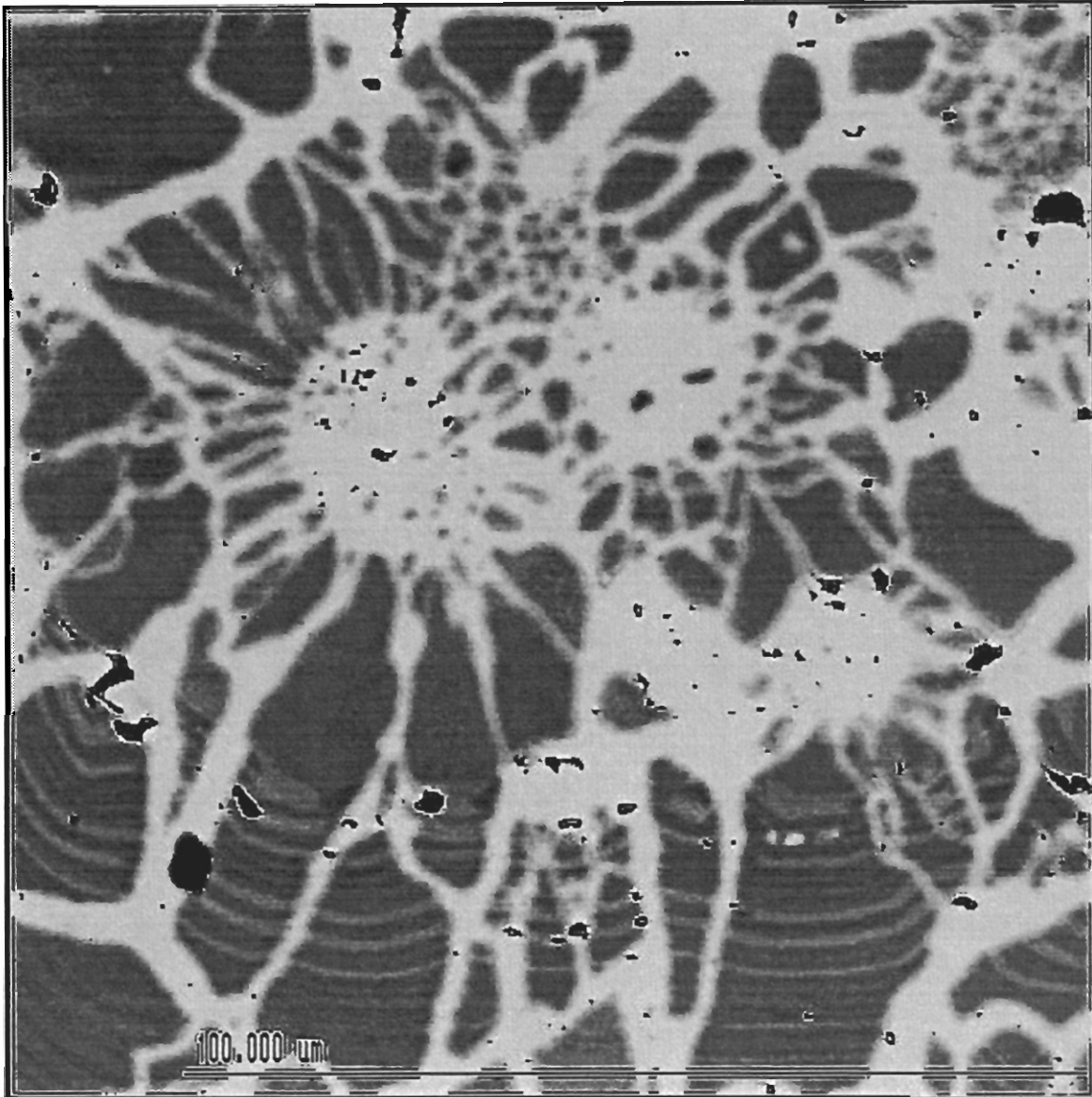


**Figure 5.4: Compositional zonation and atoll structures in framboids**


Compositional electron micrograph of PC-04 showing chemical zonation in the form of alternating light and dark bands. Due to the very small scale of this banding it is not possible to analyse accurately. It is possible that this is related to growth banding, as in Fig. 5.2b, or perhaps it is due to As enrichment. Light grey is chalcopyrite, and dark grey is pyrite. The central structures are framboid-atolls, where chalcopyrite has preferentially replaced framboids.

Black spots are holes in the slide, or gangue (R. MacKay, pers. comm.)

A process that would account for As enrichment in fresh, inclusion-free overgrowths is remobilization of As from originally enriched framboids. During replacement of framboids during Stage II metallogenesis As would be liberated, allowing circulation in hot mineralizing fluids. Then, As was re-precipitated with late hydrothermal pyrite on Stage I pyrite that was not originally enriched in As. Microprobe composition images of cubic pyrite, some with inclusions and some without shows distinctly multiple phases of growth (Figure 5.5).

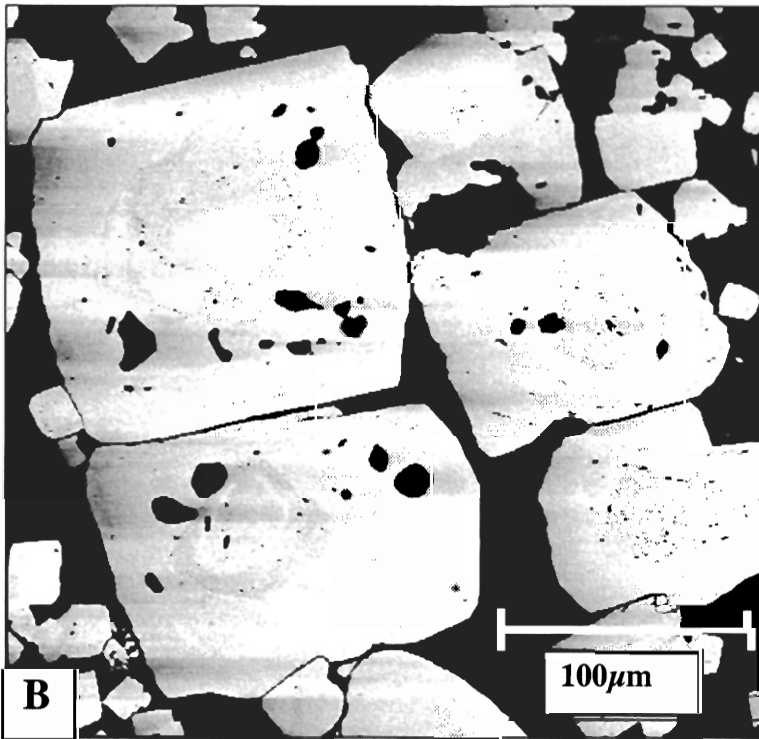
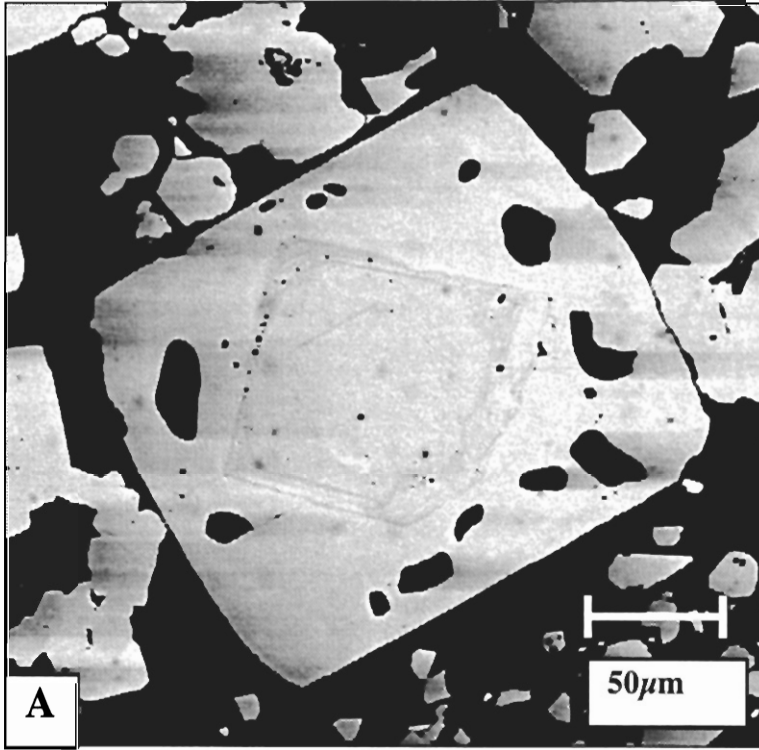
While it cannot be proven in this study that poikiloblastic pyrite represents a low-T phase of growth, the combination of As distribution in morphologies characteristic of low temperature growth, combined with the enrichment in rims of pre-existing pyrite indicates this is a plausible explanation





**Figure 5.5a, b: Multiple stages of pyrite growth**

Electron microprobe composition micrograph of MP2001-76. Cubes of pyrite in both A and B display distinct chemical variation. Chemical variation appears to be related to different phases of growth. The cores of cubic pyrite are surrounded by offset growth of later pyrite. Inclusions are also zoned, occurring distinctly along the boundary between two phases of growth. Black matrix is calcite. Sub-horizontal streaking is an artifact from probe imaging (R. MacKay, pers. comm.)



#### 5.1.4 $\delta^{34}\text{S}$ Isotope Geochemistry

The wide range in  $\delta^{34}\text{S}$  values (24.5‰) implies that sulphur fractionation has occurred, and since this data, with the exception of MP2001-70B, represents pyrite, fractionation of sulphur in pyrite has occurred.

It was expected, based on petrography of the samples before S-isotope results were obtained, that some values would show little deviation from 0‰, while others would show strong deviation: samples that displayed the most euhedral pyrite morphologies would have values closest to 0‰ while samples that displayed textures consistent with a low temperature genesis would have fractionated values.

Samples that displayed euhedral pyrite, were suspected to be of hydrothermal origin, but did not always have a corresponding low, or close to 0‰  $\delta^{34}\text{S}$  value (e.g. MP2001-61, 62, 68). Samples dominated by framboidal or colloform textures, thought to be of low-T origin, sometimes had low  $\delta^{34}\text{S}$  values (e.g. MP2001-50)

Samples MP2001-70A, 69, 68 and 67 are proximal to a gabbroic intrusion (Figure A.4), and display some evidence low for interaction with hydrothermal S. With the exception of 68, all these samples have negative  $\delta^{34}\text{S}$  values, showing less fractionation. These samples had the highest level of alteration (potassic and albitic), perhaps indicating fluid interaction, likely from the intrusion, or related to the intrusion.

Inconsistencies between texture and isotopic values indicate that there has likely been local input of  $\delta^{34}\text{S}$  into the system, or homogenization of the S reservoir. Combined with the overlap of high  $\delta^{34}\text{S}$  values in seemingly hydrothermal textures, it also appears that some  $\delta^{34}\text{S}$  has been remobilized or recycled and deposited later as a newer generation

generation of pyrite, effectively distorting the expected results. More study is warranted on the timing of the intrusion emplacement with respect to euhedral pyrite growth.

Due to the non-specific collection of sulphides for analysis, it is likely that values from all samples represent an average of several textures of pyrite, thus different modes of formation and therefore perhaps different degrees of fractionation of  $\delta^{34}\text{S}$  within a sample.

### **5.1.5 Implications for metallogenesis**

Repeated occurrences of framboidal pyrite, especially in the high-grade orebody cluster of Valdivia Sur, were often associated with atoll, or atoll-like structures (e.g. Fig. 4.1, 4.11), which are formed through the preferential replacement of one phase or morphology. This propensity of framboidal pyrite to form atolls indicates framboids have some control in mineralization or replacement. Speculatively, the original instability of griegite or other iron monosulphide framboid precursor phases, has been inherited by framboidal pyrite. Perhaps this instability allows replacement by Cu-rich fluids to operate at a slightly lower energy level, making it easier to replace them than more massive pyrite. Alternatively, the physical character of the framboids, which have immense surface area, makes them more susceptible to replacement. Regardless of process, framboidal pyrite appears to play a role in the degree of mineralization or replacement, at least in some regions of the deposit.

### **5.1.6 Fluid Inclusions**

Fluid inclusions analysis was not conducted during this study, but there have been studies in the past done on El Soldado. In Figure A.4, the locations of four fluid inclusion sample points are plotted, so that a comparison between the texture and known temperature of the area could be made. Table B-2 presents relevant data for temperatures in the proximity to samples MP2001-67, 68, 69, 70A. Note that except for sample A, which has a T max of 296 °C, and C, with a T max of 280 °C, temperatures are still relatively low. The data do not seem to correspond to temperatures related to the gabbro/diorite intrusion, which would be much higher (~800 °C, Best et al., 2000). These temperatures imply that the intrusion did not reset earlier temperatures. However, isotope values from these samples are the lowest in the data set, implying some late homogenization or interaction in the vicinity to the intrusion occurred.

### **5.1.7 Conclusion**

Pyrite characterized by framboidal, colloform, and poikiloblastic textures is typical of a low temperature of formation. The presence of euhedral pyrite in late calcite, as well as fresh overgrowths of pyrite indicates that more than one stage of pyrite exists. The second stage pyrite is less pervasive or voluminous relative to low-T pyrite.

Late pyrite overgrowths were sometimes characterized by a relative enrichment of As, which was also concentrated in framboidal zones. This implies that As has been re-deposited in a later phase of pyrite, perhaps mobilized during Cu metallogenesis.

The wide range of  $\delta^{34}\text{S}$  values both a low temperature phase, which dominates the data set, and a magmatic source or high temperature homogenization of S isotopes. Most low or negative values were in the general proximity to a late stage gabbroic intrusion.

Alteration was heaviest in this zone, and textures were the most like that expected for hydrothermal deposition.

Overall, a combination of events appears responsible for the present state of mineralization at El Soldado. Early on, diagenetic conditions were dominant, and a low temperature, reducing environment favoured the formation of framboidal and colloform pyrite, slowly evolving over millions of years. Late in the formation of the deposit, intrusions locally and regionally, provided energy and possibly some S, resulting local fluid circulation that ultimately lead to Cu deposition.

## **CHAPTER 6: CONCLUSIONS AND FUTURE RESEARCH AVENUES**

### **6.1: Conclusions**

Petrographic observations from this study, consistently showed cross-cutting relationships between pyrite, chalcopyrite, bornite and calcite indicates multiple phases of mineralization, with the majority of pyrite, which is cut by virtually every other phases, as the earliest. Textures of early pyrite indicate a low temperature of formation, possibly comparable to diagenetic conditions. Textures characteristic of a low temperature of formation are framboidal pyrite, which in some cases shows evidence of recrystallization, and colloform pyrite. The type of chemical environment that favours the development of these textures is that of relatively stable fluid chemistry and temperature, near neutral pH. These conditions appear to have prevailed in El Soldado based on microprobe compositional images, which show the record of many stages of growth, expressed as subtle variations in chemistry in the circulating fluids. Analysis of pyrite also indicates that in addition to the cross-cut early pyrite, there exists pyrite with a distinctly different texture, characteristic of a higher temperature of formation, that of euhedral pyrite cubes and pyritohedrons. Based on the fact that this pyrite is suspended in a matrix of calcite that cuts all other phases, it appears that this pyrite is the latest.

Chemically there is evidence for re-mobilization of arsenic, which has been concentrated first in the low temperature framboidal pyrite, and then re-mobilized and re-precipitated in late over-growths on Stage I poikiloblastic pyrite cubes.

Sulphur isotope analysis has lead to the conclusion that the majority of pyrite preserves a fractionated sulphur characteristic (-7.4‰ to 17.1‰). As noted above, the

dominant mode of fractionation, due to the lowest energy input required by nature, is by dissimilatory sulphate reducing bacteria. Like all life, these bacteria cannot live at elevated temperatures, and therefore seem to have played a role in the genesis of low temperature pyrite. There does appear to be some input of hydrothermal, or igneous derived S or homogenization of the S reservoir, which has resulted in some samples yielding values of  $\delta^{34}\text{S}$  near 0‰. The degree of this input is minimal, and is restricted to the vicinity of a gabbroic intrusion.

This evidence implies a diversified deposit, in terms of the different styles of genesis that have combined to form the El Soldado deposit. Low temperature pyrite appears to be an integral component of the deposit, for without it, and the instability inherited by it from early framboidal genesis, there might not have been as pervasive or widespread Cu mineralization. Pyrite appears to have controlled the replacement to some degree, perhaps resulting in the zonation present today.

## **6.2: Future Research Avenues: Useful Projects on El Soldado**

This study has answered in part several questions about the genesis of El Soldado, determining the role of pyrite in the deposit, as well as the significance of framboidal pyrite. However, there are several questions that remain either unanswered, having never been attempted to be answered, and others that have in the past been studied, but now are out of date or rely themselves on false reasoning.

One study that would prove to be exceptionally useful is a fluid inclusion study that uses sulphide minerals and fluid inclusions in interstitial calcite. This would allow



direct study of the formation temperatures of the sulphides, ending the debate of temperature of ore genesis.

Studying the relationship between igneous intrusion emplacement in the El Soldado camp and pyrite growth would also be a useful study. This would help to constrain the timing of different stages of pyrite growth.

## **Appendix A**

3-D Sample Locations: Plotted in Plan and Cross Section

## Figure Captions for Figures A.2 to A.5

### **Figure A.2**

Plan view of the El Soldado deposit at the 830m level. Refer to A.1 for legend. Note the correspondence between plan and cross section zonation. Block A represents in roughly equal intervals, from left to right MP2001-50, 51, 52, PC-03, PC-04, PC-02, and PC-01. Block B represents from left to right samples MPP2001-67, 68, 69, 70A. Modified from Boric, 2002.

### **Figure A.3**

Cross-section showing samples MP2001-67, 68, 69, and 70A. In addition, points A-D represent sample locations for fluid inclusion data refer to in Chapter 5. Modified from Boric, 2002.

### **Figure A.4**

Cross-section showing samples MP2001-76, 74, and 70B. Note that Mp2001-74 is actually projected from the +50 N level, thus lithology/metallogeny may be somewhat different in actuality. Modified from Boric, 2002.

### **Figure A.5**

Cross-section showing samples PC-01, 02, 03, 04 and MP2001-50, 51 and 52.

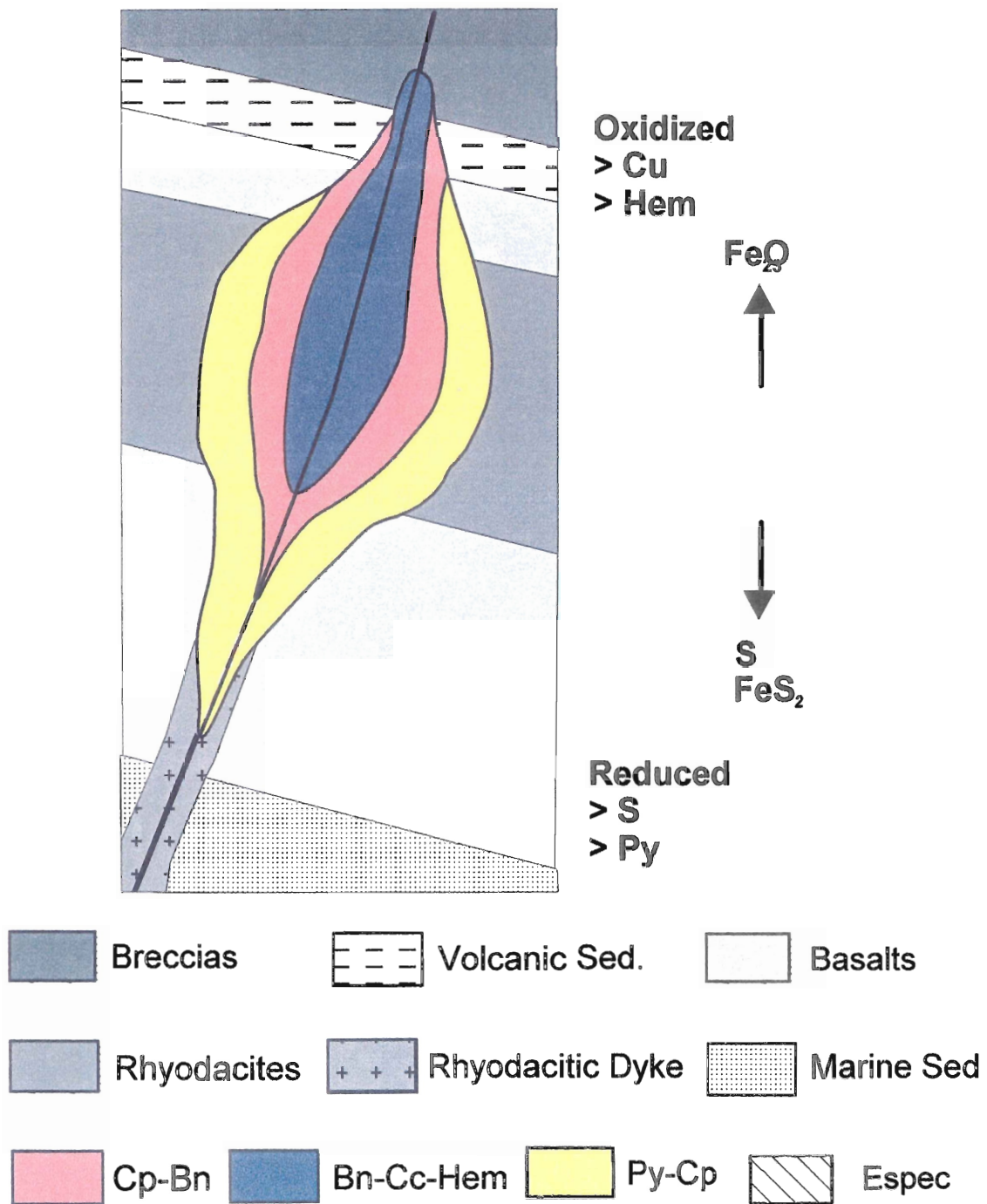


**Figure A.1**

This figure illustrates the general zonation of the ore body clusters, and their lithological distribution. Modified from Boric, 2002. This legend is applicable to all Appendix A figures.

Figure A.2

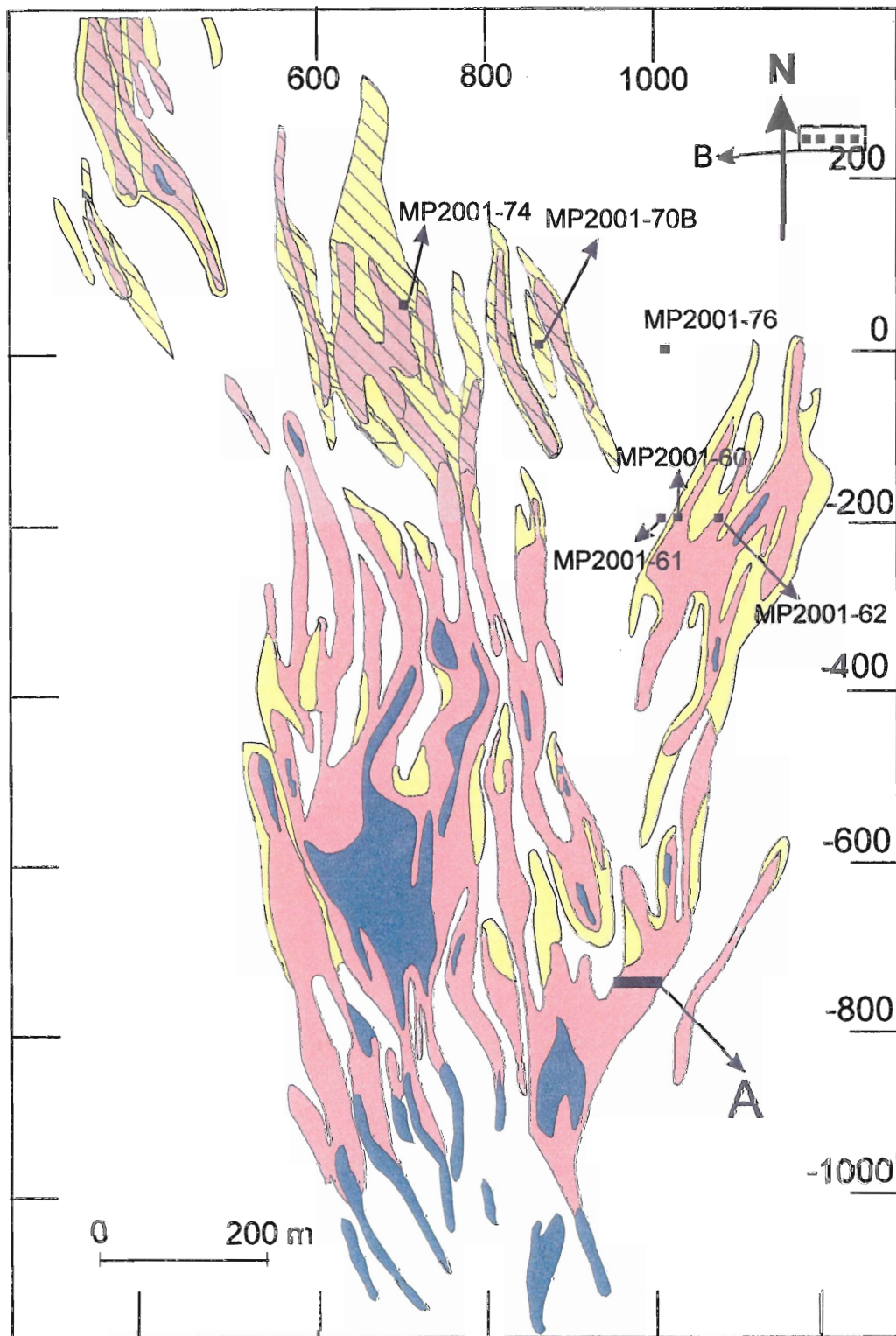


Figure A.3

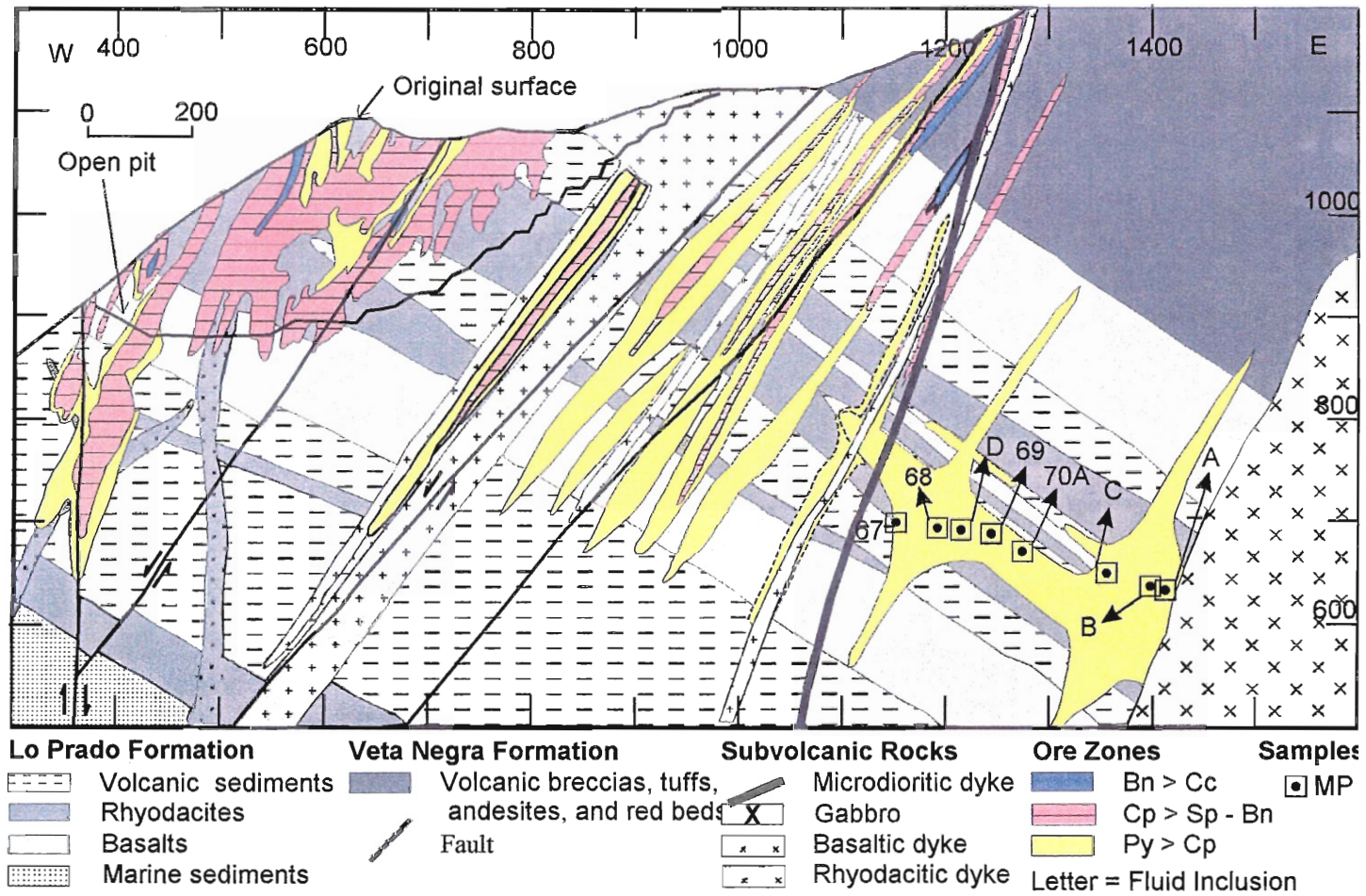
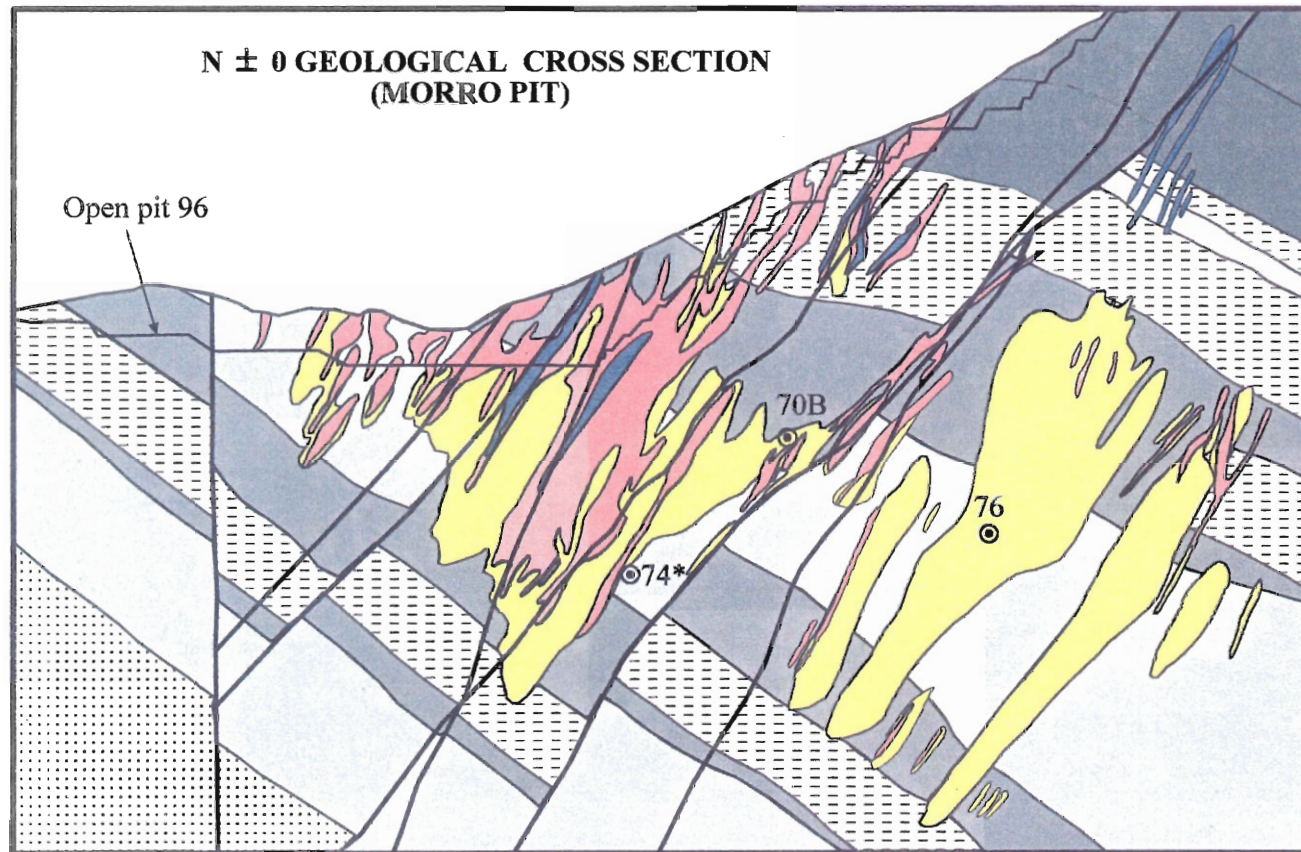


Figure A.4

118



**Lo Prado Formation**

- Volcanic sediments
- Rhyodacites
- Basalts
- Marine sediments

**Veta Negra Formation**

- Volcanic breccias, tuffs, andesites, and red beds
- Fault

**Ore Zones**

- Bn > Cc
- Cp > Sp - Bn
- Py > Cp

**Samples**

⊙ MP



200m

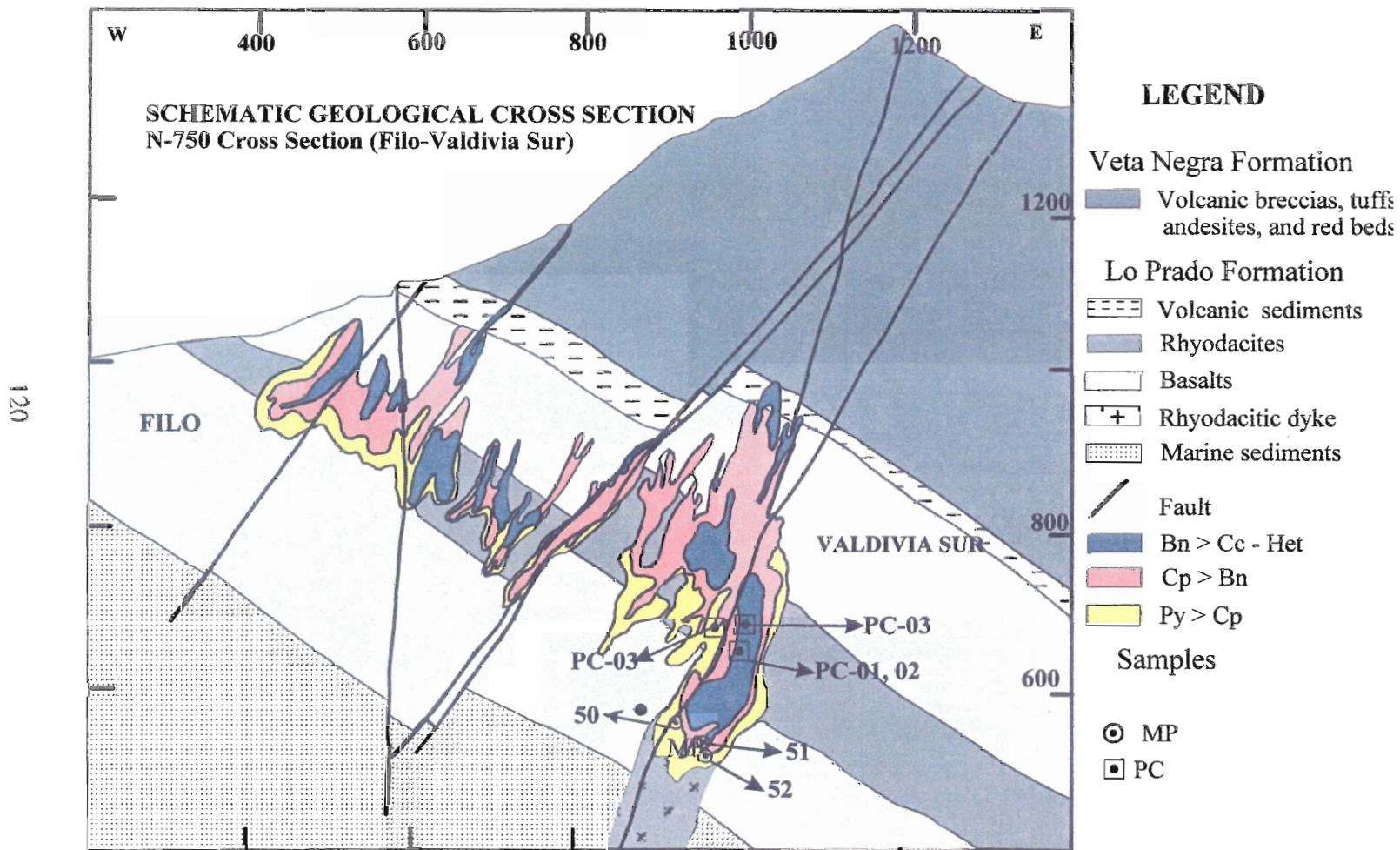
Figure Captions for Figures A.5

**Figure A.5**

Cross-section showing samples PC-01, 02, 03, 04 and MP2001-50, 51 and 52.



Figure A.5



## **Appendix B**

### Summary of Geochemical and mineralogical Data

**Table  
B.1**

Sample	Orebody	Mine Coordinates		Elevation (m)	DDH	meters		Ore type, relative percent $\delta^{34}\text{S}$			
		North	East					pyrite	chalcopyrite	bornite	
PC-01	Valdivia Sur	-750	987	664	S751	207.7	207.8	10	25	65	n/a
PC-02A	Valdivia Sur	-750	988	664	S751	209.7	209.85	97	2	1	n/a
PC-02B	Valdivia Sur	-750	988	664	S751	209.7	209.9	97	2	1	n/a
PC-03	Valdivia Sur	-750	968	675	S751	186.5	186.6	40	20	40	n/a
PC-04	Valdivia Sur	-750	985	666	S751	205.8	205.9	15	85	0	n/a
MP2001-50	Valdivia Sur	-750	918	544	SP507/84	243.7	243.8	100	0	0	6.3
MP2001-51	Valdivia Sur	-750	937	512	SP507- 84	280.1	280.2	100	0	0	17.1
MP2001-52	Valdivia Sur	-750	943	500	SP507- 84	293.9	294	100	0	0	11.4
MP2001-60	Arauco Norte	-200	1015	650	S6/95	71.75	71.85	100	0	0	16.7
MP2001-61	Arauco Norte	-200	1002	639	S6/95	85.90	86.00	100	0	0	13.8
MP2001-62	Arauco	-200	1048	541	S119/96	46.00	46.10	100	0	0	10.5
MP2001-67	Arauco Norte	250	1152	695	S250/88	584.00	584.10	100	0	0	-0.2
MP2001-68	Arauco Norte	250	1190	687	S250/88	621.00	621.10	100	0	0	7.4
MP2001-69	Arauco	250	1248	672	S250/88	679.00	679.10	100	0	0	-3.3
MP2001- 70A	Arauco	250	1279	662	S6/95	85.90	86.00	100	0	0	-2.9
MP2001-	Catedral	$\pm 0$	845	866	S200/01	177.10	177.20	100	0	0	-6.6

70B											
MP2001-74	Catedral	50	685	712	S95/98	98.80	98.90	100	0	0	-0.4
MP2001-76	Morro	+ 0	1016	761	SP507/84	243.7	243.8	95	5	0	-7.4

This table summarizes the all of the S isotope data and mineralogical data collected for this study. Mine coordinates, and drill hole measurements were kindly provided by R. Boric.

**Table B.2**

Sample	Mineral	T Minimum °C	T Maximum °C	Meters in Drill Core	Host Lithology	Observations (R. Boric)
A	calcite	240	296	870.5	rhyodacite	in contact with gabbro/diorite
B	calcite	118	200	858	rhyodacite	
C	calcite	169	280	812.5	altered sediments/tuffs	similar to MP2001-69
D	calcite	120	235	659	altered sediments/tuffs	close to MP2001-68 and 69

This table shows relevant fluid inclusion data for El Soldado where data are close to samples used in this study. Data summarized from Holmgren (1985;1987), Skewes (1988). Note that in B, C, and D, temperatures are much within a low temperature range, and do not show influence of high temperature hydrothermal fluids.

## **Appendix C**

Sample Descriptions for those samples not given in Chapter 4.

## Sample Descriptions

Refer to Chapter 4 for other samples, and Table B 2.1 for mineralogy and  $\delta^{34}\text{S} \text{‰}$

### PC-03

Pyrite occurs primarily as large (up to 300x600 $\mu\text{m}$ ) and aggregated subidioblastic cubes (~10-400 $\mu\text{m}$ ). Grains are being replaced by chalcopyrite and bornite. Chalcopyrite replacement is as net-like veinlets, and sometimes as forceful injections. Some degree of replacement appears to be cleavage controlled, as larger veinlets of chalcopyrite propagate along cleavage (Figure AI.1). Cores of large grains are homogenous. Framboidal pyrite is present, usually only revealed at edges of grains where replacement is strongest.

Chalcopyrite occurs primarily as a replacement of pyrite, dominantly as veinlets, which partially to fully cut pyrite grains. Chalcopyrite often occurs as large blebs, where near complete replacement has occurred, leaving a small portion of pyrite grain as a core. Atoll replacement structures are common where chalcopyrite is replacing framboidal pyrite, leaving a ring of pyrite. Some cleavage controlled replacement of bornite, or exsolution from bornite also present

Bornite is the primary matrix phase, all other phases appear to be suspended in it.

Commonly creates atoll structures as replacement of pyrite occurs. Bornite, based on cross-cutting relationships, is the last stage of replacement.

### MP2001-51

Sample is from the pyrite zone, and is cut from a <5mm pyrite vein. Pyrite is ~98% of the mineralization; the last 2%, as accessory minerals are equal amounts of chalcopyrite and hematite with rare covellite.

Pyrite occurs primarily as massive grains, and rarely as cubes. The center of the vein is highly brecciated and filled by late calcite. Replacement of pyrite by chalcopyrite is along fractures in the center of the vein, and also at the periphery of the vein, sometimes appearing to be along cleavage. Hematite is restricted to the periphery of the pyrite vein. There is no evidence for framboidal pyrite.

### MP2001-52

Sample is from pyrite zone, and is cut from a porphyritic green basalt. Pyrite is found mainly encrusting the edges of basalt, growing out into calcite. Pyrite comprises >99% of the sulphides and oxides in this sample. The remainder is chalcopyrite and specular hematite, which rarely occur as small blebs and laths respectively, or as inclusions in pyrite.

Pyrite occurs relatively large (avg. 25 $\mu\text{m}$ ) xenoblastic cubes, which commonly cluster in agglomerates. Massive pyrite is also common, occurring in amorphous masses. These masses, when being replaced by calcite, often reveal fine colloform textures, much as the above MP2001-50. Often these colloform structures are inferred from minute inclusion patterns that define the outline of a colloform or spheroidal structure. Rarely, pyrite appears pseudomorphing laths or plates of hematite or Fe-Ti-oxides.

### **MP2001-60**

This sample is cut from a section of net-like anastomosing pyrite that has been cut and highly replaced by late calcite. The sample is ~100% pyrite.

Pyrite occurs in two main textures – as cubes and as aggregated grains or cubes, which tend to be massive as a whole. Cubic pyrite is generally subidioblastic, perfect preservation is rare. Edges of cubes are rounded or smooth to embayed. Inclusions in cubic pyrite are not widespread, and where they occur there does not appear to be a preferred distribution. Cubic pyrite itself does not have any preferred distribution either.

The second mode of pyrite occurrence is as agglomerated or massive pyrite. The edges of the agglomerates are usually smooth to embayed, almost myrmekitic, and they are surrounded by a matrix of calcite. Colloform textures are present, often inferred from minute inclusions patterns, or poorly exposed by partial calcite replacement, which mimic those of MP2001-50, where there is clear evidence for colloform structures.

### **MP2001-61**

This sample is a <50µm pyrite vein, cut from porphyritic green basalt.

Pyrite comprises >99%, with the remainder being specular hematite or chalcopyrite. Pyrite occurs chiefly as subidioblastic aggregated grains. The vein in this sample is bordered on one side by calcite, and the other by basalt. The vein may in fact be a growth from the basalt side into the calcite – the calcite-bounded side is idioblastic, with sharp grain edges. At the edge of the idioblastic grains, specular hematite is often noted rimming pyrite. Disseminated pyrite in the basalt is prevalent, occurring as <5µm skeletal grains, which appear to be controlled by host rock porosity (?).

### **MP2001-62**

This sample is cut from a fine-grained brown rhyodacite. Mineralization is in the form of anastomosing networks of pyrite surrounding large grains of calcite. The sample is 100% pyrite, of which approximately 95% is as idioblastic cubes. It also occurs as finely disseminated cubes throughout the sample. The size of cubes ranges from <1µm to 20µm. There appears to be two different generations of cubes, with the dominantly idioblastic cubes, which are suspended in the calcite matrix, being younger, and more corroded or xenoblastic cubes being older. The so-called older cubes have a higher concentration of inclusions. There appears to have been some degree of flowage in the younger idioblastic cubes, or another mechanism that has concentrated cubes.

### **MP2001-67**

This sample is cut from a weakly albitized rhyodacite. Mineralization occurs as an approximately 1mm wide vein of pyrite. Pyrite also occurs in smaller veinlets and as finely disseminated blebs throughout the sample.

The primary texture of pyrite is as aggregates of recrystallized grains. There is often an intergranular film of calcite or some other unknown non-sulphide. Most of the aggregated grains have a spheroidal shape, and cubic pyrite is uncommon, occurring mainly at the edge of the vein. There are rarely inclusions in the pyrite, although there is commonly a large intragranular space that is calcite filled. Mild brecciation occurs parallel to the length of the vein.

### **MP2001-68**

This sample is cut from a weakly albitized rhyodacite. Mineralization occurs as an approximately 1mm wide vein of pyrite.

The sample is ~99% pyrite, the remainder being chalcopyrite and hematite.

Pyrite occurs as primarily two morphologies, cubes and also, more commonly, as aggregates of grains or cubes. Pyrite also occurs as finely disseminated cubes in the rhyodacite. This sample is very similar to MP2001-67, except there is a much higher

incidence of inclusions in the cubes and agglomerated cubes. Where grains have aggregated, the intergranular film often outlines a generally spherical shape. Inclusion patterns are also often in spheroidal

#### **MP2001-69**

This sample is cut from a felsic tuff that is strongly altered (albite > potassic). Mineralization occurs only as blebs of pyrite, and fine disseminations randomly distributed throughout the sample.

The large blebs (<200µm) have smoothly rounded edges, often concave into the grain. There are inclusions in these blebs, which have an amoeba shape (Figure X). The pyrite is very homogenous, with no irregularities. Hematite is common in the matrix, as specular hematite, and sometimes occurs as inclusions in the large pyrite blebs.

#### **MP2001-70A**

This sample is cut from a strongly altered (potassic > albitic) tuff as well. Pyrite occurs as discrete blebs and as finely disseminated grains in the host rock. This sample is very similar to MP2001-69, except that there is a higher frequency of small, non-amoeboid shaped inclusions. Pyrite is homogenous, and edges are smooth, often concave into the grains.

#### **MP2001-70B**

This sample is cut from a high-grade chalcopyrite vein. The sample is >99% chalcopyrite with the remainder as specular hematite.

Chalcopyrite is completely homogenous, exhibiting no textures, except where rare inclusions occur. These inclusions are filled with calcite or calcite and specularite, which grows into the cavities as laths or plates. The left side of the sample has some heterogeneity, marked by highly irregular bands of alternating calcite and chalcopyrite. There does not appear to be any framboidal characteristics, as is often noted in chalcopyrite of the Valdivia Sur orebody cluster.

#### **MP2001-76**

This sample is cut from a zone of aggregated spherical grains that have been cut or infilled by late calcite. In hand sample these spherical grains are clearly visible, clumping together. Pyrite comprises approximately 95% of the mineralization, with chalcopyrite forming the final 5%. Pyrite occurs in two main morphologies, cubes and aggregates of grains or cubes. Cubic pyrite occurs in a wide range of sizes, from <1µm to 20µm. Smaller cubes are homogenous, containing little to no inclusions, while larger cubes, and aggregates of cubes exhibited a large amount of inclusions. There is no preferred distribution of cubes in the sample.

The more dominant morphology of pyrite is as recrystallized aggregates of grains and cubes. These aggregates are amorphous, and generally the edges are highly irregular, due to their composite nature. There is a high degree of inclusions in the aggregates, and these aggregates display a small degree of regularity, often outlining a spherical shape. This is possible a function of the aggregate nature of the masses, reflecting the outline of a grain that has been incorporated into the aggregate. There are often intergranular films of calcite separating the aggregated grains. The edge of the aggregates always displays a fresh overgrowth, which is inclusions free, and likely the result of a later phase of pyrite mineralization



## **Appendix D**

Microprobe Raw Data  
Categorized by Mineral

**Explanation of Point type codes:**

fr: point is from the vicinity of a pyrite framboid, or a framboidal zone

vn: point is from a small veinlet in the slide

cb: point comes from a cube of pyrite, or an aggregate of cubes, either fresh or poikiloblastic

ms: These points come from texturally massive or homogenous sulphides

lg: point has come from one of the large grains of pyrite or other sulphides being replaced

sg: points come from small grains, typically those like pyrite in Figure 5.2, grains suspended in matrix of replacement sulphide

rc: points are from shell structures surrounding framboids, or from the rings of pyrite in colloform pyrite

cr: where transects across pyrite cubes or other large grains, cr represents the core or mid-point of the transect

ot: a non-classified texture

t: this is used to represent trace amounts that are likely not significant in terms of probe analytical measurement errors. Generally at 0.1%, or above probe detection limits

**Table D.1 Microprobe data for Pyrite analysis**

Real sample	Cu	Fe	As	S	Ni	Mn	Co	Pb	Mo	Ti	Total	type of point
MP2001-52.1		46.640		53.710				0.909	t		101.429	rc
MP2001-52.2		46.092	t	54.245		0.520	0.155	0.843	t		101.871	rc
MP2001-52.3		46.722	t	54.005	t		0.175	1.083	t		102.134	cr
MP2001-52.4		46.374	t	54.306			0.166	1.756	t		102.618	cr
MP2001-52.5		46.971		53.563			0.147	0.289	t		101.047	cr/rc
MP2001-52.6		46.350		54.182			0.208	1.293	t		102.098	cr/rc
MP2001-52.7	t	47.171		54.235				0.929	t		102.562	rc
MP2001-52.8		46.441		54.518		t	0.281	1.296	t		102.747	rc
MP2001-52.9	t	45.136	t	51.189		t	0.095		1.246		98.143	ot - psuedo
MP2001-52.10		45.222	t	50.367			0.212		1.648		97.711	ot - psuedo
MP2001-52.11		46.270		54.401	0.0959			0.537	t		101.479	ot - psuedo
MP2001-52.12		46.110	0.481	53.701				0.987	t		101.596	cbi
MP2001-52.13		46.003		52.119			0.355	0.872	t		99.378	cbi
MP2001-52.16		46.493		54.499		0.373	0.206	1.226	t		102.862	cbi/fr
MP2001-52.17		46.966		55.538				1.804	t		104.444	cbi/fr
MP2001-62.1		47.162		54.645			0.251	1.223	t		103.440	cbi
MP2001-62.2		47.677	t	53.835			0.257	0.768	t		102.777	cbi
MP2001-62.3		47.089		54.811				0.464	t		102.387	ms
MP2001-62.5		46.487		54.407			0.314	0.687	t		101.985	cbi
MP2001-62.6		47.052	t	54.229	0.136			0.384	t		102.029	cbi
MP2001-62.7		46.687		54.455				0.315	t		101.544	cbi/cr

MP2001-62.8		46.895		54.527			0.348	0.321	t		102.118	ms/cb
MP2001-62.9		46.740		53.782			0.292	0.583	t		101.458	ms/cb
MP2001-62.10		46.639	t	55.110	0.112		0.094	1.531	t		103.690	ms/cb
PC-04.5	t	44.792	2.223	51.492		0.311		0.000	t		99.350	fr
PC-04.8	t	44.662	2.669	51.734		0.299		0.443	t		100.315	fr/rc
PC-02A.2	0.552	45.875	1.341	53.021	t		0.244	0.285	t		101.417	fr/ms
PC-02A.3		45.382	1.618	52.201	0.161	t	0.151	0.609	t		100.248	fr/ms
PC-02A.4		46.360	0.314	53.291	0.063		0.375	0.228	t		100.789	fr/ms
PC-02A.5	0.816	45.141	0.664	51.988			0.313	0.732	t		99.730	fr/ms
PC-02A.6	1.440	44.933	1.136	52.235			0.220	0.712	t		100.719	fr/ms
PC-02A.7	1.000	44.815	1.133	50.840			0.386		0.588		98.761	fr/ms
PC-02A.8		45.587	1.016	53.149		0.641					100.468	fr/ms
MP2001-68.2		48.440		55.644	0.245		t	0.110			104.748	cb
MP2001-68.3		48.225		55.637			0.135	1.092			105.261	cb/cr
MP2001-68.4		48.348		55.680	t		0.325	0.236			104.676	cb
MP2001-68.5		48.726		55.321			0.163	0.000	0.474		104.849	cr/ms
MP2001-68.6		48.750		55.982			0.170	0.354			105.340	cb/ms
MP2001-68.7		48.694		55.723			0.202	1.130			105.749	ms/cr
MP2001-51.3		48.529		55.337	0.164		0.241	0.487			104.757	cb
MP2001-67.1		48.183		55.447	0.128		0.154	0.152			104.070	ms
MP2001-67.2		47.904		55.131							103.179	ms
MP2001-67.3		47.945		55.025				0.853			103.894	ot
MP2001-67.5		48.174	0.385	56.151			0.276	0.997		0.238	106.221	ot
MP2001-67.6		47.182	0.368	55.864				0.373		0.728	104.671	ot
MP2001-70A.1		48.111		54.889			0.363	0.486			103.890	sg
MP2001-69.1		48.593		55.816			0.198	0.000			104.687	ms/ms

MP2001-74.1		50.044		58.072			0.152	1.223			109.614	cb
MP2001-74.2		49.581	t	58.081			0.329	1.453			109.800	cb
MP2001-74.3		49.802		58.936			0.179	1.164			110.199	cb/cr
MP2001-74.4		49.856	0.556	57.165				0.000			107.846	cb/ms
MP2001-74.5		49.990	0.336	58.217			0.109	1.315			110.214	cb/ms
MP2001-74.6		50.081		58.921			0.158	1.688			110.866	cr/ms
MP2001-74.7		49.308		56.258			0.263	0.019	0.858		106.717	cr/ms
MP2001-74.8		49.892		58.300	t		0.201	0.928			109.490	cb-zoned
MP2001-74.9		50.235		58.771	0.137			2.332			111.511	cb-zoned
MP2001-76.1		49.363	t	58.516	0.154		0.053	1.739			109.977	cb-zoned
MP2001-76.2		49.523	t	58.301			0.260	2.674			110.908	cb/cr
MP2001-76.3		49.647		58.903			0.205	1.787			110.626	cb/cr
MP2001-61.2		50.514		60.046				2.935			113.748	vn
MP2001-61.3		47.232	0.320	53.811			0.213		0.221		101.808	vn
MP2001-60.1		48.711		55.419		t	0.239				104.596	ms
MP2001-60.2		48.610		55.310		0.215	0.471				104.666	ms
MP2001-60.3		49.328		56.862			0.372				106.691	ms
MP2001-60.4		48.818		55.623		0.204	0.204				104.849	ms/cr
MP2001-60.5		48.868		55.428			0.279				104.757	ms/cr
MP2001-60.6		48.688		56.214		0.666					105.669	ms/cr
MP2001-60.7		45.304		50.624			0.169		0.864		97.043	ms
MP2001-60.8		46.095		51.569			0.198		1.376		99.269	ms
PC-02A		46.62		53.29				0.71			100.62	sg
PC-02A		46.89	0.55	54.09		0.32		0.87			102.71	sg
PC-02A	2.22	45.94		52.77		t		1.49			102.42	fr/cr
PC-02A	3.25	44.03	1.60	50.24				0.57			99.69	fr/cr



**Table D.2: Chalcopyrite data**

Chalcopyrite													
Point	Real sample	Cu	Fe	As	S	Ni	Mn	Co	Pb	Mo	Ti	Total	point type
15	MP2001-52.14	33.297	31.613		34.930				0.615			100.638	cb
	PC-04.1	25.078	35.717	0.639	41.415				0.273			103.284	rc
	PC-04.2	26.528	34.807	0.553	40.732		t	0.242	1.046			104.066	rc
	PC-04.3	28.144	34.387	0.417	38.918				0.060	0.438		102.370	cr/fr
	PC-04.4	28.607	33.899	0.545	39.812		t		0.883			103.962	cr/fr
	PC-04.6	30.761	31.588		36.588				0.219			99.205	rc
	PC-04.7	33.696	30.607		34.717			0.248	0.640			99.916	cr/fr
	MP2001-70B.1	37.915	32.550		36.796				0.067	0.698		108.087	ms
	MP2001-61.4	36.066	31.495		35.227			t	0.550			103.497	sg
3.00	PC-02A	34.20	30.64		34.67		t		1.32			100.96	ms
4.00	PC-02A	33.95	31.01		34.60				0.93			100.6	ms
5.00	PC-02A	34.06	30.44	t	35.47				1.80			101.97	fr/cr
11.00	PC-02A	35.18	30.35		34.89				0.87			101.31	fr/cr
13.00	PC-02A	34.20	30.30	t	35.01				0.87			100.58	rc/fr
18.00	PC-02A	34.14	30.52		35.19				1.05			100.9	cr/fr
19.00	PC-02A	34.49	30.49		34.28				0.00	0.23		99.72	sg
20.00	PC-02A	33.60	31.24		35.33				0.96			101.24	sg
21.00	PC-02A	34.48	29.57		34.80				1.59			100.61	sg
2.00	PC-04	34.14	30.87	t	34.90				0.04			100.2692308	ms
6.00	PC-04	33.10	29.78		34.05				1.04			98.22865385	vn/fr
17.00	PC-04	34.11	29.94	t	34.22				1.16			99.94461538	fr/cr
25.00	PC-03	33.46	30.45		34.52		t	0.22	1.04			100.0481731	fr/cr
30.00	PC-03	35.29	30.34		35.04				1.13			102.2643269	ot
32.00	PC-03	34.09	30.88		35.68				1.82			102.9675	ot
42.00	PC-01	33.31	28.92		32.80		t		1.24			96.86961538	ms

**Table D.3: Bornite microprobe data**

<b>Bornite</b>												
<b>Point</b>	<b>Sample</b>	<b>Cu</b>	<b>Fe</b>	<b>As</b>	<b>S</b>	<b>Ni</b>	<b>Mn</b>	<b>Co</b>	<b>Pb</b>	<b>Mo</b>	<b>Total</b>	<b>type of point</b>
3.00	PC-04	59.59	11.84		24.46						96.65144	sg
13.00	PC-04	60.00	11.56		25.90				0.14		97.63308	lg near fr
14.00	PC-04	61.20	11.42		26.00				1.30		100.5997	vn
16.00	PC-04	60.16	11.88		25.68				1.43		99.55981	ms near py
18.00	PC-04	59.49	12.14		25.71				0.69		98.33365	fr
20.00	PC-04	53.89	15.24	t	27.69		t		0.86		98.37635	fr
21.00	PC-04	62.60	11.35		25.17				0.74		100.2882	fr
27.00	PC-03	61.62	11.61		25.79				1.28		100.6265	sg (surrounded by py)
29.00	PC-03	62.52	12.24		25.72				1.19		101.7947	ms/fr
38.00	PC-01	58.99	10.81		23.16				0.11	0.57	93.98404	fr
40.00	PC-01	58.30	12.40	t	25.11				0.38		96.86183	fr
41.00	PC-01	60.23	11.14		24.14				0.42		96.12317	ms



**Table D.4: All values with high levels of As**

<b>High As</b>												
<b>Real sample</b>	<b>Cu</b>	<b>Fe</b>	<b>As</b>	<b>S</b>	<b>Ni</b>	<b>Mn</b>	<b>Co</b>	<b>Pb</b>	<b>Mo</b>	<b>Ti</b>	<b>Total</b>	<b>type of point</b>
MP2001-52.12		46.110	0.481	53.701				0.987	t		101.596	cbi
PC-04.5	t	44.792	2.223	51.492		0.311		0.000	t		99.350	fr
PC-04.8	t	44.662	2.669	51.734		0.299		0.443	t		100.315	fr/rc
PC-02A.2	0.552	45.875	1.341	53.021	t		0.244	0.285	t		101.417	fr/ms
PC-02A.3		45.382	1.618	52.201	0.161	t	0.151	0.609	t		100.248	fr/ms
PC-02A.4		46.360	0.314	53.291	0.063		0.375	0.228	t		100.789	fr/ms
PC-02A.5	0.816	45.141	0.664	51.988			0.313	0.732	t		99.730	fr/ms
PC-02A.6	1.440	44.933	1.136	52.235			0.220	0.712	t		100.719	fr/ms
PC-02A.7	1.000	44.815	1.133	50.840			0.386		0.588		98.761	fr/ms
PC-02A.8		45.587	1.016	53.149		0.641					100.468	fr/ms
MP2001-67.5		48.174	0.385	56.151			0.276	0.997		0.238	106.221	ot
MP2001-67.6		47.182	0.368	55.864				0.373		0.728	104.671	ot
MP2001-74.4		49.856	0.556	57.165				0.000			107.846	cb/ms - poik
MP2001-74.5		49.990	0.336	58.217			0.109	1.315			110.214	cb/ms - poik
MP2001-61.3		47.232	0.320	53.811			0.213		0.221		101.808	vn
PC-02A		46.89	0.55	54.09		0.32		0.87			102.71	sg
PC-02A	3.25	44.03	1.60	50.24				0.57			99.69	fr/cr
PC-02A	0.99	45.48	1.38	52.54				1.59			101.98	fr/cr
PC-02A		46.71	0.62	52.89				1.11			101.33	cb
PC-02A		46.15	0.60	53.81		t		2.07			102.63	cb
PC-02A		46.42	0.37	53.79		t		1.83			102.41	cb
PC-02A	1.15	44.70	1.10	50.81				0.97			98.74	cb
PC-02A	1.22	44.39	2.78	51.47		t		0.28			100.14	cb
PC-02A		45.01	0.43	54.04		1.97	0.11	0.32			101.89	ms

PC-02A		44.71	0.43	53.83		1.96		1.09			102.03	ms
PC-04	0.89	45.29	0.52	51.37			t	0.00			98.61826923	rc/fr
PC-04	1.18	44.90	0.55	51.50		t	0.28	2.08			101.2446154	rc/fr
PC-04		45.31	0.99	52.52		0.32	0.15	0.98			100.7861538	lg
PC-03		45.80	1.24	52.56		t	0.24	0.00			100.6451923	rc/fr
PC-03		46.57	0.96	53.51		t	0.22	1.89			103.8274038	rc/fr
PC-03	8.17	42.61	0.23	48.33				0.60			100.1780769	fr
PC-03		47.53	0.39	53.21			0.12				101.6301923	cb
PC-01	0.69	43.64	2.42	50.01		t		0.31			97.36673077	ot

## References

- Bassi, H.G.L., 1988. Evolucion en el conocimiento geologico del yacimiento cuprifero disminado El Soldado, 5a Region, Chile, Actas, V Congreso Geologico Chileno, v3, p G53-G70
- Bateman, J.A., 1995. Mineralogical and Geochemical traits of the Egret Member Shale, Jeanne d'Arc Basin, Offshore Newfoundland, Canada. Unpublished MSc. Thesis, Dalhousie University, Halifax, Nova Scotia.
- Bates, R.L. & Jackson, J.A., 1984. Dictionary of Geological Terms, 3<sup>rd</sup> Ed. Anchor Books, New York
- Best, M.G. & Christiansen, E.H., 2001. Igneous Petrology. Blackwell Science
- Berner, R.A., 1970. Sedimentary pyrite formation. American Journal of Science, **268**: 1-23
- Berner, R.A., and Raiswell, R., 1993. Burial of organic carbon and pyrite sulphur in sediments over Phanerozoic time: a new theory. Geochimica et Cosmochimica Acta, **47**: 855-862
- Boric, R., 1997. Nuevo antecedentes sobre el modelo geologico del yacimiento de cobre, El Soldado, Chile Central, Cong. Geol. Chile, Antofagasta, p. 862-866

Boric, R., Holmgren, C., Wilson, N.S.F., and Zentilli, M., 2002 (in press). The geology of the El Soldado manto type Cu (Ag) deposit, Central Chile. *In* Porter, T.M. (Ed), - Hydrothermal Iron Oxide Copper-Gold & Related Deposits: A Global Perspective, volume 2, *PGC Publishing, Adelaide*.

Boric,R., 2002. Geology, mineral zoning, and lithochemistry of the El Soldado manto type copper deposit, Chile. Unpublished M.Sc. Thesis, Dalhousie Univ., Halifax, Canada, ca. 200p.

Craig, J.R. and Vaughan, D.J., 1994. Ore microscopy and Ore Petrography (2<sup>nd</sup> Ed). John Wiley & Sons, Inc. New york

Deer, W.A., Howie, R.A., Zussman, J., 1992. An Introduction to the Rock Forming Minerals. Longman Group Limited, London

Gonzalez, F. and Holmgren, C. 1993. Características mineralógicas de la zona de oxidación y su implicancia en la recuperación de sulfuros en el yacimiento El Soldado, *Congreso Internacional de Ingeniería de Minas*, III Región, Copiapo, Chile, Actas, pp. 270-279.

Fontboté, L., 1990, Strata-bound ore deposits in the Andes: A review and classification according to their geotectonic setting, in Fontboté, L., Amstutz, G.C., Cardozo, M., Cedillo, e., and Frutos, J. (eds), *stratabound Ore Deposits in the Andes*, Springer-Verlag, 79-110p.

Holmgren, C., 1987, Antecedentes para un modelo genético del yacimiento El Soldado, V Región de Valparaiso, Chile: *Revista Geolog. De Chile*, v. 30, p 13-18

Kashefi, K., Tor, J.M., Nevin, K.P., and Lovley, D.R., 2001. Reductive precipitation of Gold by dissimilatory Fe(III)-reducing bacteria and archaea.. *Applied and Environmental Microbiology*, **67**: 3275-3279

Manning, D.A.C. & Gize, A.P., 1993. *Organic Geochemistry*. Ed by Engle, H.L. & Macko, S.A. New York p547-563

Martin, W., 1981. Distribucion de la Mineralizacion en el Yacimiento Cuprifero El Soldado, V Region. *Unpublished B. Sc. Thesis*, Departamento de Geologia y Geofisica, Universidad de Chile, Santiago, 92 p.

Ponce, R., 2001. Geologia, mineralizacion y distribucion de elementos trazas en el sector Filo, mina El Soldado, V Region. *Unpublished B.Sc. thesis*, Depto. de Geologia, Universidad de Chile, Santiago, 104 p

Nielson, H., 1979. *Lectures in Isotope Geology*. Ed. Jäger E. and Hunziker J.C. Springer-Verlag. New York. p283-312.

North, F.K., 1985. *Petroleum Geology*. Allen and Urwin, Boston, p607

Otswald, J., and England, B.M., 1977. Notes on framboidal pyrite from Allandale New South Wales, Australia. *Mineralium Deposita*, **12**: 111-116

Otswald, J., and England, B.M., 1979. The relationship between euhedral and framboidal pyrite in base-metal sulphide ores. *Mineralogical Magazine*, **43**: 297-300

Parnell, J., 1988. Metal enrichments in solid bitumen: a review. *Mineralium Deposita*, **23**: 191-199.

Ramdohr, P., 1980. *The Ore Minerals and Their Intergrowths* Second Edition. Pergamon Press.

Rickard, D.T., 1970. The origin of framboids. *Lithos*, **3**: 269-293

Robinson, D., and Bevins, R.E., 1989, Diasthermal metamorphism at very low grades and possible high grade analogues, *Earth and Planetary Science Letters*, **70**: 151-158

Ruiz, C. Aguilar, A., Egert, E., Espinoza, W., Peebles, F., Queada, R., and Serrani, M., 1971. Yacimientos chilenos estratiformes de sulfuros de cobre, *Revista Minerale*, **26**: 3-13

Sassano, G.P., and Schrijver, K., 1989. Framboidal pyrite: early diagenetic, late-diagenetic, and hydrothermal occurrences from the Acton Vale Quarry, Cambro-Ordovician, Quebec. *American Journal of Science*, **289**: 167-179

Sato, T., 1984. Manto-type copper deposits of Chile, in: *Research on calc-alkaline magmatism and related mineralization in Chile: Report of research and development cooperation ITIT project no. 7911*; Geological Survey of Japan: March 1984, p52-72.

Sawlowicz, Z., 1992. Pyrite framboids and their development: a new conceptual mechanism. *Geologische Rundschau*, **82**: 148-156

Sillitoe, R.H., 1990, *Copper deposits and Andean evolution: Earth Science Serials*, Circum-Pacific Council Energy Mineral Resource, v.11, 285-311.

Sillitoe, R.H., 1992, Gold and Copper Metallogeny of the Central Andes – Past, Present and Future Exploration Objectives, *Economic Geology*, v.87, 2205-2216p.

Westra, G., 1988, La importancia del metamorfismo de carga en la formación de yacimientos de cobre tipo manto: Reprint, Keynote Address, V Chilean Geol. Cong., Santiago, 18p.

Wilkin, R.T., and Barnes, H.L., 1997a. Formation processes of framboidal pyrite. *Geochimica et Cosmochimica Acta*, **61**: 323-339

Wilkin, R.T., and Barnes, H.L., 1996. Pyrite formation by reactions of iron monosulphides with dissolved inorganic and organic sulphur species. *Geochimica et Cosmochimica Acta*, **60**: 4167-4179

Wilson, N.S.F., 1998. The role of petroleum in the formation of the El Soldado copper deposit, Chile: Hydrothermal replacement of a biodegraded petroleum reservoir. P1-418.

Wilson, N.S.F., and Zentilli, M. 1999. The role of organic matter in the genesis of the El Soldado volcanic-hosted manto-type Cu deposit, Chile. *Economic Geology*, **94**: 1115

Wilson, N.S.F., 1999. Organic petrology, chemical composition, and reflectance of pyrobitumen from the El Soldado Cu deposit, Chile. *International Journal of Coal Geology*. **43**: 53-82

Wilson, N.S.F., Zentilli, M. and Spiro, B., 2001. The essential role of bacteria and petroleum in the formation of the volcanic-hosted El Soldado manto-type Cu deposit, Chile: a sulphur, carbon, oxygen, and strontium isotope study. Submitted.

Winchester J.A. and Floyd, P.A., 1977. Geochemical discrimination of different magma series and their differentiation products using immobile elements. *Chemical Geology*, v. 20, pp. 325-343.

Zentilli, M., Munizaga, F., Graves, M.C., Boric, R., Wilson, N.S.F., Mukhopadhyay, P.K., and Snowdon, L.R., 1997, Hydrocarbon involvement in the genesis of Ore Deposits: An Example in Cretaceous Strata-bound (Manto-Type) Copper Deposits of Central Chile, *International Geology review*, v39, 1-21p.

Mineral Gallery [www.theimage.com](http://www.theimage.com) (no update date)

Retrieved on March 22, 2002 from,

<http://www.theimage.com/mineral/pyrite/pyrite.html>

Amethyst Gallery Inc. (1999). The Mineral Marcasite

Retrieved on March 22, 2002 from,

<http://mineral.galleries.com/minerals/sulfides/marcasit/marcasit.htm>

Pyrite (no author or update date).

Retrieved on March 22, 2002 from,

<http://www.chem.ox.ac.uk/mom/pyrite/pyrite.html>



# Patrick G. Collins

106 Crichton Avenue  
Dartmouth, Nova Scotia  
B3A 3R5  
902.466.3791  
pat\_collins013@yahoo.ca  
September 10, 2002

## Education

Dalhousie University, Halifax, Nova Scotia, 1998-2003

### **Bachelor of Science, Honours, Earth Science**

Selected classes:

- Structural Geology (B+) • Honours Field Camp (A+)
- Metamorphic Petrology (A) • Computing Field Camp (A)
- Quaternary Geology (A) • Igneous Petrology (A-)
- Tectonics (B+) • Advanced Min. Deposits (on track for A)
- Applied Geology/Mineralogy (A) Thesis Defense (A)

### **High School**

Dartmouth High School, 1994-1996

## Skills

### **Field Skills**

- Geological mapping, sedimentary, metamorphic, igneous rocks.
- Developmental and operational mapping underground
- Geophysical probing/surveying of blasthole operations (Craig Mine)
- Air photos, compass and pace traversing; FIELDLOG recording
- Field trips in Nova Scotia, New Brunswick and Ontario, including underground visit to Brunswick #12 mine, Strathcona/Fraser mine, Thayler-Lindsley mine
- Accurate note taking; Report writing
- Acute observational skills
- Drivers license since 1995; clean driving record
- Mechanical repairs on bicycles

### **Computer Skills**

- Datamine: familiar with wireframe modeling and block modeling
- CAMP/Silver Screen mapping/modeling package
- Century Systems Suite: Borehole Manager, DH Logger
- Windows OS, Mac OS (all versions), Microsoft Word, Excel, Access
- Experienced with AutoCAD, and FIELDLOG in creating working geological maps
- Familiar with IDRISI, Arcview and CARIS software with respect to basic GIS

### **Lab Skills**

- Petrographic microscope skills for sedimentary, igneous, and metamorphic rocks; transmitted and reflected light (ore microscopy)
- Capable of operating JEOL 733 and JEOL JXA 8200 microprobes
- Core logging (lithology, RQD, structure, mineralization estimates)
- Sampling: processing samples for assaying
- XRF, XRD, heavy mineral separation, INAA
- Basic experience with seismic-record interpretation

## Employment History

**Fission Track Laboratory, Dalhousie University** Septmeber 9, 2002 – present

Supervisor: Dr. Marcos Zentilli, Lab Director

Position: Research Assistant. Responsibilities include database cataloguing, microscopy and electron microprobe based research, assistance with manuscript preparation

**Falconbridge, Mines/Mill Business Unit, Sudbury, Ontario** May 6, 2002 – August 30, 2002

Supervisor: Steve Falconer, Mine Geologist, Craig Mine, Onaping, Ontario

Position: Geologist I. Responsibilities included diamond drilling data management, logging operations core, sampling core, due diligence (DDH log validation), geophysical surveying, map digitizing, and 3D modeling

**Dalhousie University, Dept. of Earth Sciences:** June 2000

Supervisor: Dr. D.B. Clarke Telephone: 902 494 2358

Developing experiments used to create an analogue mechanical model for shearing in a partly crystallized granite pluton

**Dio Mio Gelato Deserts Café:** June 1996 - September 1, 2000; September 2001-February 2002

Walter Forsythe, Owner, 902.492.3467

Position: Gelato production, and baker

## Volunteer Experience

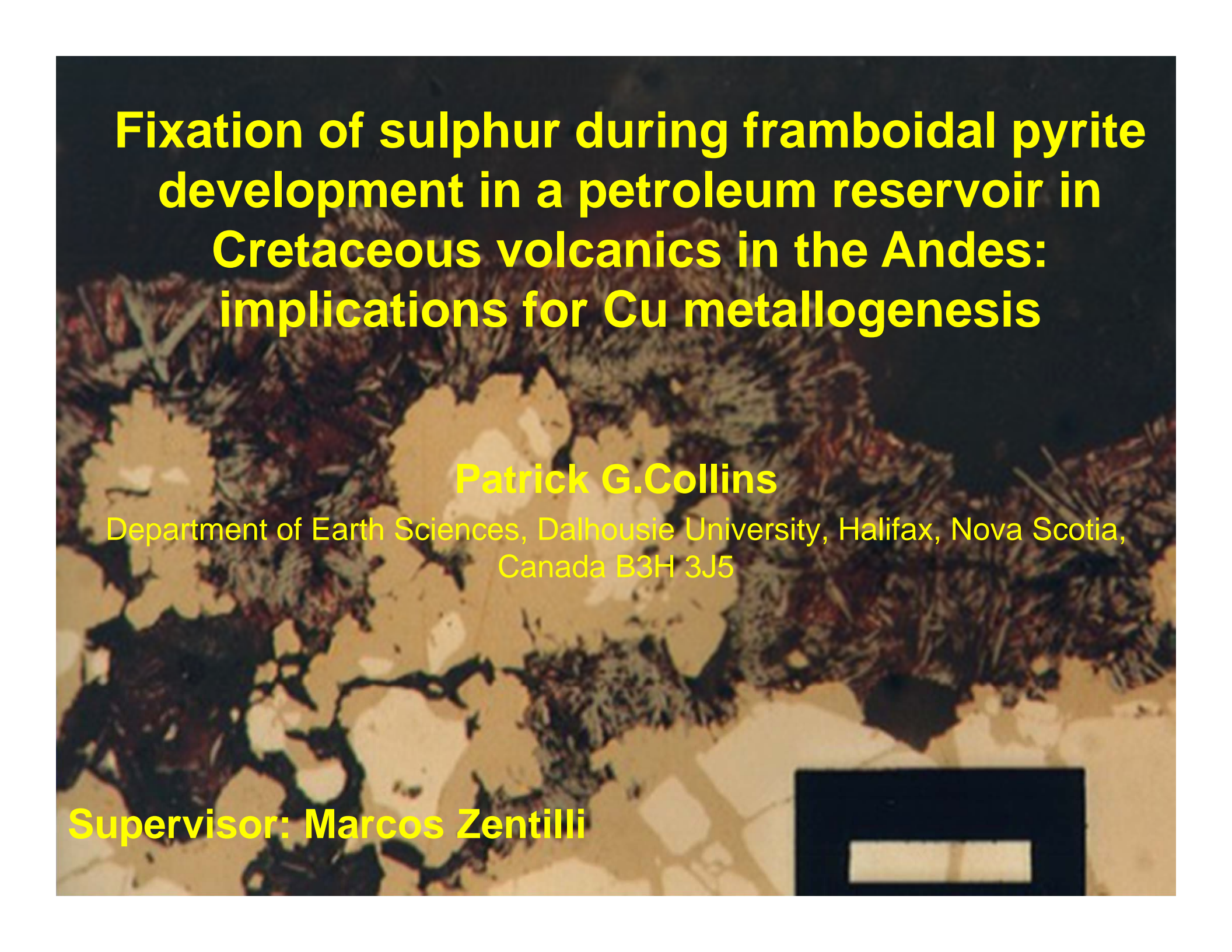
- **Canada Games Cycling Team:** I am a NCCP (National Coaching Certification Program) certified Level Two Mountain Bike Technical coach.
- **AUGC 2000 (Atlantic Universities Geologic Conference):** During this conference I volunteered my time to help the organizers with various tasks including transportation of participants, as well as organization of meals

## Reports and Presentations

- **AUGC 2002 oral presentation:** Diagenetic pyrite in a petroleum reservoir in Cretaceous volcanics in the Andes replaced by hydrothermal copper
- **BSc Honours Thesis: September 10, 2002:** Fixation of sulphur during framboidal pyrite development in a petroleum reservoir in Cretaceous volcanics in the Andes: implications for Cu metallogenesis
- **Thesis Defense, Halifax, NS, April, 2002:** Oral defense of my Honours thesis
- **Atlantic Geological Society Conference, Antigonish, NS, February 2002:** Presented data from my Honours project
- **AUGC, Antigonish, NS, 2001:** poster presentation on El Soldado Cu deposit

## Distinctions, Certifications and other Activities

- Frank Shea Memorial Award: Best Economic Geology paper at AUGC 2002
- Dean's List, Faculty of Science, 2002
- WHIMIS certification as well as courses for mine site safety: surface and underground
- Nova Scotia valid Class 5 drivers license
- PADI Open Water SCUBA diving certification
- Dalhousie Dawson Geology Club Member, 1999- present
- Certified Nova Scotia Prospector (License # 1066) Sept. 2000-present
- Society of Economic Geologists, Student Chapter, Dalhousie University, October 2000 - present
- Mountain Bike racing: I have raced mountain bikes since 1993, and currently race at a semi-professional level. In 2000, my last year of fully dedicated racing, I was ranked 2<sup>nd</sup> overall in Atlantic Canada, and was 9<sup>th</sup> in Canada, for <23 yr. old, professional racers
- Swimming - I enjoy swimming, and swam with the Dartmouth Crusaders Swim Club from 1989-1996
- Canoe safety certification, experience with small motorized water craft



**Fixation of sulphur during framboidal pyrite  
development in a petroleum reservoir in  
Cretaceous volcanics in the Andes:  
implications for Cu metallogenesis**

**Patrick G. Collins**

Department of Earth Sciences, Dalhousie University, Halifax, Nova Scotia,  
Canada B3H 3J5

**Supervisor: Marcos Zentilli**

# Acknowledgements

Thanks must be given to my advisor, Marcos Zentilli; Ricardo Boric (Mine geologist at El Soldado); Nick Wilson, GSC; Sandy Grist (FTL); Bob MacKay; special thanks to Gordon Brown for the excellent polished sections



Morro open  
pit

100's of kms  
underground

adit

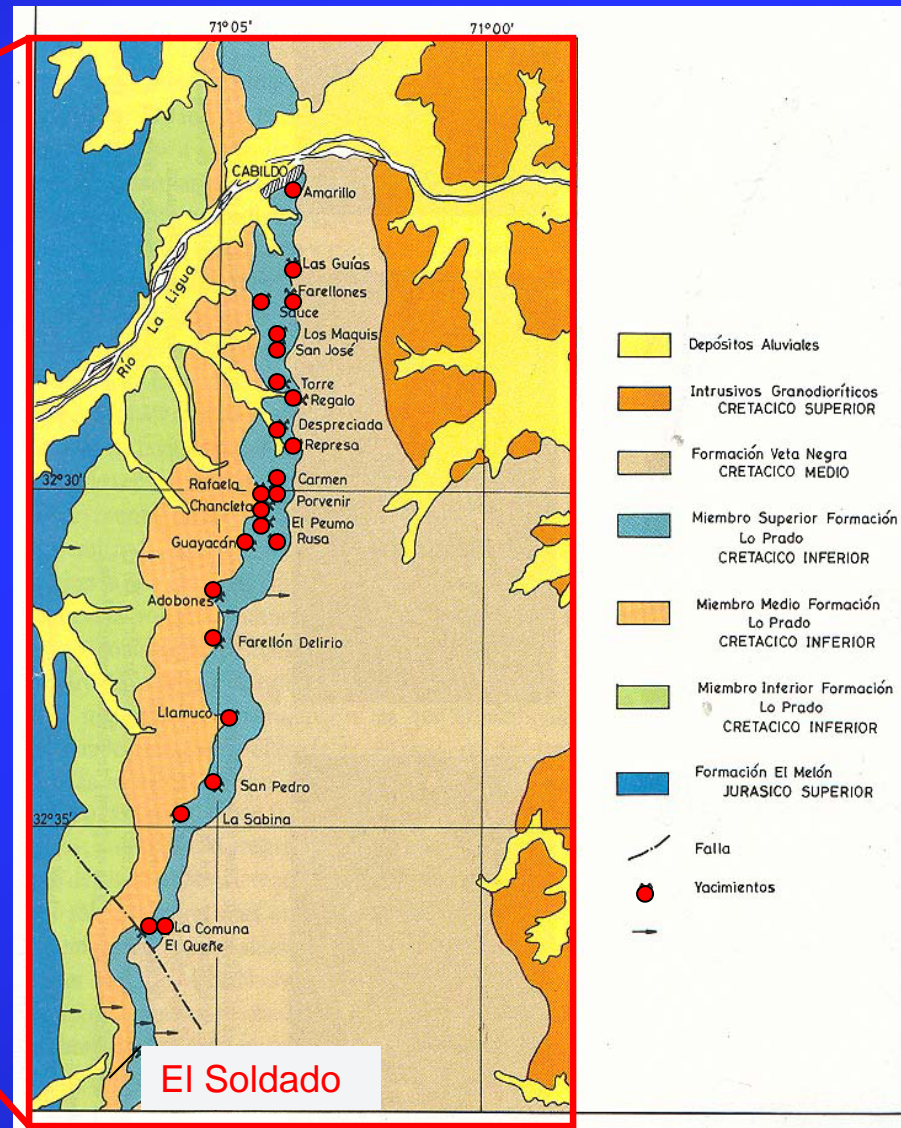
waste dump

mill/concentrator

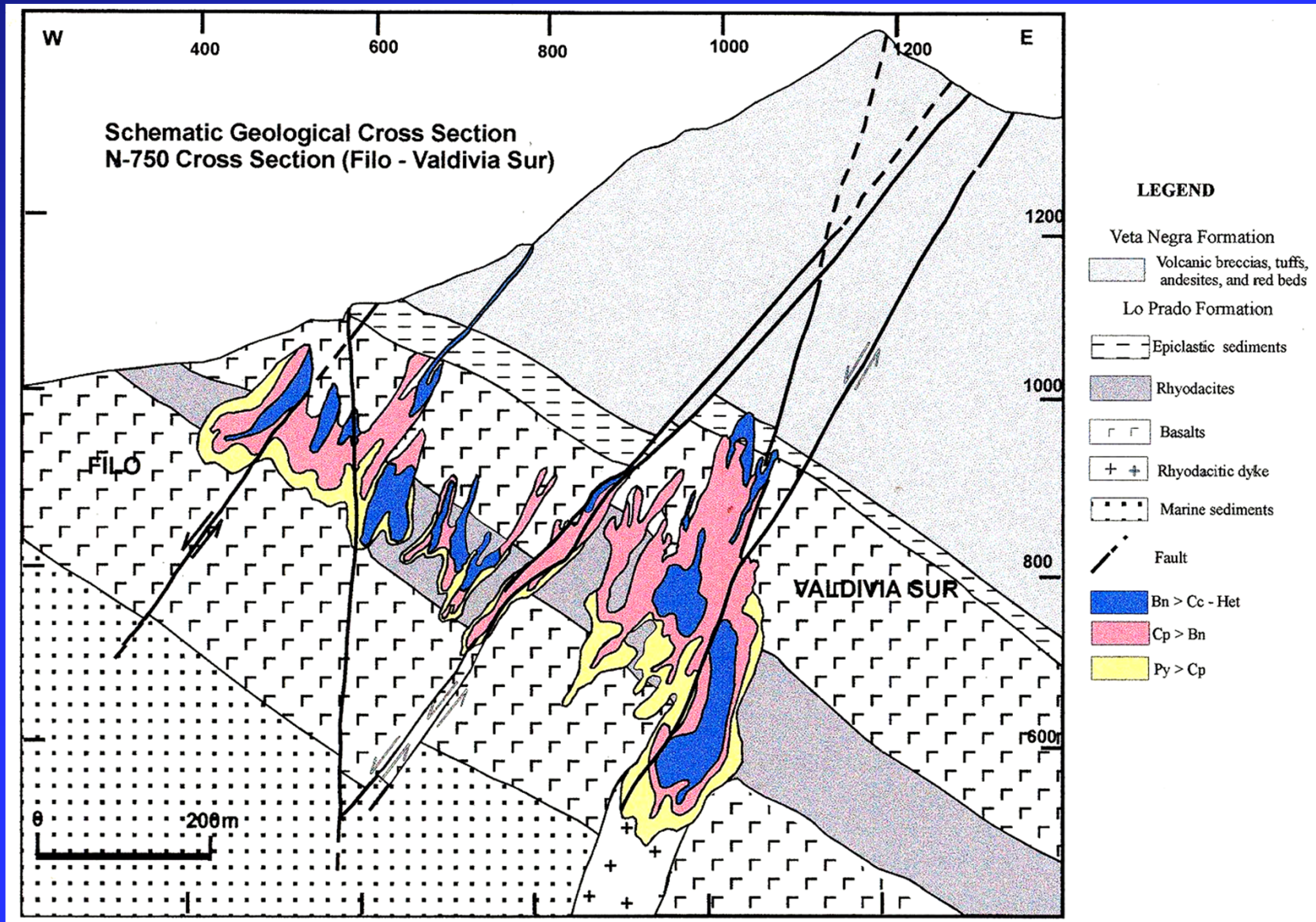
# Outline

1. Introduction to El Soldado, Chile
2. The Problem at hand
3. What are framboids?
4. Petrographic results
5. Microprobe results
6. Sulfur isotope results
7. Framboid control on metallogenesis?
8. Conclusions

# Where is El Soldado?



# El Soldado Cross section



# The Problem

1. Previous studies indicate mineralization occurred in two distinct phases, (I) **Low T**, diagenetic (pyrite), (II) **High T**, hydrothermal (Cu)
2. Mine owners EXXON CMD are skeptical
3. Samples of massive pyrite, deep zones collected
4. Petrography - reflected light
5. S-isotopes
6. Microprobe: chemical and textural



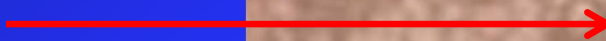
# What are framboids?



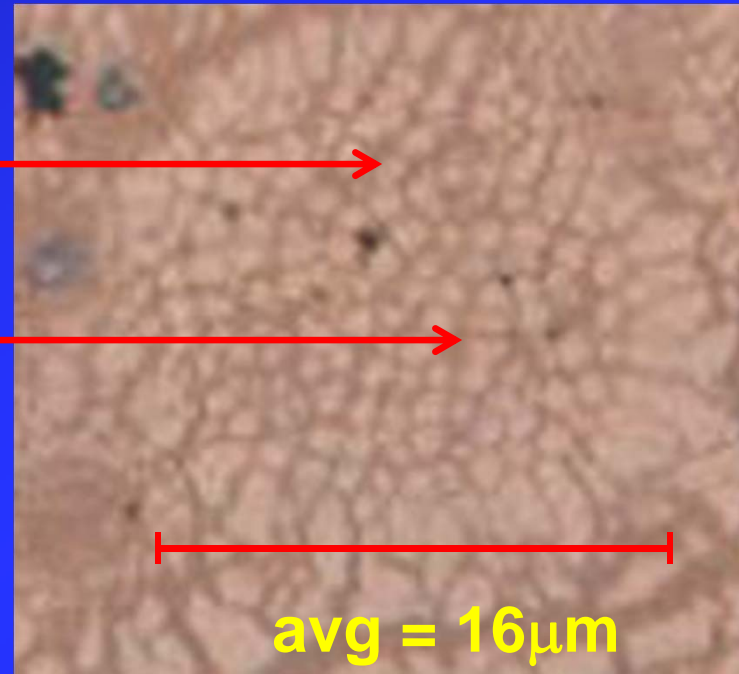
Scanning electron microscope (SEM) image of pyrite framboids  
(Wilson, 1998)

# How do framboids form?

microcrystallite



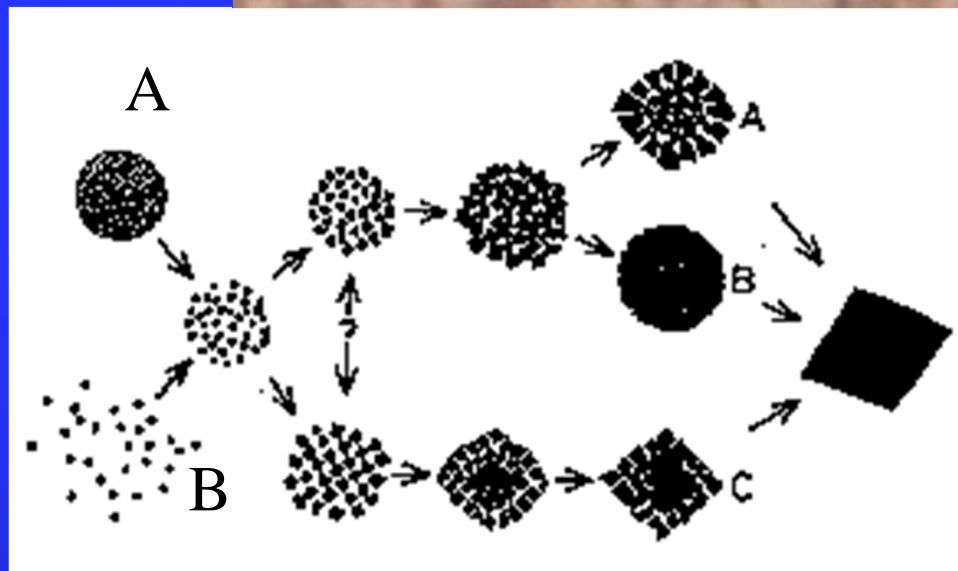
interstitial replacement  
product



avg = 16 $\mu$ m

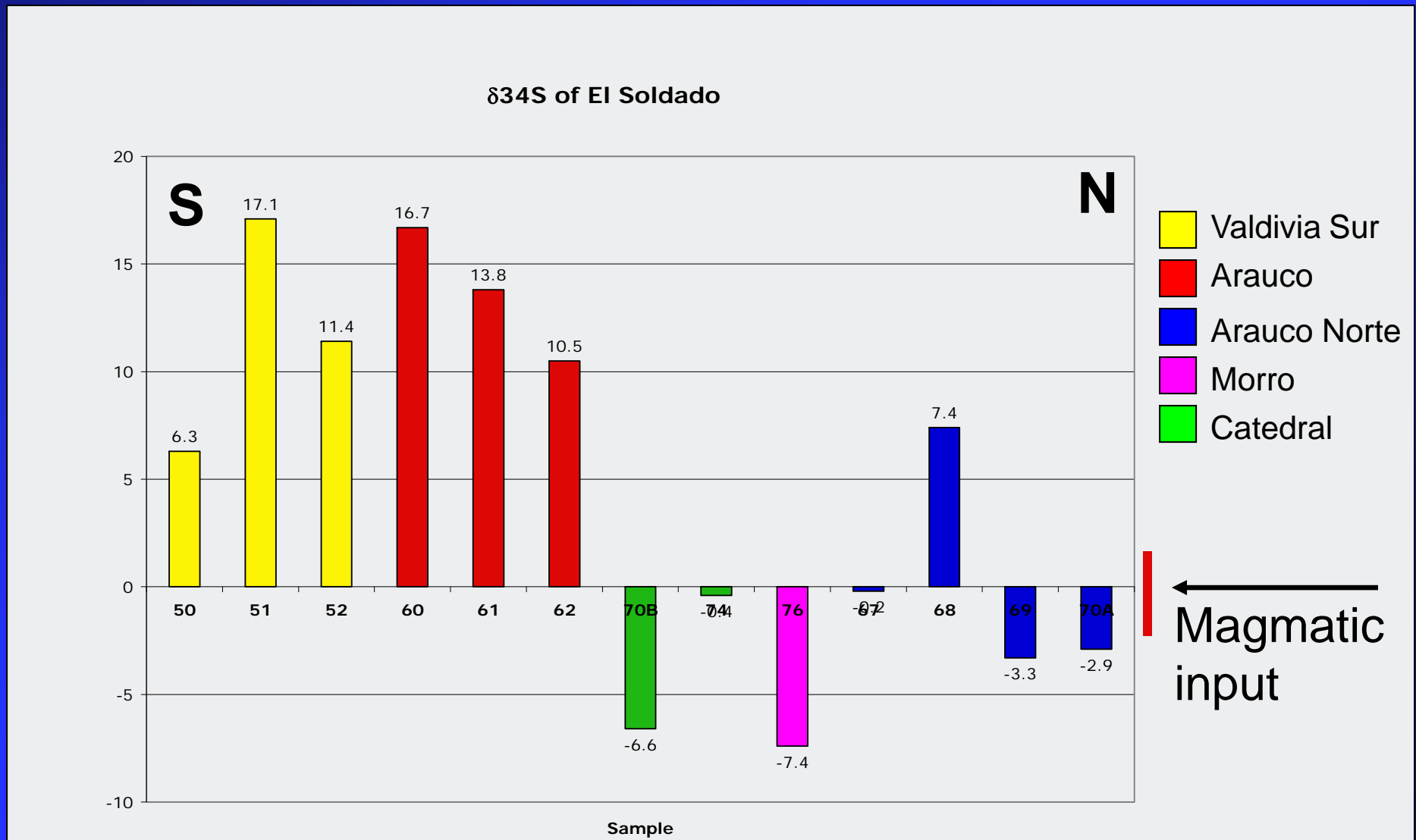
**Potential pathways  
for the formation  
of framboids.**

(After Sawlowicz, 1993)



# $\delta^{34}\text{S}$ isotope values for orebodies at El Soldado

- Thirteen samples sent to Queen's University S-isotope lab



# Petrography

- Paragenetic sequence of sulphides determined
- Textures indicate pyrite framboids have some control on mineralization

Reflected light image of  
framboidal pyrite  
replacement by  
chalcopyrite and bornite



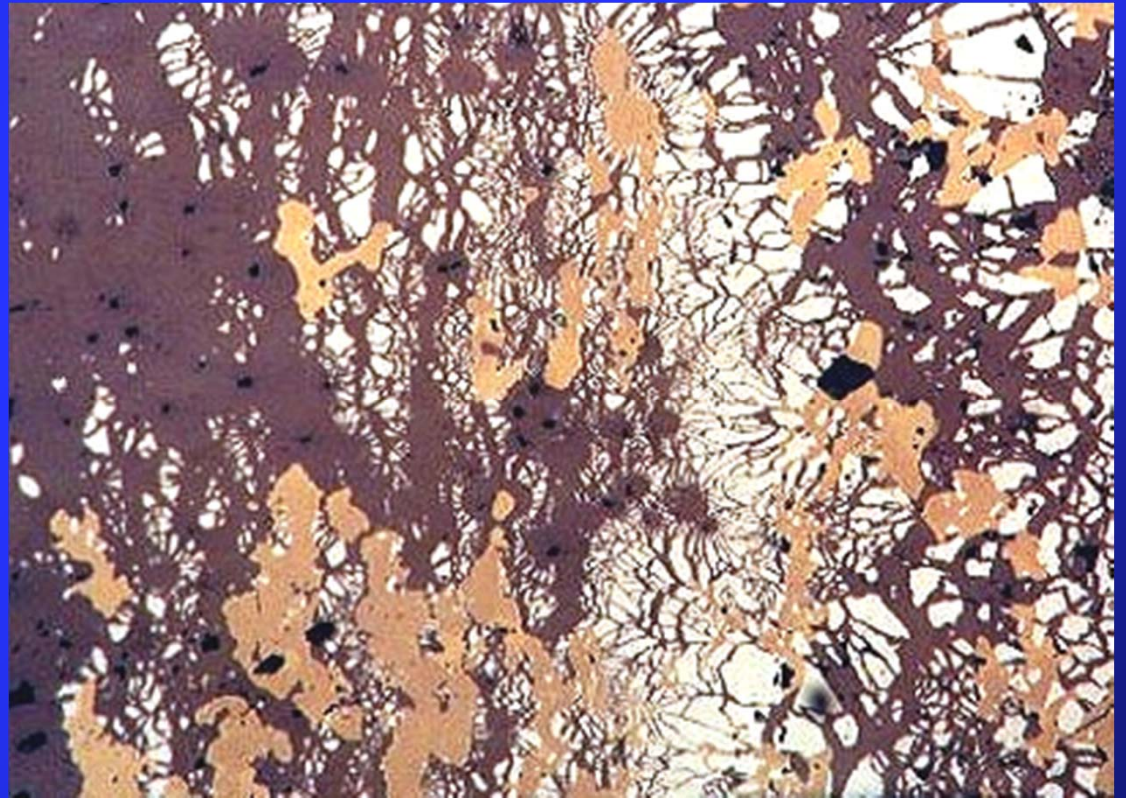
bornite



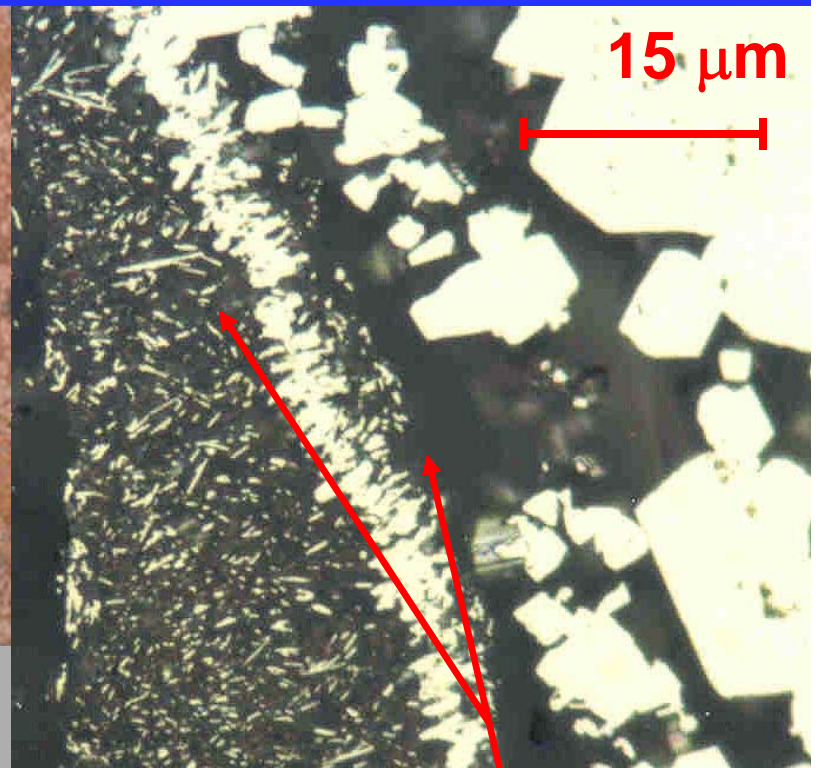
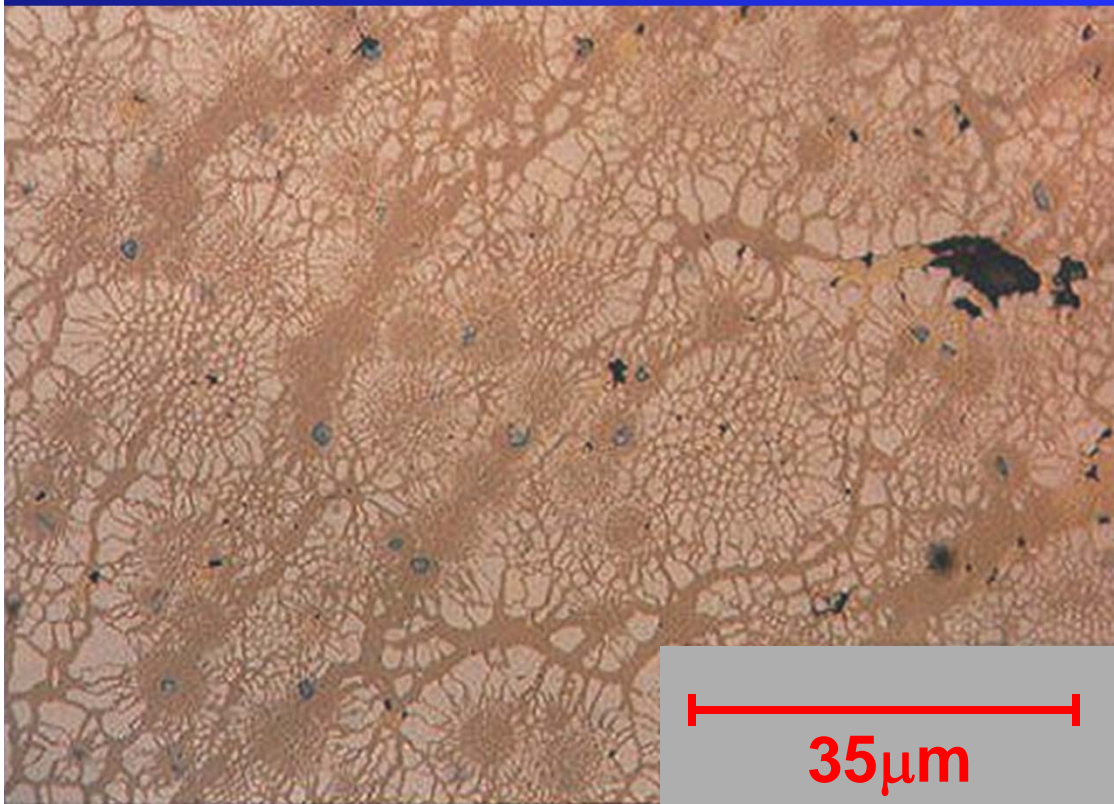
chalcopyrite



pyrite



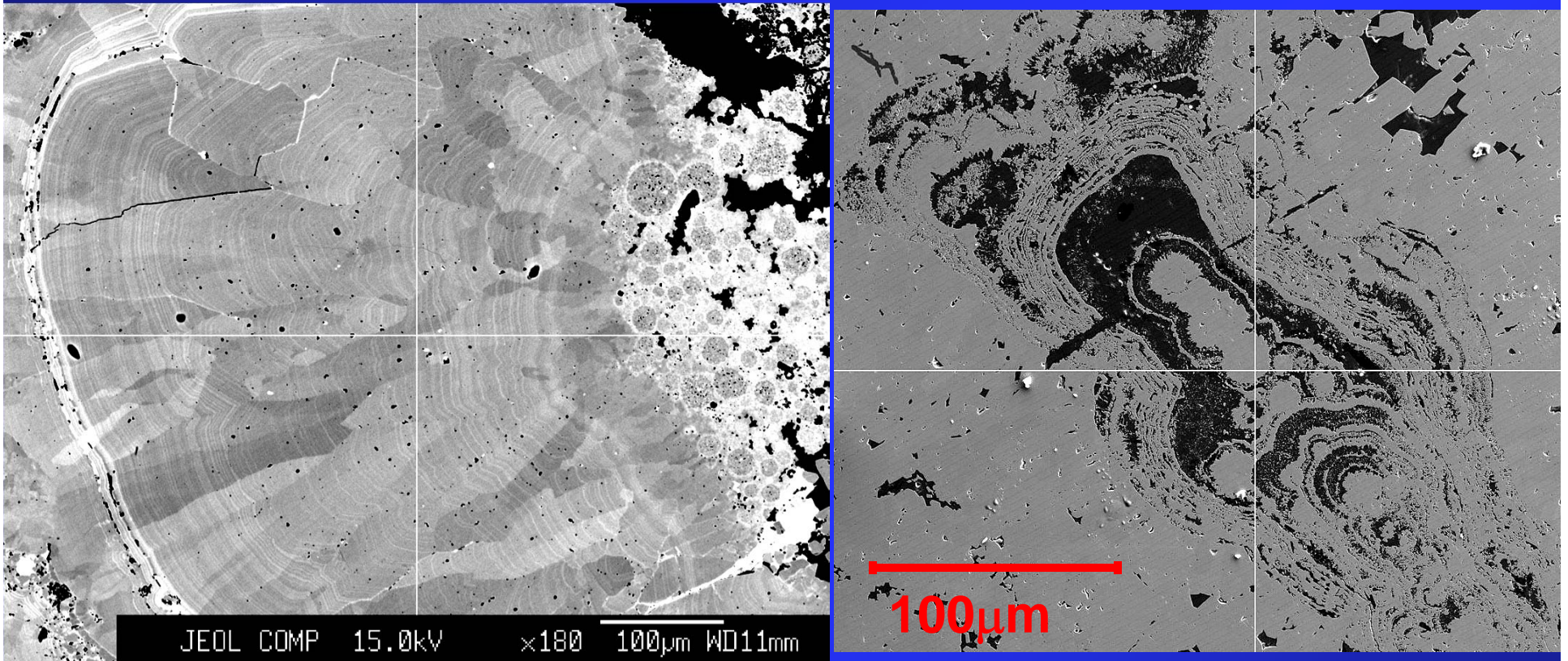
# Evidence for low-T pyrite origin: textures



- Framboids rarely form in hydrothermal deposits; very commonly found in marine sediments, past and present

- Pyrite needles/laths - pyrite does not have this morphology: Pseudomorphing low-T phase?

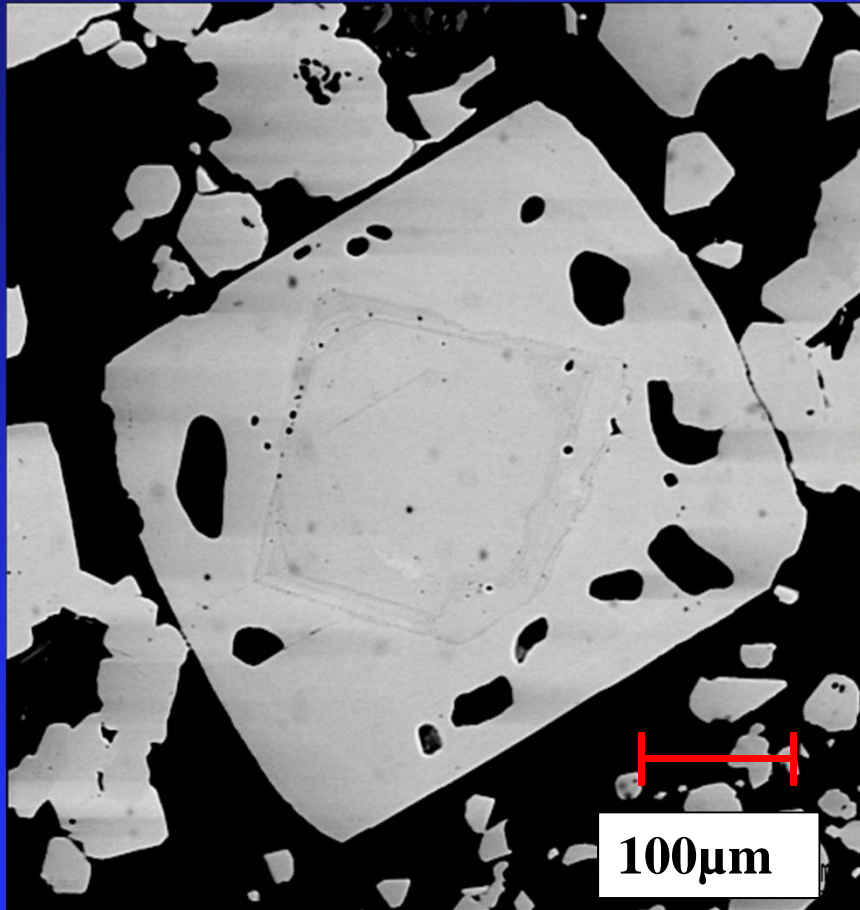
# Slow, low-T growth formed some pyrite



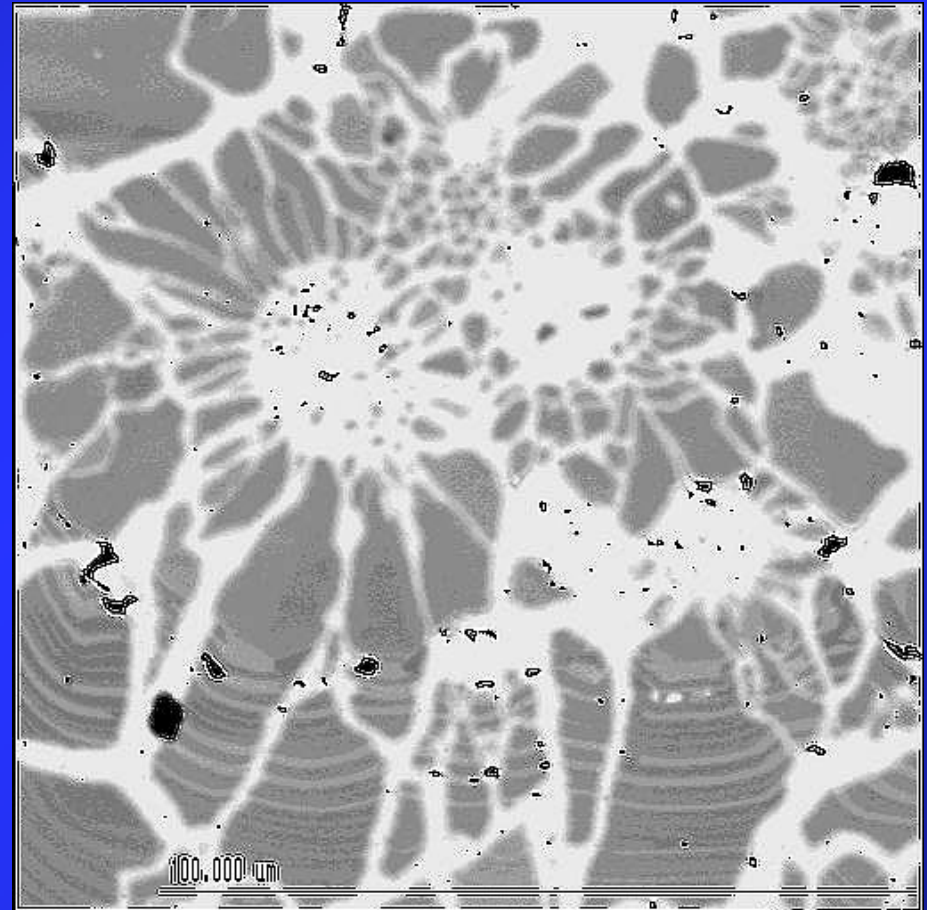
- Growth bands indicate prolonged stability
- Framboids indicate low-T

- Colloform texture characteristic of low-T formation
- Colloform cores are framboidal

# Microprobe Results

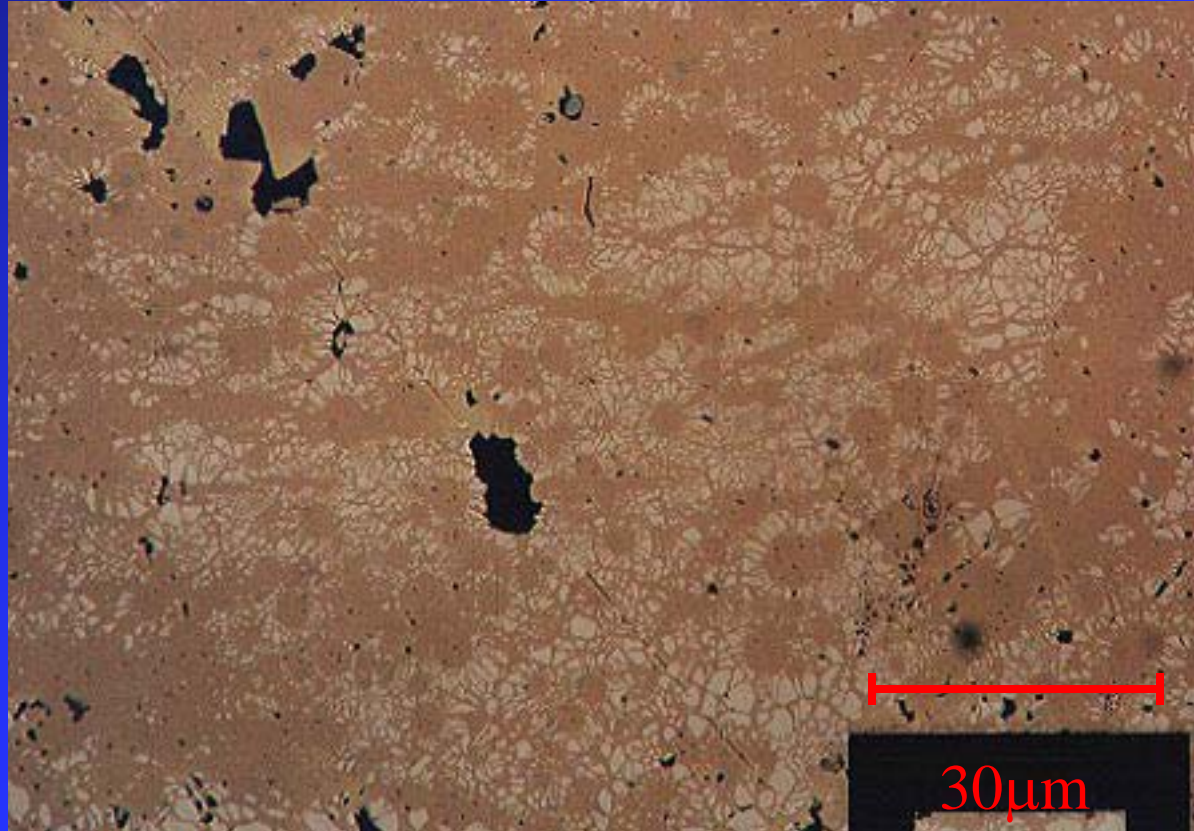


- Compositionally zoned pyrite: rims enriched in Arsenic; distinct primary cube overgrown by late pyrite



- Relative enrichment in As: concentrated in framboids, periphery of framboids and fresh inclusion-free overgrowths

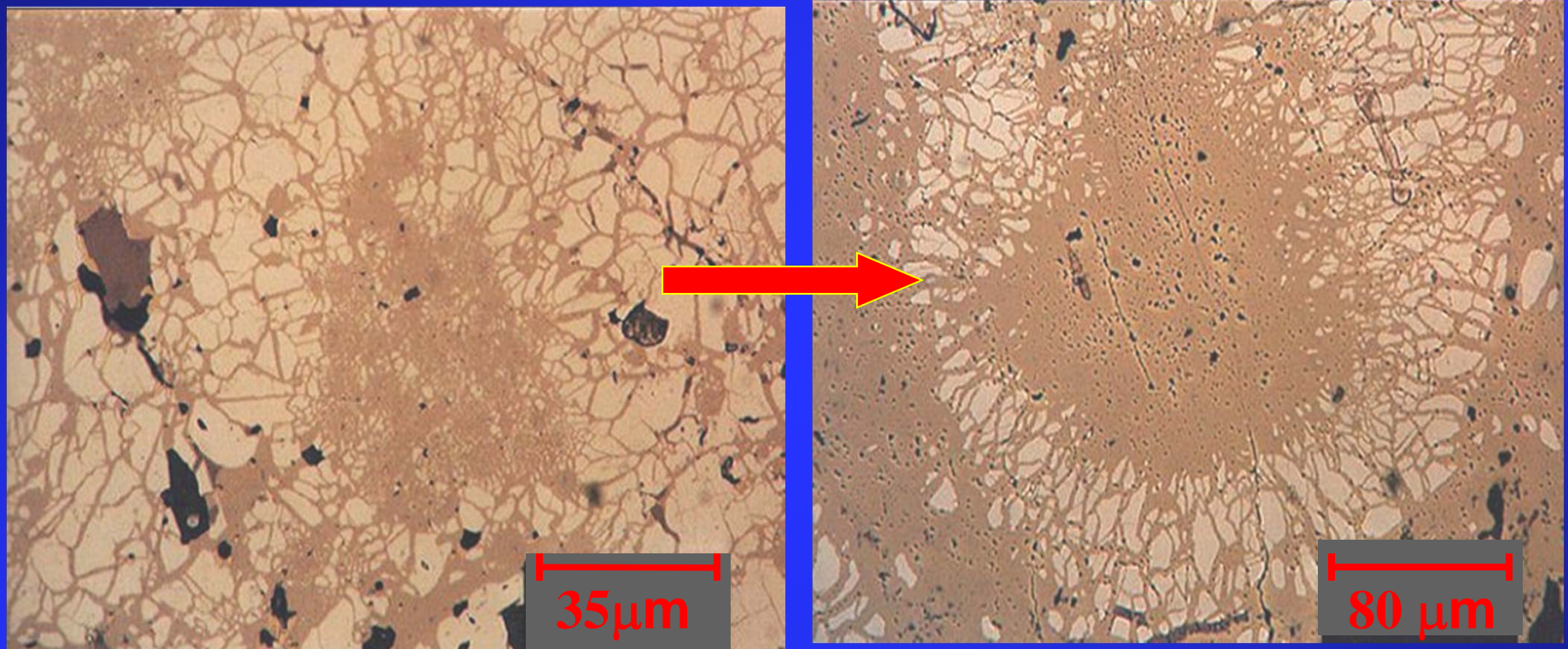
# Framboids control Cu replacement



- Consider system in terms of equilibrium
- Framboids appear to be metastable, likely due to unstable monosulphide origin
- Enormous surface area prone to pseudomorphing



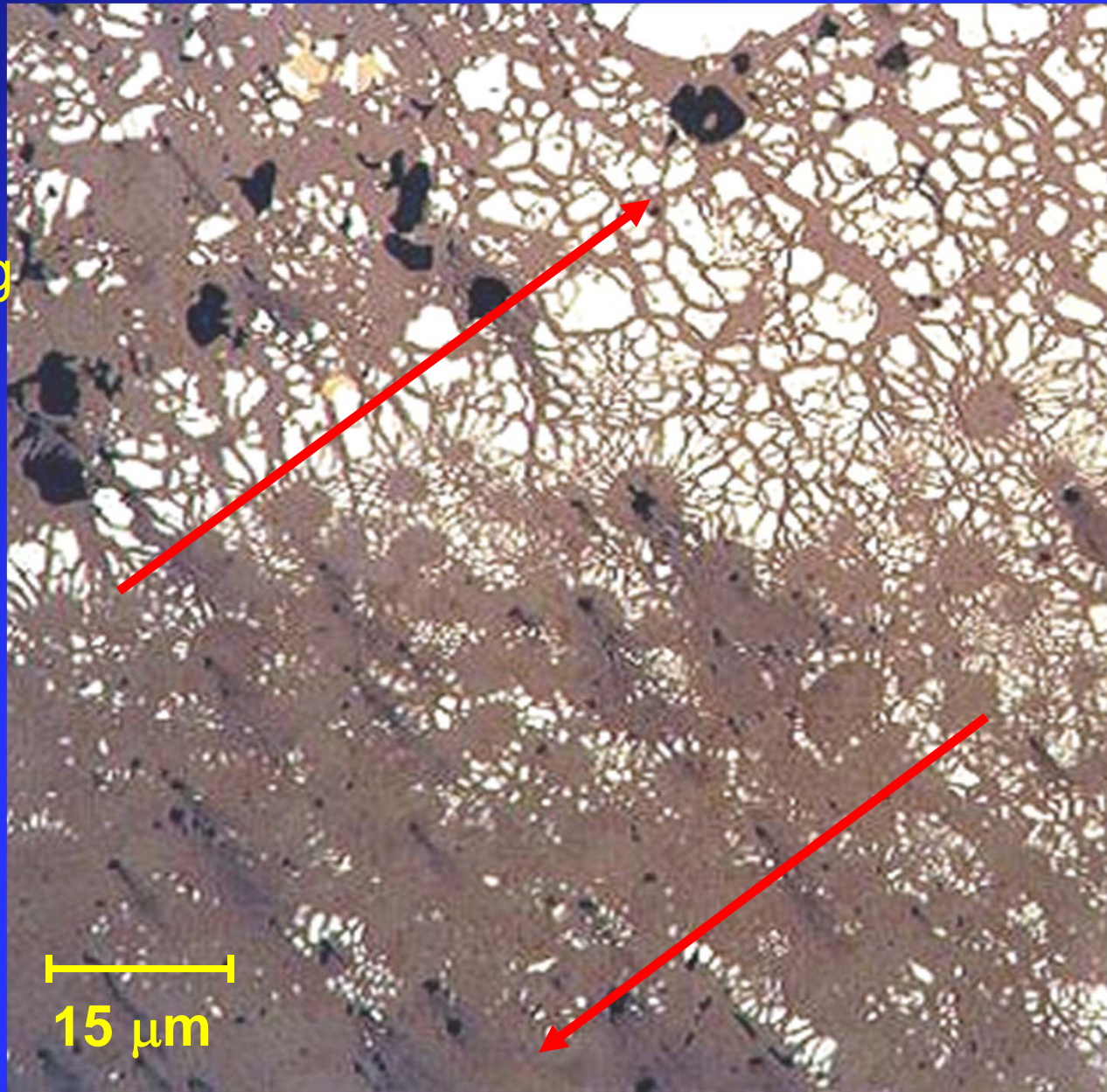
# Continuing replacement: atoll structures



- Unstable framboids replaced before massive, recrystallized pyrite, creating atoll structures, which are typical of preferential replacement

# Nearing the end: high-grade bornite ore

Decreasing  
framboid  
density



15  $\mu\text{m}$

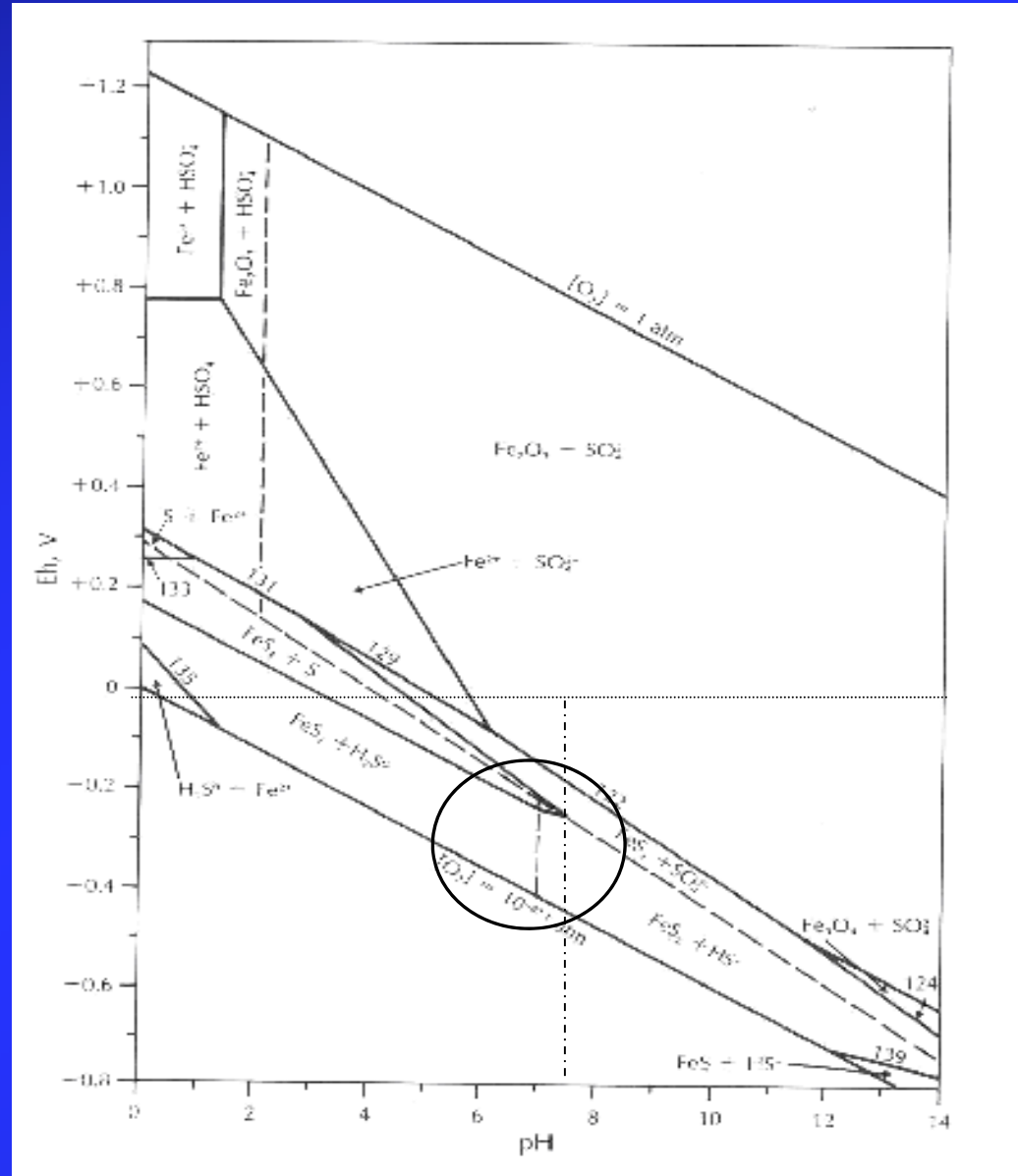
Increasing  
copper  
grade

# Conclusions

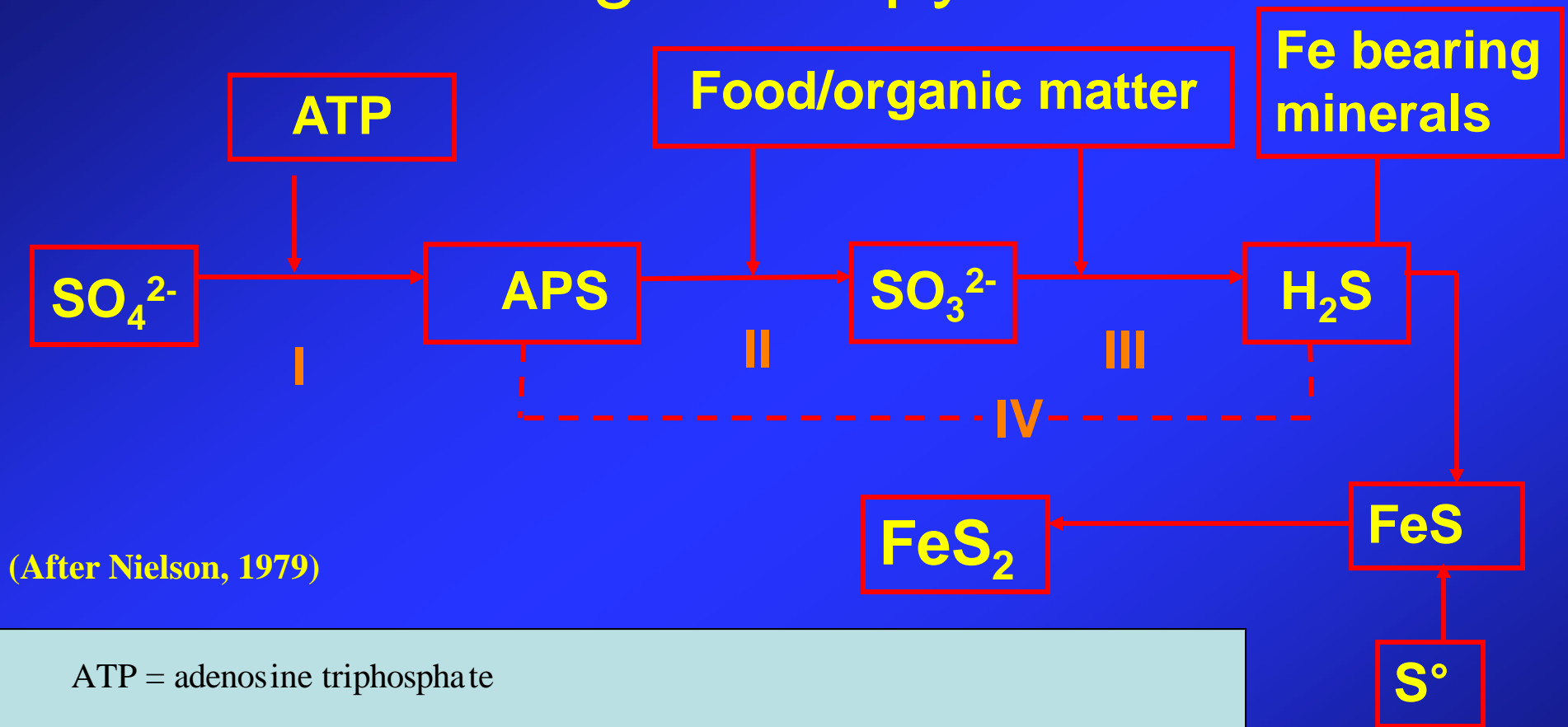
1. Analysis indicate that most pyrite is low-T origin, even deep zones, only minor amounts of hydrothermal pyrite formed (late), and replaced low-T pyrite
2. Copper mineralization is late, *replacing* pyrite (framboids), preserving S, forming hematite with remaining Fe
3. S-isotopes indicate closed system fractionation
4. Multiple phases of growth: remobilized As
5. Mineralization is partially controlled by the instability of framboids, thus mapping their extent aids in exploration models

**Questions?**

# Eh-pH constraints



# Reaction path for (bacteria mediated) diagenetic pyrite



(After Nielson, 1979)

ATP = adenosine triphosphate

APS = adenosine-5'-phospho sulphate

Step I is the rate controlling reaction when sulphate or food is in small

Step II, the breaking of the S-O bond is the normal rate controlling step because it is the most energy intensive step, thus the slowest.